U. S. DEPARTMENT OF COMMERCE
Charles Sawyer, Secretary
NATIONAL BUREAU OF STANDARDS
E. U. Condon, Director

DECEMBER 1948
VOLUME • 41
NUMBER 6

JOURNAL OF RESEARCH

of the

NATIONAL BUREAU OF STANDARDS

Contents

RP		Page
1938.	Effect of boron on the hardenability of high-purity alloys and commercial steels. Thomas G. Digges, Carolyn R. Irish, and Nesbit L. Carwile. (Price 15 cents)	545
1939.	Absorption of radio waves reflected at vertical incidence as a function of the sun's zenith angle. Eloise W. Taylor. (Price 10 cents)	575
1940.	Destruction of superconductivity by current. Russell B. Scott. (Price 10 cents)	581
1941.	Study of the modifications of manganese dioxide. Howard F. McMurdie and Esther Golovato. (Price 10 cents)	589
1942.	Laboratory evaluation of a method proposed by Gnam for measuring the temperature of rotating parts. Andrew I. Dahl and Paul D. Freeze. (Price 10 cents)	601
1943.	Amides of glucuronic, galacturonic, and mannuronic acids. Harriet L. Frush and Horace S. Isbell. (Price 10 cents)	609
1944.	Absorption spectra of methane in the near infrared. Richard C. Nelson, Earle K. Plyler, and William S. Benedict. (Price 10 cents)	615
1945.	Transmittance of near infrared energy by binary glasses. Jack M. Florence, Francis W. Glaze, Clarence H. Hahner, and Ralph Stair. (Price 10 cents)	623
	Index to volume 41 (July to December 1948, Research Papers RP1896 to RP1945).	627

For sale by the Superintendent of Documents, U. S. Government Printing Office, Washington 25, D. C. - Price 50 cents
$4.50 per year on subscription

UNITED STATES GOVERNMENT PRINTING OFFICE, WASHINGTON : 1949

S. Department of Commerce
ational Bureau of Standards

Research Paper RP1938
Volume 41, December 1948

Part of the Journal of Research of the National Bureau of Standards

ffect of Boron on the Hardenability of High-Purity Alloys and Commercial Steels

By Thomas G. Digges, Carolyn R. Irish, and Nesbit L. Carwile

A study was made of the action of boron in relation to the hardenability of high-purity alloys varying in carbon content. The effectiveness of boron in enhancing the hardenability of these alloys and certain steels is believed to be due to its action in retarding the rate of nucleation of ferrite and carbide while in solid solution in austenite. The hardenability of the boron-treated alloys, as determined in terms of the critical cooling rate of small specimens austenitized at a wide range of temperatures, varied with the prior history and with the carbon content. The hardenability of a commercial boron-treated steel, as determined by the end-quench test, was also sensitive to prior thermal treatments. Boron was lost in the decarburized zone of commercial steels, and its rate of diffusion apparently is of the same order of magnitude as that of carbon. The heat treatment of specimens of the alloys and steels to produce a boron constituent and the microstructures of the alloys as cast and as homogenized are described.

I. Introduction

In a previous investigation [1],[1] evidence was tained that the effectiveness of boron in en-ncing the hardenability of certain steels de-nded upon the form of the boron at the time of nching and not necessarily on the total ount of boron present. This observation was sed on a determination of hardenability by the d-quench test. As the study was carried out ring a period of national emergency, but little ttention could be given to the mechanism of the fect of boron on hardenability. The present vestigation was made as a further study of the rdenability of boron-treated alloys and steels th particular attention directed to the action of ron on the hardenability of these materials.

High-purity alloys consisting of: (1) iron and ron, (2) iron and carbon, without and with ron, and (3) iron, carbon, and manganese, thout and with boron were prepared in the boratory, and commercial open-hearth steels re procured for use in this investigation. De-rmination was made of the hardenability in rms of the critical cooling rate of the iron-carbon and iron-carbon-manganese alloys when quenched from various temperatures. The end-quench test also was used for evaluating the hardenability of the iron-carbon-manganese alloys and the commercial steels. A metallographic study was made of specimens prepared from the alloys in the conditions as cast, as forged and homogenized, and as heat treated in various ways to precipitate a boron constituent. Experiments also were made to determine whether boron was lost during the decarburization of commercial steels and for determining the rate of diffusion of boron in austenite of these steels.

[1] Figures in brackets indicate the literature references at the end of this paper.

II. Previous Investigations

Considerable work has been carried out by different investigators in studying the iron-boron equilibrium system. The published diagrams [2, 3], however, were of little value in the present study because of inconsistencies, especially in the solubility of boron in the alpha and gamma fields, and deficiency in information on alloys containing the relatively low amount of boron now used commercially in boron-treated steels (0.0005 to 0.005 percent of boron).

The action of boron in increasing the harden-

ability of steel is not definitely known, but tentative explanations have been reported in the literature. These theories may be classified on the basis that the improvement is due to boron in solid solution in austenite, and a reaction of boron with some other element to change the condition of the latter.

Grange and Garvey [4] assumed the presence of boron in steel in both an effective and an ineffective form. The effective form is capable of dissolving in austenite, whereas the ineffective boron does not enter into austenite solid solution. The small boron atom is pictured as forming an interstitial solid solution with gamma iron. The boron atoms are preferentially located in the grain boundaries of the austenite just prior to its transformation, and their presence lowers the rate of grain boundary nucleation and thus increases hardenability. As boron has a relatively low solubility in austenite, some of the boron atoms may be precipitated as some compound and thus form a "film" at the austenite grain boundaries that is supersaturated with respect to these atoms. This precipitate seemingly occurs rapidly and in advance of the usual transformation of austenite to ferrite; only those boron atoms that remain in solid solution are effective in decreasing the rate of nucleation of ferrite and hence in increasing the time required for austenite to transform. Heating steel at a high temperature for a long time may convert effective into ineffective boron; the latter may be some stable chemical compound of boron that gradually forms at high temperature. Lippert [5] stated that boron, similar to any other alloying element, must be in solid solution to be effective in increasing hardenability.

Chandler and Bredig [6] were of the opinion that nitrides act as nucleating agents in the decomposition of austenite, particularly for the rejection of ferrite. The hardenability effect of boron, either alone or in combination with other elements, appears to be the influence of a fluxing agent upon the particle size of nitrides of other elements, such as those of silicon, aluminum, titanium, and zirconium. Thus boron converts particles of harmful critical size into particles of larger size unable to effect nucleation. Corson [7] assumed that boron increases hardenability by its action in removing something in the steel (possibly free nitrogen) that exists in very small amounts by weight and which has a deleterious effect on hardenability. Bain [8] apparently was of the opinion that boron has little effect as an alloying element but more likely acts as a sort of cleansing agent, perhaps in some connection with the nitrogen content of the steel. Dean and Silkes [9] were inclined to believe that the effect of boron on hardenability was due to a dispersion rather than a solution in austenite. Presumably the boron in excess of the small amount required for maximum hardenability reacts with some other constituent in the steel.

Digges and Reinhart [1] found no definite correlation between the amount of boron added or retained in experimental (induction melted) and commercial open-hearth steels and the hardenability as determined by the end-quench test. In many of the aluminum-killed experimental steels, the optimum hardenability was obtained with small additions of boron (0.001 % or less retained), whereas in other steels the hardenability increased continuously with increase in boron (about 0.0015 to 0.006 %). In still other steels, the addition of boron as a simple or complex intensifier was either without effect or impaired the hardenability. The hardenability of boron-treated steels varied also with the state of deoxidation and with the nitrogen content. High acid-soluble nitrogen (sulfuric acid) was usually detrimental to the effect of boron on hardenability, but it was possible to retain the effect in high-nitrogen steels (low-soluble nitrogen) by fixing the nitrogen with strong nitride-forming elements such as titanium. With the commercial boron-treated steels, the magnitude of the hardenability effect was independent of the amount of boron added or retained and the chemical composition of the intensifiers used.

Boss [10] speculated that boron increases hardenability of steel by the removal of the last trace of oxygen, but boron itself is harmful to hardenability; a small amount of oxygen is also detrimental to hardenability. Grossmann [11] suggested the possibility of the boron being present, at least in part, as stable carbides.

III. Alloys and Steels Used

The chemical compositions of the high-purity alloys and the steels used are given in table 1.

In preparing the alloys, one lot of electrolytic iron was used as the base material. Melting was

TABLE 1. *Chemical composition of the alloys and steels used*

Identification	Percentage by weight as determined—																
	Chemically						Spectrographically [1]								By vacuum fusion		
	C	Mn	P	S	Si	B	Mn	Si	Ni	Co	Cu	Al	Cr	B	O	N	H
IRON-BORON ALLOYS																	
B3	<0.01	---	---	---	---	0.0028	0.002	<0.01	0.013	0.008	0.003	0.003	<0.001	---	0.011	0.001	0.0001
B4	<.01	---	---	---	---	.011	.002	<.01	.012	.008	.004	<.001	<.001	---	.008	---	.0003
IRON-CARBON ALLOYS																	
B8	0.32	---	---	---	---	[2] None	0.002	<0.01	0.013	0.008	0.002	0.001	<0.001	[3] ND	0.003	0.001	0.0003
B6	.32	---	<0.001	0.002	---	0.0021	.002	<.01	.011	.008	.001	.001	<.001	---	.003	.001	.0003
B7	.50	---	---	---	---	None	.001	.002	.010	.007	.001	[3] ND	ND	ND	.002	.001	.0002
B12	.54	---	---	---	---	None	.002	<.01	.010	.007	.002	<.001	<.001	ND	.001	.001	.0001
B2	.47	---	---	---	---	.0020	.001	.002	.013	.008	.001	ND	ND	---	.004	.001	.0003
B10	.70	---	---	---	---	None	.002	.025	.009	.007	.003	.008	<.001	0.0004	.001	.0005	.0004
B5	.74	---	---	---	---	.0028	.002	<.01	.011	.007	.001	<.001	<.001	---	.005	.001	.0004
IRON-CARBON-MANGANESE ALLOYS																	
B13	0.42	0.67	<0.001	0.002	0.087	None	---	0.11	0.012	0.008	0.001	0.041	<0.001	ND	0.002	0.001	0.0001
B14	.41	.64	<.001	.002	.096	0.0024	0.68	.09	.010	.008	.001	.003	ND	0.0025	.001	.001	.0001
COMMERCIAL STEELS [4]																	
C15	.043	1.58	0.020	0.019	0.31	[5] None	---	---	---	---	---	---	---	---	---	---	---
C9	.43	1.58	.019	.019	.32	0.0003	---	---	---	---	---	---	---	0.0004	---	---	---
C11	.42	1.59	.019	.018	.32	.0011	---	---	---	---	---	---	---	.0014	---	---	---
C12	.43	1.56	.020	.019	.31	.0022	---	---	---	---	---	---	---	.0020	---	---	---
C14	.43	1.59	.018	.019	.32	.0036	---	---	---	---	---	---	---	.0040	---	---	---
C19	.43	1.58	.019	.018	.31	.0001	---	---	---	---	---	---	---	.0003	---	---	---

[1] V, Mo, Sn, and W were searched for in all of the alloys and Ti and Zr in most of the alloys. These elements were not detected, but a small amount of Be was found in B13.

[2] None denotes not added.

[3] ND denotes not detected.

[4] Split open hearth heat. The boron additions were made with Grainal No. 79 (C9 and C11), Ferroboron (C12 and C14), and Grainal No. 1 (C19) in the ladle.

[5] Trace (less than 0.0001 %) boron was detected by chemical analysis.

by induction heating of the charge in crucibles of high-purity magnesia, except for the two alloys containing manganese (B13 and B14), which were melted in commercial crucibles of beryllia. Additions as required were made of carbon and electrolytic manganese in the initial charge, whereas the boron was added to the molten metal as commercial ferroboron containing about 12 percent of boron. The heats were not deoxidized with aluminum or silicon. Melting and subsequent solidification of the ingot were carried out in vacuo obtained by means of a mechanical vacuum pump rated to attain a vacuum of 0.02 μ of mercury. In most cases, the system was vacuum tight as was indicated by the manometer after standing for 12 to 15 hr. without operating the pump. The boron additions were made by means of a special holder without disturbing the vacuum.

The manganese, nickel, and cobalt contents were approximately the same for each alloy, except for two (B13 and B14) in which the manganese was intentionally added. These impurities and the sulfur and phosphorus contents, as determined for several of the alloys, were about the same as those contained in the electrolytic iron used as the base material. In some cases, there was some pick-up in silicon and aluminum (incident to the melting operation) especially in the alloys prepared in the commercial crucibles. The results of the vacuum fusion analyses showed that the oxygen and nitro-

gen contents of the alloys were low except for the relatively high values for oxygen of the two iron-boron alloys (B3 and B4) not treated with carbon; 0.004 to 0.005 percent of oxygen was obtained in the boron-treated alloys B2 and B5.

Some of the ingots of the high-purity alloys were hot forged to a range of about three-quarters to one-third of their original diameters. The outer surfaces of these forged bars were removed by machining prior to carrying out a homogenizing treatment by heating in vacuum at temperatures ranging from 1,700° to 1,900° F for varying periods. The evacuated tube containing the bars was cooled from the high temperature in air. Microscopic examination of the cross section of the bars after the homogenizing treatment indicated a fair degree of uniformity in distribution of the carbon. Specimens subsequently used for test purposes were prepared from the original ingots (as cast) or from the bars as homogenized.

The commercial steels were from the same "split" open-hearth heat as that used and described in a previous investigation [1]. The boron additions were made in the mold with Grainal No. 79, (Steel C9 and C11), Ferroboron (Steels C12 and C14), and Grainal No. 1 (Steel C1 These steels were received in the form of h rolled 1¼-in. rounds.

IV. Austenite Grain Size

Since the hardenability of most steels is infl enced by the size of the grains at the time quenching, a determination was made of t grain size established at the quenching temper tures of each alloy and steel used in carrying o the critical cooling rate and end-quench tes Grain size measurements were made by t method described by Jeffries [12] or by estimati the grain number by comparing the microsco image at 100 diameters with an American Soci for Testing Materials standard grain size chart.

The results obtained on the small specime used for determining the critical cooling rate a summarized in table 2 and illustrated by typi photomicrographs in figures 1 and 2. In some the quenched specimens, the parent austeni grains could be revealed by a contrast etch of t martensite (fig. 1), or by the presence of sm amounts of fine pearlite located at their boundar (fig. 2, A).

TABLE 2. *Austenite grain size of the alloys*

Small specimens, initially as homogenized or as cast, were heated rapidly to the required temperature, held at this temperature for 15 min, before cooli various rates. The same specimens were used to determine critical cooling rates.

Identification	Percentage			Average number of grains per square inch at times 100 diameters, at—						
	C	B	Al	1,425° F	1,500° F	1,600° F	1,700° F	1,800° F	1,900° F	2,000° F
INITIALLY AS HOMOGENIZED										
B8	0.32	None	0.001	.....	14	6	7	6	5	3
B6	.32	0.0021	.001	.....	.....	7	7	6	5	3
B7	.50	None	ND [1]	16	9	8	13	11	14	14
B12	.54	None	<0.001	7	6	5	7	6	5	4
B2	.47	0.0020	ND	.....	8	7	6	3	3	2
B10	.70	None	0.008	.....	[2] 24 to 48	[2] 12 to 24	[2] 6 to 12	6	5	3
B5	.74	0.0028	.001	17	13	12	14	13	14	16
B13 [3]	.42	None	.04	.....	8	8	6	6	6	7
B14 [3]	.41	0.0024	.003	.....	9	8	3	2	1	1
INITIALLY AS CAST										
B6	0.32	0.0021	0.001	.....	.....	[2] 24 to 48	11	11	13	15
B2	.47	.0020	ND	.....	10	9	4	4	3	2
B5	.74	.0028	<.001	[2] 24 to 48	[2] 24 to 48	[2] 24 to 48	[2] 12 to 24	[2] 12 to 24	[2] 6 to 12	[2] 6 to 12

[1] ND denotes not detected.
[2] Estimated.
[3] The alloy also contained approximately 0.65 percent of manganese and 0.10 percent of silicon.

Although an attempt was made to heat the specimens relatively rapidly through the transformation temperature range, the heating rates varied to some degree with the different specimens and with the maximum temperature attained. As previously shown [13], the grain size at temperatures somewhat above Ac_3 of high-purity iron-carbon alloys varied with the rate of heating through the transformation temperature range; the austenite grain size increased markedly with a decrease in rate of heating. Variations were sometimes obtained in the grain size of the different specimens of a selected alloy, especially B2 and B10, when heated to the same temperature, as is illustrated for alloy B12 in figure 1, C and F, and occasionally a wide variation in the size of the grains was obtained in the same specimen (fig. 1, D and E). Grain-size measurements made on the latter specimen are practically meaningless. In some cases, the variation in grain size at a selected temperature of different specimens of the same alloy was as great or greater than that due to the range in temperature used. (Compare fig. 1, C and F with fig. 2, D and F.) Because of these conditions, the same specimens were used for determining the austenite grain size and the hardenability. That the austenite grain size of one of the alloys (B13) is affected by the rate of heating or by prior thermal treatment is shown by the photomicrographs of figure 2. The grain size at 1,500°, 1,700°, and 1,900° F of an end-quench specimen is shown in figure 2, A, B, and C and that of considerably smaller specimens (used in determining the critical cooling rate) in figure 2, D, E, and F. The grain size of the end-quench specimen increased with a change in temperature from 1,500° to 1,700° F, but there was practically no further increase in size when heated to 1,900° F. The average grain size of the small specimens was unaffected by this range in austenitizing temperatures. The same specimen was used for end-quenching from each temperature, and the small specimens were prepared from this bar after the quench from 1,900° F. The bar was normalized at 1,650° F prior to each quenching treatment. The specimen for end-quenching was heated in a furnace at the desired temperature for 45 min (total time in furnace), and it required an estimated time of 10 to 15 min to attain the temperature of the furnace. The small specimens were heated from room temperature to the austenitizing temperature in approximately 2 min and were held at temperature for 15 min (in furnace for 17 min) before quenching; it required about 6 to 8 sec to heat each specimen through the transformation temperature range. All specimens had an initial structure of fine pearlite and ferrite, but variations thus existed in the rate of heating and time at the austenitizing temperature of the two series. It is noteworthy that the grain size established at 1,500° F was somewhat finer in the large than in the small specimen (fig. 2, A and D), although the rate of heating was slower and the time at temperature was greater for the large than for the small specimens; the grain size should increase, not decrease, with time at austenitizing temperature. The trend for the grain size at 1,500° F of this iron-carbon-manganese alloy containing 0.04-percent aluminum (B14) to increase with the faster rate of heating is the reverse of that observed previously in high-purity iron-carbon alloys. It was shown [13], however, that the austenite grain size at the temperature ordinarily used in hardening an aluminum killed commercial steel containing 0.5-percent carbon increased with increase in rate of heating through the transformation temperature range.

Intermediate or coarse grains were established at each austenitizing temperature of each alloy (table 2 and fig. 18). This is to be expected, as the alloys were of relatively high purity with the presence of only small amounts, if any, of the grain-refining elements (other than carbon) except for the 0.04-percent aluminum in B13.

The austenite grain size of some of the alloys varied with the initial condition of the specimens (table 2). At a selected temperature, the size of the grains in an initially homogenized specimen was either approximately the same or coarser than that of the same alloy initially as cast.

With an initial structure as homogenized, the average size of the austenite grains of alloys B7, B12, B13 (all without boron) B6 and B5 (each with boron) was not significantly affected by the range in austenitizing temperatures used. However, there was some increase in grain size of alloys B8 and B10 (without boron), and B2 and B14 (with boron) with a change from the lower to the higher part of the range in austenitizing temperatures.

With an initial structure as cast, the average size of the austenite grains of alloys B6, B2, and B5

(all with boron) was somewhat finer at the lower than at the higher austenitizing temperatures.

Apparently, boron had no consistent effect on the austenite grain size and coarsening temperature of these high-purity alloys.

V. Hardenability

1. Procedure

Numerous methods have been proposed and used for determining the hardenability of steel. The selection of a method depends largely upon the nature of the information desired and range in hardenability of the steels or alloys. The standard end-quench test is widely used commercially for measuring the hardenability of low alloy steels (intermediate hardenability), but it is not well suited for the shallow hardening type (plain carbon) or for the deep hardening alloy steels, such as those that harden through in ¾-in. rounds or larger sections by cooling in air.

In carrying out a fundamental study of hardenability, it is a common practice to measure either the cooling rate at a selected temperature or the cooling time or rate through a temperature interval during the quenching operation, and then evaluate the cooling time or rate in terms of the structure or hardness of the quenched specimen. However, different parameters, including temperature intervals, structures, and hardnesses have been used by various investigators. French [14] used the cooling rate at 1,330° F, Boeghold and Weinman [15] at 1,300° F. and the time to cool from 1,350° to 900° F., and Post, Fetzer, and Fenstermacher [16] used the rate at 1,000° F. to evaluate hardenability; values for the cooling rate at 1,300° F. are included in the chart prepared by the American Society for Testing Materials [17] for presenting data obtained in the end-quench test. Grossmann [18] and coworkers used the time required to cool from the quenching temperature to that half way down to the temperature of the quenching medium, and they arbitrarily selected a structure consisting of 50-percent martensite and 50-percent pearlite (ferrite and carbide) as the division between the hardened and unhardened condition. These data have been used extensively in computing the hardenability from the chemical compositions of the steels.

The isothermal transformation diagrams (S or TTT curves) for numerous steels [19] show that the decomposition of austenite to aggregates of ferrite and carbide (pearlite) is most rapid in the temperature range of about 1,110° to 930° F (nose curve) but in some steels, notably the deep hardening type containing high molybdenum, the nose of the isothermal transformation curve may occur in the lower part or below this range. To completely harden a steel by quenching, it is essential to cool with sufficient rapidity to prevent the austenite from transforming in this temperature range. If by a continuous quench to approximately room temperature, the austenite is cooled through the range of 1,110° to 930° F without decomposing, it remains unchanged until a temperature is reached that is favorable for its transformation to martensite. This applies to most steels in which pearlite rather than bainite limits the formation of martensite. At some cooling rate, called the critical cooling rate, the austenite of a steel that is capable of hardening by quenching just begins to transform at the nose of the S-curve. The critical cooling rate, therefore, is an index to hardenability. The slower the critical cooling rate, the deeper is the hardening of the steel. Published data show that the temperature of the initial transformation of austenite to martensite is not affected by the rate of cooling, that is, the start of the Ar″ or Ms temperature is not depressed by rapid cooling.

A determination of the critical cooling rate was used at this Bureau in a study of the hardenability of high-purity alloys of iron and carbon [20]. With suitable equipment the method is capable of producing results of a high degree of accuracy, and it is applicable for alloys with a wide range in hardenability. This method was, therefore, selected for use in the present study. In addition, the standard end-quench test was used for evaluating the hardenability of the two alloys containing manganese (B13 and B14, table 1) and for determining the effects of quenching temperature and initial structure on hardenability of the commercial steels.

(a) Critical Cooling Rate

The apparatus and procedures used for obtaining time-temperature cooling curves were similar to those described in some detail in a previous report [20]. The essential features consisted of using specimens approximately 1/10 in. square by 0.04 in. thick with one wire of a 32-gage chromel-alumel thermocouple spot welded to the center of

flat face and the other wire welded to the opposite face. The specimen was heated rapidly (usually the specimen attained the austenitizing temperature within 2 min) in an atmosphere of dry nitrogen, or in vacuo, to the required temperature and held at temperature for 15 min. before quenching directly in helium. Cooling of the specimen was recorded photographically by means of an Einthoven string galvonometer apparatus, and a time-temperature cooling curve was plotted from this record. Metallographic examination was made of the cross section of the quenched specimen a short distance from the points of contacts of the thermocouple wires, and the structure of the specimen was correlated with its cooling time or rate. The quenching temperature used ranged from 1,425°, 1,500°, or 1,600° to 2,000° F, depending upon the carbon content of the alloy.

The amount of fine pearlite (nodular troostite) or bainite contained in the quenched specimen was estimated as 0.0 percent, trace, 0.2, 1.0 or over 1.0 percent. The photomicrographs of figure 3, A, B, and C were used as a "standard" in making this estimate. In a continuous quench of these high-purity alloys, the initial transformation product of austenite, which was formed at the nose of the S-curve was fine pearlite as is illustrated in figure 3; some bainite also was formed in some of the specimens of the two alloys (B13 and B14), which contained about 0.7-percent manganese.

(b) End-Quench Test

The procedure as recommended by the American Society for Testing Materials [17] was regularly followed in making the standard end-quench test, except that when higher quenching temperatures than those usually recommended were used, the quenched bar was ground to a depth of 0.030 to 0.045 in. preparatory to making the hardness measurements; with the high-purity alloys (B13 and B14), the same specimen was used for each of the three end-quenching treatments. These specimens were not exactly round at the time of carrying out the last two treatments, as they contained either two or four flats ground on the surface for use in the prior determination of hardness. A special fixture was used for positioning the specimen for making the Rockwell hardness measurements.

2. Results

(a) Iron-Carbon Alloys

Critical Cooling Rate. A photographic record of the time-temperature relationship, which was obtained with each specimen during the quench, permits an evaluation of these data in terms of the cooling time or rate at any selected temperature or temperature interval within the range corresponding to that of the start and finish of the quench (austenitizing and approximately room temperature, respectively).

Specimens Initially as Homogenized. The relation of the time required to cool specimens through three temperature ranges to the structures of the iron-carbon alloys is given in figures 4 to 10. These specimens were prepared from initially homogenized bars and were quenched from various temperatures. In these figures, the curves represent the relation of the cooling time for the formation of 0.2-percent fine pearlite (critical cooling time) to the quenching (austenitizing) temperature. The values for the specimens, which were cooled too rapidly to allow the critical amount of austenite to transform (at the nose of the S-curve), should fall below the curve, whereas the values for the specimens containing more than 0.2-percent pearlite should lie above the curve. There were some inconsistencies in this relation that may have been caused by a variation in grain size at the austenitizing temperature or by chemical inhomogeneity. As is illustrated in figure 5, however, no definite correlation was obtained between cooling time and structure of initially homogenized specimens of the alloy B6 containing 0.32-percent carbon and 0.0021-percent boron when quenched from temperatures ranging from 1,600° to 2,000° F. It is believed that the relative ineffectiveness of boron in improving the hardenability of some of the specimens may be due to a change in the form of boron in the austenite brought about during the hot-working (forging) or homogenizing process. Evidence supporting this view will be discussed later in connection with figure 15.

The relation of critical cooling time to quenching temperature of an alloy was quite similar for each of the three temperature intervals used, as is shown by the shape of the curves. This is to be expected because of the exponential type of cooling curve that was obtained on quenching the

small specimens from the austenitizing temperature in gas at a rate sufficiently fast to prevent less than about 5 percent of the austenite transforming to relatively soft products. Thus a determination of the cooling time through any one of the three temperature ranges used appears to be as suitable as the remaining two for correlating with the microstructure in evaluating the hardenability of these alloys. Obviously, however, the values used to express the hardenability in terms of the critical cooling time or rate will vary with the temperature ranges used. Since a determination of the cooling rate through the range, 1,110° to 930° F (nose of S-curve) was used in previous investigations to evaluate the hardenability of high purity iron-carbon alloys, this temperature range was again selected for use in the present study. The critical cooling rate, therefore, is taken as the average cooling rate between 1,110° and 930° F (600° to 500° C) which produced in, the quenched specimen a structure of martensite with fine pearlite in an amount estimated to be 0.2 percent.

The relation of critical cooling rate to quenching temperature of initially homogenized specimens of iron-carbon alloys, without and with boron, is shown in figure 11. For alloys without boron, the critical cooling rate decreased continuously with increase in quenching temperature when the carbon content was 0.32 percent (B8), but the critical cooling rate of the alloys with 0.50- or 0.54-percent carbon (B7 and B12) was not appreciably affected by changes in quenching temperatures within the range from 1,425° to 2,000° F. With 0.70-percent carbon (B10), the critical cooling rate was approximately constant when the alloy was quenched from temperatures within the range of about 1,425° to 1,600° F, the rate decreased rapidly with change in quenching temperature from about 1,600° to 1,800° F and then less rapidly with a further increase in quenching temperature.

For the alloys with boron, the critical cooling rate decreased continuously with increase in quenching temperature when the carbon was 0.47 percent (B2), but with 0.74-percent carbon (B5) the rate was constant for quenching temperatures up to 1,600° F. The critical cooling rate of the latter alloy decreased somewhat with increase in quenching temperature from 1,600° to 2,000° F. As previously stated, no consistent relationship was shown between the cooling rate and structure produced by quenching initially homogenized specimens of the 0.32-percent carbon—0.0021-percent boron alloy (B6).

The influence of boron on the hardenability of alloys with about 0.5- and 0.7-percent carbon is shown by a comparison of the positions of the curves of figure 11. The improvement in hardenability of the boron-treated alloys was confined principally to the high range in quenching temperatures for the alloys of the 0.5-percent carbon type and to the low range when the carbon content was about 0.7 percent. Apparently this improvement is a secondary effect, possibly due to a change in the grain size at the austenitizing temperatures.

The relation of critical cooling rate to austenite grain size of the iron-carbon alloys is given in figure 12. The general trend was for the hardenability of the alloys, without and with boron, to increase (critical cooling rate decreased) as the size of the austenite grains increased. The critical cooling rate of the 0.74-percent carbon—0.0028-percent boron alloy ranged from about 500° to 900° F per second without an appreciable change in austenite grain size.

To determine the primary effect of boron on hardenability, a comparison should be made of the critical cooling rate of alloys of the same carbon content, without and with boron, when quenched from temperatures sufficiently high to ensure complete solution and uniform distribution of carbon in austenite of the same grain size. Unfortunately, in the present experiments these conditions were not met for wide ranges in both carbon content and size of the austenite grains. However, the data obtained from figure 12 permit such a comparison to be made of the alloys with austenite grain sizes of about 10 and 5 grains/in.^{2} at 100 diameters (ASTM No. 4 and 3). When the critical cooling rate is plotted against the carbon content of the alloys each with the same austenite grain size (10 or 5 grains/in.^{2} at $\times 100$), no significant improvement is shown in the hardenability due to boron (fig. 13).

It is noteworthy that a change in austenite grain size of about one ASTM number of a given boron-free alloy initially as homogenized had considerably more effect on its hardenability than the addition of about 0.002 percent boron, provided the austenite grain size was not changed.

Specimens initially as cast. The hardenability

high-purity-iron-carbon-boron alloys may be fected by hot-working, or thermal treatments rried out during the course of their preparation. ests, therefore, were made on specimens prepared om boron-treated ingots (as cast) containing 0.32, 47, and 0.74 percent of carbon, respectively 6, B2, and B5) and on a boron-free alloy with 0.50 rcent of carbon (B7). The effect of the initial ructural condition on the hardenability of the 50-percent carbon alloy without boron was not arked; slightly higher critical cooling rates were quired with initially cast than with homogenized ecimens when the quenching temperature was ithin the range of about 1,500° to 1,600° F and wer rates in the former specimens when quenched om 2,000° F.

The relation of cooling time to structure of ecimens, initially as cast, of the 0.32-percent car- on—0.0021-percent boron alloy when quenched om different temperatures is given in figure 14. he curves show the relation of critical cooling me to quenching temperature. More consistent sults were obtained with these specimens than ith those prepared from the homogenized bar of e same alloy (fig. 5).

The relation of critical cooling rate to quenching mperature of some of the alloys initially as cast urves A) and initially as homogenized (curves B) summarized in figure 15. With an initial struc- re as cast, the hardenability was markedly im- oved by the addition of boron to alloys contain- g 0.32- or 0.47-percent carbon, but the presence boron in the 0.74-percent carbon alloy again had o material effect on the critical cooling rate. he lower hardenability of the initially cast ecimens of the 0.74-percent carbon alloy when enched from 1,425° or 1,500° F was due to omplete solution and nonuniform distribution carbon in austenite at these temperatures, as idenced by the presence of free carbides after enching. As previously stated, the initially omogenized specimens of the 0.32-percent car- on—0.0021-percent boron showed nonuniform rdening characteristics. Because of this con- tion, it was necessary to use the results obtained ith initially homogenized specimens of the alloy ithout boron as a basis for evaluating the effect initial structure on the hardenability of the oron-treated alloy containing 0.32-percent car- n. Considerably higher cooling rates were quired to completely harden the 0.32- and 0.47-percent carbon alloys in the initial condition as homogenized than as cast when quenched from alike temperatures within the range of 1,500° or 1,600° to 2,000° F.

The observed difference in hardenability cannot be ascribed to a grain-size effect, as the sizes of the grains established at the austenitizing temperatures for 0.47-percent carbon 0.0020-percent boron alloy were nearly alike in the two series of specimens, and the average size of the austenite grains obtained at each austenitizing temperature of the 0.32-percent carbon—0.0021-percent boron alloy was slightly finer in the initial condition as cast than as homogenized (table 2). As boron improved the hardenability of the two alloys (0.3 and 0.5% carbon) in the initial condition as cast but was practically without effect after hot-working and homogenizing, it is clearly apparent that the action of boron on hardenability was adversely affected during the course of these treatments, probably by the exposure to the relatively high temperature required for forging. In carrying out the forging operation, the ingots (1 to 1½ in. in diameter) were placed in a furnace within the temperature range of 1,900° to 2,100° F, in a reducing atmosphere, held in the furnace for ¾ to 1 hr and then forged, without reheating, with a drop hammer to approximately ½ in. in diameter; forging was completed at a temperature above Ar_3, and the forged bars were cooled in air. Microscopic examination of cross sections of the forged bars showed the presence of a decarburized layer at the surface of the 0.47-percent carbon alloy (B2) and no appreciable decarburization of the 0.32-percent carbon alloy (B6). The usual procedures as previously described were followed in removing the outer surfaces from the forged bars and in carrying out the homogenizing treatments.

There was no pick-up in the amounts of nitrogen or oxygen during the forging and homogenizing operation as shown by the results of analysis by the vacuum fusion method on specimens of the 0.32-percent carbon alloy (B6). The results of determinations for boron by chemical analysis on bars as forged (B2) or as homogenized (B6) showed the presence of sufficient boron (0.002%, table 1) to enhance the hardenability of each alloy.

Grange and Garvey [4] also found that when a boron-treated steel is heated at a very high temperature for a very long time, the increase in

hardenability due to boron gradually diminishes and finally disappears, although the boron content as measured by analysis remains unchanged. They express the opinion that possibly part or all of the efficacy of boron in enhancing hardenability is lost when the steel is heated for rolling or forging.

The results summarized in figure 15 for initially cast specimens also show that the boron-treated alloys containing 0.32-percent and 0.47-percent carbon had critical cooling rates of the same order of magnitude when austenitized alike, and these rates were, in all cases, slower than those of the boron-treated alloy containing 0.74-percent carbon; in hypoeutectoid plain-carbon steels, the hardenability increases with an increase in carbon content, provided all other factors that affect hardenability are alike. Thus the action of boron on the hardenability of these high-purity alloys, as cast, varied with their carbon content; the effectiveness decreased with an increase in carbon, the improvement being very pronounced with 0.3-percent, intermediate with 0.5-percent, and nil with 0.74-percent carbon. Rahrer and Armstrong [21] and Grange and Garvey [4] also reported the above trends with commercial steels.

The hardenability of certain commercial boron-treated [4] and experimental [1] steels decreased with an increase in quenching temperature. It is interesting, however, to note from the results given in figure 15, that the hardenability of these boron-treated alloys did not decrease with an increase in quenching temperature.

(b) Iron-Carbon-Manganese Alloys

Critical Cooling Rate. The relation of cooling time to structure of the iron-carbon-manganese alloys, without and with 0.0024-percent boron, when quenched from various temperatures, is shown in figures 16 and 17, respectively, and the relation of critical cooling rate to quenching temperature is given in figure 19. Variation in quenching temperature from 1,500° to 2,000° F had no material effect on the critical cooling rate (fig. 19) or average size of the austenite grains (table 2) of the alloy without boron (B13), whereas with the boron-treated alloy (B14) the trend was for the hardenability to increase slightly with temperature and for the grain size to increase with a change in temperature from 1,600° to 2,000° F.

End-Quench Test. The curves obtained from the results of the end-quench test of the iron-carbon-manganese alloys are given in figure 1 and the relation of quenching temperature to the distances from the quenched end of the bar corresponding to Rockwell hardness values of C42 (50% martensite) and C50 (95% martensite) are shown in figure 19.

When a comparison is made on the basis of the distances from the quenched end for Rockwell values of C42 or C50 (fig. 19), the hardenability of each alloy was increased slightly by a change in quenching temperature from 1,500° to 1,700° F but there was no further improvement by increasing the temperature to 1,900° F. The observed improvement in hardenability with a change in quenching temperature from 1,500° to 1,700° may be due to a grain size effect.

The effect of boron on the hardenability of the iron-carbon-manganese alloys as determined by critical cooling rate and by the end-quench test is also shown by the results summarized in figure 19. For each austenitizing temperature used, the hardenability was enhanced by the presence of boron. This improvement appears to be a primary rather than a secondary effect, as the differences in grain size of the alloys at each temperature is insufficient to account for the magnitude of the observed effects. For example, the specimens of both alloys used for determining the critical cooling rate had approximately the same grain size at 1,500° and 1,600° F, but the hardenability of the alloy containing boron was considerably higher than that of the alloy without boron; part of the observed increase in hardenability of the boron-treated alloy when quenched from within the temperature range of about 1,700° to 2,000° F may be due to its larger grains (table 2).

The increase in hardenability of the iron-carbon-manganese alloys by the addition of boron was considerably more marked when measured in terms of the critical cooling rate than by the end-quench test.

(c) Commercial Steels

End-Quench Test. It was shown previously [1] that the hardenability as determined in the end-quench test of certain boron-treated experimental and commercial steels was affected by the quenching temperature. In some of the steels, the hardenability was increased by increasing the quench-

ing temperature above the usual recommended range; whereas in other steels the hardenability was not affected, or was decreased by this change. With specimens initially normalized from the usual recommended temperature range, it was shown [1] that variations in quenching temperature from 1,550° to 1,900° F had no material effect on the hardenability of boron-treated steels (table 1) C14 (0.0036% B), and C19 (0.0001% B); the hardenability of the base steel C15 (without boron) increased slightly by increasing the quenching temperature from 1,550° to 1,900° F, but the hardenability of another boron-treated steel C12 (0.0022% B) was decreased somewhat by increasing the quenching temperature from about 1,550° or 1,650° to 1,900° F. Several of these commercial open hearth steels (table 1), all prepared from the same heat, were selected for use in a further study of the factors, such as variations in initial structure, austenite grain size, etc., that might influence the hardenability.

The results of some of the end-quench tests made on the commercial steels containing 0.43-percent carbon, 1.6-percent manganese, and varying amounts of boron are summarized in figure 20.

The influence of boron on the hardenability of these steels when normalized and quenched from the usually recommended temperatures is shown by the relative position of the curves in figure 20A. The hardenability of each steel (C9, C12, C14, and C19) was markedly improved by boron, but the retention of 0.0001 percent was nearly as effective as retaining 0.0036 percent. As these results were obtained on specimens that were normalized and end-quenched from recommended temperatures, the curves are used as a basis for correlating the hardenability of the steels after various thermal treatments.

A change in normalizing temperature from 1,650° to 1,900° F followed by end-quenching from 1,550° F did not appreciably affect the hardenability of the base steel (C15), or boron-treated steels C9, C14, (fig. 20, B) and C12, but the hardenability of steel C19 with 0.0001-percent retained boron was decreased slightly by this change. The hardenability of these steels was not significantly affected by quenching from 1,900° F in water prior to end-quenching from 1,550° F, as is illustrated for steels C15, C9, and C19 in figure 20, C (C14 not included in the test). That steel C19 is sensitive to prior thermal treatment is clearly shown by the results summarized in figure 20, D, E, and F. Its hardenability was of the same order of magnitude as the base steel when the specimens were treated alike by heating to 1,900° F followed by cooling in another furnace at either 1,550° or 1,425° F for 30 min before end-quenching (fig. 20, D and E). However, the hardenability of the steels with higher boron content was not appreciably affected by these treatments (steel C12, fig. 20, D and steels C9 and C14, fig. 20, E). Furthermore, the hardenability of steels C9 and C14 was not changed by increasing the time of holding at 1,425° F from ½ to 5 hr. before end-quenching. The slight improvement in the hardenability of the base steel (compare curves of steel C15, fig. 20, A and E) was probably due to an increase in grain size with the higher austentizing temperature (1,550° and 1,900° F, respectively). The hardenability of boron-treated steel C19 was also impaired by an initial treatment that consisted of heating to 1,900° F, cooling in another furnace at 1,425° F for 30 min, and then quenching in water before end-quenching from 1,550° F (fig. 20, F). The hardenability thus impaired (specimen C19 A), however, was restored to approximately its normal value by increasing the temperature of the end-quench test from 1,550° to 1,750° F (specimen C19 B).

VI. Effect of Quenching Temperature on Ar″ Transformation

Many of the photographic records obtained during the continuous cooling of small specimens by quenching directly from various austenitizing temperatures showed an arrest in the cooling curve in the temperature range of martensite formation. The clarity of the arrest as shown in the photographs and from a plot of the time-temperature cooling curve varied with the carbon content of the alloys and with the rate of cooling. A summary of the data from these photographic records indicated a very definite trend for the temperature of the start of the transformation of austenite to martensite (start of the Ar″ or Ms) in the high-purity alloys to increase with increase in quenching temperature. Because of this unexpected relation, attempts were made to obtain the Ms point in several of the alloys (B2, B7, B13, and B14) by a quench-temper technique as described and used by Greninger and Troiano [22]. These alloys,

however, are relatively shallow hardening, and the Ms point was not accurately determined by this method. A deeper-hardening commercial steel (C14) was, therefore, selected for determining, both by thermal analysis and by the metallographic method, the influence of quenching temperature on the temperature of the Ms point.

Specimens of steel C14 were quenched directly from the austenitizing temperatures and the temperatures of the start of the formation of martensite were obtained from the photographic records in the usual manner. The procedures as already described for preparing small specimens, heating, quenching, and recording the cooling curves, were also followed in carrying out these tests. The average value as determined from cooling curves on two to four specimens quenched from each of the selected temperatures are given in figure 21. Again the trend was for the temperature of Ms to increase with increase in quenching temperature. However, additional tests on specimens that were austenitized at either 1,900° or 2,000° F and then cooled and held in the temperature range of 1,500° to 1,600° F before quenching, showed values for the Ms temperature that were only slightly higher than those obtained in austenitizing and quenching directly from the lower temperatures. Other specimens that were austenitized at 2,000° F and then cooled, without decomposing the austenite, to a temperature within the range of about 1,100° to 900° F before quenching, gave an average value for the Ms point that was about the same as that obtained on quenching directly from 1,600° F. Furthermore, the results of determinations by the metallographic method show no appreciable difference in the temperature of the Ms point with quenching temperatures of 1,600°, 1,800°, and 2,000° F. The observed increase in the Ms temperature with increase in quenching temperature is apparently due to the method of thermal analysis and is probably not a characteristic of the alloys.

The average size of the austenite grains in specimens of steel C14 ranged from about ASTM grain number 5 to 2 with change in temperature from 1,550° or 1,600° to 2,000° F. This range in grain size had no significant effect on the temperature of the start of the formation of martensite as determined by the metallographic method.

VII. Diffusion of Boron in Austenite of Commercial Steels

The penetration of boron in low-carbon ste has been investigated by Tschischewsky [23] an by Campbell and Fay [24]. According to Cam bell and Fay, the boron and carbon steels sho many similarities in the mechanism of their ab sorption and diffusion phenomena. In the ab sence of nitrogen, they found that the penetrati of boron followed a normal diffusion curve b when a boron-treated specimen was heated 900° C in ammonia, the nitrogen displaced th boron at its surface. They concluded that 900° C boron had a greater affinity for nitroge than it had for iron.

Specimens of three of the commercial boro treated steels (C11, C12, and C14, table 1) we decarburized by heating in a reducing atmosphe (mixture of natural and manufactured gas wit air, moisture not removed) at 1,550° or 1,900° for 8 hr and then cooled in mica. The depth decarburization was estimated metallographicall and the boron content in the decarburized lay was determined spectrographically. The result obtained are summarized in table 3 and illustrate in figure 22. The depth of the decarburized lay of a specimen of steel C14 decarburized at 1,900° is shown by the structure reproduced in the photo micrograph at the top of figure 22, and the heav horizontal line represents the nominal boro content (0.0038 %) as determined spectrograph cally. There was a high concentration of boron the original surface of the specimens, which prob ably was due to a reaction of the diffusing boro with oxygen in the furnace atmosphere to for boron oxide (B_2O_3); the specimens were colore dark during the decarburizing treatment. Th boron content slightly below the original surfa (about 0.003 in. for specimens of C14, fig. 22) w usually less than the value that could be accurate determined by the methods employed (limits sensitivity were about 0.0002 and 0.0005 % boron A concentration gradient extended from this zo where the boron was practically depleted to depth usually as great or greater than the severe decarburized layer. The approximate value of th coefficient of diffusion of boron (D) as compute from experimental results obtained with th

specimen [2] also indicated that the rate of diffusion of boron in gamma iron was of the same order of magnitude as that of carbon. Thus the rate of diffusion of boron in austenite at 1,550° or 1,900° F appears to be equivalent to or slightly greater than that of carbon in steels containing 0.4 percent of carbon. It is therefore logical to assume that the mechanism of the diffusion process for boron in austenite is quite similar to that of carbon. That is, the boron atoms are located in the interstices of the gamma iron lattice.

VIII. Structures of the Alloys and Steels

A metallographic examination was made of the high-purity alloys used to evaluate hardenability in the conditions as cast, forged, and homogenized. The examination was extended to include specimens specially heat-treated to develop a constituent containing boron in each of the boron-treated alloys and steels listed in table 1. Some of the specimens containing a boron constituent were examined with an electron microscope.

1. Initially as Cast and as Homogenized

Numerous particles in the form of spheroids and stringers were observed in the structures of the boron-treated alloys containing 0.3-, 0.5-, and 0.7-percent carbon in the conditions as cast and as homogenized, as is illustrated in the photomicrographs of figure 23. The trend was for the particles to form in the ferritic areas especially when the proeutectoid ferrite was located in the parent austenite grain boundaries. These particles appear to be carbides, some of which are complex (fig. 23, E), as is indicated by their reaction to a picral or nital etch (differentially attacked, fig. 23, E, not appreciably attacked, fig. 23, A, B, and C) and to an electrolytic etch in a sodium cyanide solution (attacked, fig. 23, F). The results of micro hardness measurements using the Knoop instrument with a 25-g load also indicated that the particles were harder than the ferrite matrix. The carbide particles also were observed in the primary austenite grain boundaries of polished but unetched specimens of the 0.47-percent carbon—0.0020-percent boron alloy as cast (B2, fig. 23, D). Since the free carbide particles were observed principally in the high-purity alloys containing boron, it is logical to believe that most of these particles are cementite containing boron.

TABLE 3.—*Boron content of decarburized layer of commercial boron-treated steels*

The limits of sensitivity of the spectrographic methods were 0.0002-percent for the low, and 0.0005-percent boron for the high concentrations. These determinations were confined to layers 0.004 and 0.002 in. immediately below the surfaces, respectively. Each value for boron given in the table is the result of a single determination, and the depth is that of the surface at which the arc was struck, not the depth to which the pit due to the arc extended. The specimens were ground to the desired depths with boron-free wheels.

Depth [1]	Boron-content of specimen—		
	C11	C12	C14
Decarburized 0.025 to 0.04 in.[2]			
in.	%	%	%
0.000	0.030	0.029	0.051
.001	.046	.017	.022
.002	<.0005	.0012	<.0005
.003	<.0002	<.0002	<.0002
.003	<.0002	<.0002	<.0002
.011	<.0005	<.0005	<.0005
.012	<.0005	<.0005	<.0005
.022	<.0005	<.0005	.0023
.022	<.0005	<.0005	.0023
.031	<.0005	<.0005	.0026
.032	<.0005	<.0005	.0028
.041	<.0005	<.0005	.0027
.042	.0005	.0006	.0031
.051	.0006	.0007	.0034
.051	.0007	.0013	.0030
.054	<.0005	.0011	.0027
.060	.0006	.0007	.0031
.063	.0005	.0007	.0032
.064	.0007	.0013	.0033
.077	.0008	.0021	.0036
.077	.0010	.0022	.0037
.090	.0010	.0021	.0038
Decarburized 0.01 to 0.02 in.[3]			
0.000	0.023	0.013	0.022
.001	<.0005	.0035	.0025
.001	----------	.0041	.010
.003	<.0002	.00055	.0021
.003	<.0002	.00035	.0017

[1] Distance from the surface of the specimen as decarburized. These surfaces were ground prior to decarburizing.

[2] The specimens were decarburized by heating at 1,900° F in a reducing atmosphere for 8 hr, followed by cooling in mica.

[3] The specimens were decarburized by heating at 1,550° F in a reducing atmosphere for 8 hr, followed by cooling in mica.

[2] The authors are indebted to Cyril Wells, Carnegie Institute of Technology, for computing and reporting the approximate value of the rate of diffusion of boron in this specimen (at 1,900° F, $D=2.0\times10^{-7}$ cm²/sec). Additional and considerably more precise tests to determine the rate of diffusion of boron in high-purity iron-carbon alloys containing 0.32 percent of carbon (B6 and B8) and in experimental and commercial steels under varying conditions are now in progress in that laboratory. The results will be published at a later date by Wells.

The structure of the alloys as cast and as homogenized consisted of proeutectoid ferrite, pearlite varying somewhat in degree of fineness, and spheroided carbides (fig. 23, A, B, C, E, and F). Obviously, the relative amounts of ferrite and pearlite varied with the carbon content.

2. Heat Treatments to Develop a Boron Constituent

Grange and Garvey [4] described a metallographic test for determining the presence of boron in steel, and they attempted to correlate the observed amounts of a constituent in specially treated specimens with the actual boron content and hardenability. Essentially, the test consists of austenitizing small specimens (about ⅛ in. thick) at a high temperature (2,000° to 2,100° F for 10 min.) followed by cooling rapidly in a lead or salt bath at 1,200° F (temperature of this bath may be changed to suit existing conditions), holding at this temperature for a sufficient time to allow the constituent to precipitate, and finally cooling to room temperature preferably by quenching in water or brine. The original surface layer of the heat-treated specimen is removed preparatory to polishing and then etching in picral for metallographic examination at a magnification of approximately 500 diameters. They found that the constituent (dark-etching dots) always formed as a partial or continuous network in the parent austenite grain boundaries of the specially treated specimens of steels containing a minimum of 0.0004-percent boron. The hardenability of their steels correlated somewhat better with the amount of boron constituent than with the actual boron content, but they concluded that the hardenability of boron-treated steels can be safely estimated only from the results of a hardenability test. The precise nature of the constituent was not known, but to the authors it appeared to be an iron boride probably containing carbon and other alloying elements.

A boron constituent was observed in specially treated specimens of the boron containing alloys and steels listed in table 1; only very small amounts were observed in a commercial steel with 0.0001-percent boron (C19) and possibly a trace in carburized specimens of iron-boron alloy (B13) initially with relatively high oxygen content. Some of these specimens were heat-treated according to the procedure recommended by Grange and Garvey, but other specimens heat-treated quite differently frequently contained this constituent. The results are illustrated in figures 24, 25, and 26.

The tendency for the carbides to spheroidize in high-purity iron-carbon-boron alloys is further illustrated in the photomicrographs of figure 24. Although this specimen, in cooling from 1,900° F, was held for only 1 min in the temperature range where pearlite is formed, the final structure indicates that the time was ample for some spheroidization of the carbides to occur in a coarse pearlitic area; the spheroids as shown extending linearly across the photomicrographs in figure 24, A and B, were attacked by etching electrolytically in a sodium cyanide solution. The dark etching dots (believed to be a boron constituent) in the martensite areas (fig. 24, C) are considerably smaller than the carbides located in the ferritic area. Additional study is needed to identify positively the former particles. It is of interest to note the continuity in the alinement of both size particles in the form of a partial network located in the prior austenite grain boundaries.

The trend was for the boron constituent to be concentrated in the parent ausenite grain boundaries of the specially treated specimens of the alloys and steels (fig. 25, A and B). However, some dark etching particles often were observed within the grains of these and of other specimens that were cooled rapidly, directly from high austenitizing temperatures, as is illustrated in figure 25, C and D. The result obtained on a small specimen of a commercial steel (C14) that was austenitized at 2,000° F and quenched into ice sodium hydroxide solution (fig. 25, C and D) indicates either that all of the boron (0.0036 %) was not in solution in the austenite at 2,000° F or that the formations of the precipitate cannot be entirely suppressed by extremely rapid cooling from this temperature. The constituent also was observed in other specimens of this steel that were cooled from the austenitizing temperature (2,000° F) in air or in oil.

Many of the data indicated that the solubility of boron in gamma iron decreased with an increase in temperature but, in a few cases, the results also indicated that the solubility increased with the temperature.

The number, size, and distribution of the boron-containing particles varied with the amount and form of boron and with the conditions used in heat treating the specimens, including austeniti-

ng temperature and atmosphere, rate of cooling, temperature of quenching bath, and time held in the bath if at elevated temperature, and temperature of reheating.

Furthermore, the success in revealing the presence of the boron constituent in these specimens varied appreciably from time to time, with the polishing and etching technique, as is illustrated in figure 25, C and D. Although a similar procedure for preparing this specimen was followed on two occasions by different persons, it is apparent that considerably more of the "dots" are shown within the parent austenite grains in figure 25, D, than in figure 25, C.

The boron constituent was observed in a specimen of a high-purity iron-boron alloy with less than 0.01-percent carbon that was heated to 2,000° F and then cooled in a lead bath at 1,700° F (gamma field) for 5 min and finally quenched in sodium hydroxide solution at room temperature (fig. 26, A). The dark etching constituent delineated the gamma (austenite) grains, and it also precipitated within the grains on parallel planes thus giving the appearance of twinning. Although no appreciable decarburization could occur during the austenitizing of this specimen (less than 0.01 % carbon) the boron constituent did not extend to its original surface; the left edge of the photomicrograph in figure 26, A, corresponds to the surface of the quenched specimen. Some, but not all, of the constituent was dissolved on reheating this specimen in lead at 1,650° F for 5 min; compare the amount of the constituent as shown in the photomicrograph of figure 26, C, with that of A and note in C that the ferrite grain boundaries appear to be located independently of the network.

If it is assumed that all the oxygen in this B4 alloy (0.008 % by vacuum fusion analysis) reacts with the boron to form a boron oxide of the composition B_2O_3, sufficient boron would still be available to produce the observed constituent. However, in another alloy (B3), which contained 0.011-percent oxygen and 0.0028-percent boron, there is not sufficient boron to react with all the oxygen to form this compound. Specimens of the latter alloy were subjected to various heat treatments, as summarized in table 4, preparatory to carrying out the metallographic examination in the usual manner. No boron constituent was observed in any of these specimens, thus indicating that the constituent is not an oxide of the metal boron. However, what might be traces of the constituent were observed in the carburized zone of specimens of this alloy that were pack carburized prior to the special treatment (designated as 9 in table 4).

TABLE 4. *Heat treatment of specimens of iron-boron alloy (B3 <0.01 percent carbon, 0.0028 percent boron) to develop a boron constituent*

Designation of treatment	Heat treatment [1]			
	Furnace		Lead bath	
	Temperature	Time	Temperature	Time
	°F.	min.	°F.	min.
1	2,300	2	.....	.....
2	2,000	3	.....	.....
3	2,000	7	.....	.....
4	2,000	3	1,200	2
5	2,000	3	1,200	5
6	2,000	3	1,300	1
7	2,000	3	1,500	2
8	2,000	3	1,600	5
9	2,000	3	1,700	5

[1] The procedure was to place the specimen in the furnace at temperature for the time as indicated and then either quench directly into sodium hydroxide at room temperature (treatments 1, 2, and 3) or transfer to a lead bath at temperature for time as indicated before quenching in sodium hydroxide at room temperature. A reducing atmosphere (graphite crucible containing powdered charcoal) was used in the furnace for carrying out treatments 3, 4, 5, and 6, and an oxidizing atmosphere (air) for the other treatments.

It should be pointed out that the particles composing the chain-like constituent appear, at high magnification, to be similar to inclusions, as is illustrated in figure 26, B. Possibly the constituent was dissolved by the acid (picric) or was removed by polishing and the two oval or round spots (fig. 26, B) are voids in the specimen. A preliminary examination of this and several other specimens with the electron microscope was unsuccessful in determining if these "dots" are merely voids. An attempt to measure the hardness of the boron constituent by means of microhardness tests (Knoop instrument or Tukon Tester) also was unsuccessful.

The ease with which this constituent was formed and observed in specimens of the high-purity alloys varied with the initial structural conditions. Usually, the constituent was considerably more pronounced in specially treated specimens prepared from the as-cast ingots than from homogenized bars. In some of the latter specimens it was recognized metallographically with certainty only in an occasional field, but it

was never observed in severely decarburized portions of any of the specimens from the alloys and steels (fig. 26, A).

Specimens prepared from various experimental high-nitrogen steels described in a previous report [1] were subjected to different treatments to develop the boron constituent. The constituent was not observed in the specimens containing high-soluble nitrogen (0.01 to 0.03 % soluble in sulfuric acid), whereas it was readily produced in specimens of steels containing similar amounts of nitrogen that were treated with titanium to fix the nitrogen as titanium nitride. Thus the boron constituent is not a nitride. Presumably compounds of boron and oxygen or boron and nitrogen existed in specimens of the high-oxygen alloys or high-soluble nitrogen steels containing boron in which the chain-like constituent was not developed. It should be pointed out that such compounds were not identified in these specimens as polished and unetched or as etched. The boron constituent developed in these tests therefore, was not an oxide or a nitride, and it does not appear to be a carbide. Its exact identification is not established, but it is believed to be an iron boride.

Attempts were made to correlate the boron constituent, as observed in specially heated specimens with the hardenability of the high-purity alloys and some of the experimental high-nitrogen steels. As previously stated, the boron constituent was observed in specimens prepared from the ingots and from homogenized bars of the boron-treated alloys containing 0.32, 0.47, and 0.74 percent of carbon, but in some of the initially homogenized specimens the amount of the constituent was considerably less than that of specimens from the ingots. The hardenability of all the initially homogenized alloys and of the 0.74-percent-carbon alloys as cast was not materially enhanced by boron. With the high-nitrogen steels the hardenability as determined in the end-quench test was not significantly improved by the addition of boron and no boron constituent was observed in the metallographic test when the soluble nitrogen was relatively high whereas the hardenability was increased by boron and the constituent was observed when the nitrogen was fixed with titanium.

It is clear, therefore, that the presence or absence of the boron constituent as determined by the metallographic test often indicates the response in hardenability of the steel to a boron treatment but it is not always a reliable criterion of this effect.

IX. Mechanism of Boron Effect on Hardenability

A summary of the present results and those published previously strongly supports the belief of the authors that the effectiveness of boron in enhancing the hardenability of certain steels is due entirely to its action while in solid solution in austenite. Only the portion of the boron that is in solution at the time of quenching contributes toward an increase in hardenability. The boron undissolved or in the form of compounds is either without effect, or possibly decreases hardenability by acting as transformation centers for austenite in the temperature range where pearlite is formed.

In addition to dissolving in austenite, boron can exist in steel in the form of compounds with nitrogen, oxygen, iron, and carbon. Some of these compounds are stable and are not decomposed at temperatures ordinarily used in the heat treatment of boron-treated steels, whereas other compounds containing boron may be partially or entirely decomposed at these temperatures. Some data indicate an increase in solubility of boron in gamma iron with increasing temperature, whereas other results indicate a decrease in solubility with increasing temperature in this field. In any event, only a very small amount of boron is retained in solution at heat-treating temperatures, and it is possible to obtain the maximum response in the hardenability of certain steels by relatively minute additions of this element.

With steels, isothermally transformed, it was shown [19] that the addition of boron did not decrease the rate of formation of pearlite in the temperature range just below Ae_1 (coarse pearlite), but boron had a marked effect in retarding the rate of formation of pearlite in the temperature range corresponding to the nose of the S-curve (fine pearlite). Pearlite is formed by a process of nucleation and growth. It has also been shown [25] that the rate of growth is the governing factor in the rate of formation of coarse pearlite, whereas the rate of nucleation is the controlling factor in the rate of formation of fine pearlite. When boron enhances the hardenability of a steel, therefore, it decreases the rate of nucleation and not the

rate of growth of ferrite and carbide. The boron atom, believed to be located interstitially in the gamma iron lattice, is effective in retarding either the rate of formation of nuclei or the rate of their growth to the critical size necessary for transformation to begin, or both.

X. Summary

A series of high-purity iron-carbon alloys varying in carbon content and other high-purity alloys containing 0.4 percent of carbon and 0.7 percent of manganese were prepared for use in this investigation. Several steels from a commercial open-hearth heat also were included in the testing program. The hardenability of the iron-carbon alloys as affected by variations in initial structural conditions and in quenching temperature and of the iron-carbon-manganese alloys as affected by variations in quenching temperature was determined in terms of the critical cooling rate. In addition, the end-quench test was used for determining the hardenability of the iron-carbon-manganese alloys in some of the experiments carried out with the commercial steels. Wide use was made of the metallographic test described by Grange and Garvey [4] for detecting the presence of boron in the form of a constituent in specially treated specimens of the high-purity alloys, commercial steels, and other experimental steels containing high nitrogen.

The addition of 0.002 percent of boron had no material effect on the austenite grain size or grain coarsening temperatures of the high-purity alloys. As these alloys were not deoxidized, except with carbon and in one alloy by some aluminum picked up from the crucible, the test specimens contained intermediate or coarse grains at relatively low austenitizing temperatures.

The general trend in the high-purity alloys, without and with boron, was for the critical cooling rate to decrease (hardenability increase) as the size of the austenite grains increased.

The influence of boron on the hardenability of the iron-carbon alloys varied with the initial condition of the alloys and with the carbon content. The hardenability of the alloys containing 0.3, 0.5, and 0.75 percent of carbon initially as forged and homogenized and the 0.75-percent-carbon alloy as cast was not significantly affected by the addition of boron. However, the hardenability of the ingots (as cast) containing 0.3 and 0.5 percent of carbon was markedly improved by the boron. Each of these two ingots showed approximately the same degree of hardenability, and they were somewhat deeper hardening than the boron-treated 0.75-percent-carbon alloy.

The hardenability of initially forged and homogenized iron-carbon-manganese alloy was enhanced by the presence of boron.

Evidence was obtained that the response in hardenability of a commercial steel containing 0.0001 percent of boron was sensitive to prior thermal history. The hardenability of this steel was first impaired and then restored to its normal value by certain heat treatments.

Boron was lost in the decarburized zone of commercial steels. Evidence indicated that the diffusion rate of boron in austenite is of the same order of magnitude as that of carbon.

A boron constituent was observed in specially treated specimens of the iron-carbon and iron-carbon-manganese alloys and in an iron-boron alloy with 0.011 percent of boron. It was not observed in similarly treated specimens of an iron-boron alloy containing relatively high oxygen and 0.003 percent of boron (except possibly a trace in specimens initially packed carburized) or in some experimental boron-treated steels containing high-soluble nitrogen. Thus the number, size, and distribution of the boron-containing particles varied with the amount and form of the boron and also with the conditions used in heat treating the specimens. The presence or absence of a boron constituent as determined in the metallographic test often indicated the response in hardenability of the alloy or steel to the boron treatment, but the test was not always a reliable criterion of this effect.

The effectiveness of boron in increasing the hardenability of certain alloys and steels is believed to be due to its action in retarding the rate of nucleation of ferrite and carbide while in solid solution in austenite.

The authors are indebted to Ellen H. Connelly and G. De Vries, former members of the section, for assistance in preparing the high-purity alloys and in carrying out some of the tests. The spectrographic analyses were made by C. H. Corliss, chemical analyses by J. L. Hague and K. D. Fleischer and gas analyses by J. T. Sterling.

XI. References

[1] T. G. Digges and F. M. Reinhart, J. Research NBS **39,** 67 (1947) RP1815.

[2] M. Hansen, Der Aufbam der Zweistofflegierungen (von Julius Springer, Berlin, 1936). (Iron-boron system, fig. 127, p. 274).

[3] International Critical Tables **2,** 450.

[4] R. A. Grange and T. M. Garvey, Trans. Am. Soc. Metals **37,** 136 (1946).

[5] T. W. Lippert, Iron Age **150,** 41 (Nov. 19, 1942).

[6] H. T. Chandler and M. A. Bredig, discussion of paper by Grange and Garvey [4].

[7] M. G. Corson, discussion of paper by Grange and Garvey [4].

[8] H. A. Allen, Steel **112,** 67 (Feb. 15, 1943).

[9] R. S. Dean and B. Silkes, Boron in iron and steel, Information Circular, Bureau of Mines [IC 73 63] (Sept. 1946).

[10] G. H. Boss, Metal Progress **51,** 265 (Feb. 1947).

[11] M. A. Grossmann, Hardenability calculated from chemical composition, Metals Tech. (June 1942) TP1437.

[12] Preparation of micrographs of metals and alloys, Am. Soc. Testing Materials Designation: E2–44T, Am. Soc. Testing Materials Standards, part I, Metals, p. 1875 (1944).

[13] S. J. Rosenberg and T. G. Digges, Trans. Am. Soc. Metals **29,** 638 (1941); J. Research NBS **25,** 215 (1940) RP1322.

[14] H. J. French, Trans. Am. Soc. Steel Treating **17,** 798 (1930).

[15] A. L. Boeghold and E. W. Weinman, Metal Progress **51,** 96–B (Jan. 1947).

[16] C. B. Post, M. C. Fetzer, and W. H. Fenstermacher, Trans. Am. Soc. Metals **35,** 85 (1945).

[17] Tentative method of end-quench test for hardenability of steel, Am. Soc. Testing Materials Designation A 255–42T, Am. Soc. Testing Materials Standards, part I, Metals, p. 1106 (1942).

[18] M. A. Grossmann, M. Asimow, and S. F. Urban, Hardenability, its relation to quenching and some quantitative date, Hardenability of alloy steels, p. 125 (Published by the Am. Soc. Metals, 1939).

[19] United States Steel Corp., Research Laboratory, Atlas of isothermal transformation diagrams (1943).

[20] T. G. Digges, Trans. Am. Soc. Metals **29,** 285 (1941); J. Research NBS **24,** 723 (1940) RP1308.

[21] G. D. Rahrer and C. D. Armstrong, Trans. Am. Soc. Metals **40,** 1099 (1948).

[22] A. B. Greninger and A. R. Troiano, Trans. Am. Soc. Metals **28,** 537 (1940).

[23] N. Tschischewski, J. Iron Steel Inst. **95,** 185 (1917).

[24] T. P. Campbell and H. Fay, Ind. Eng. Chem. **16,** 719 (1924).

[25] Robert F. Mehl, Trans. Am. Soc. Metals **29,** 825 (1941).

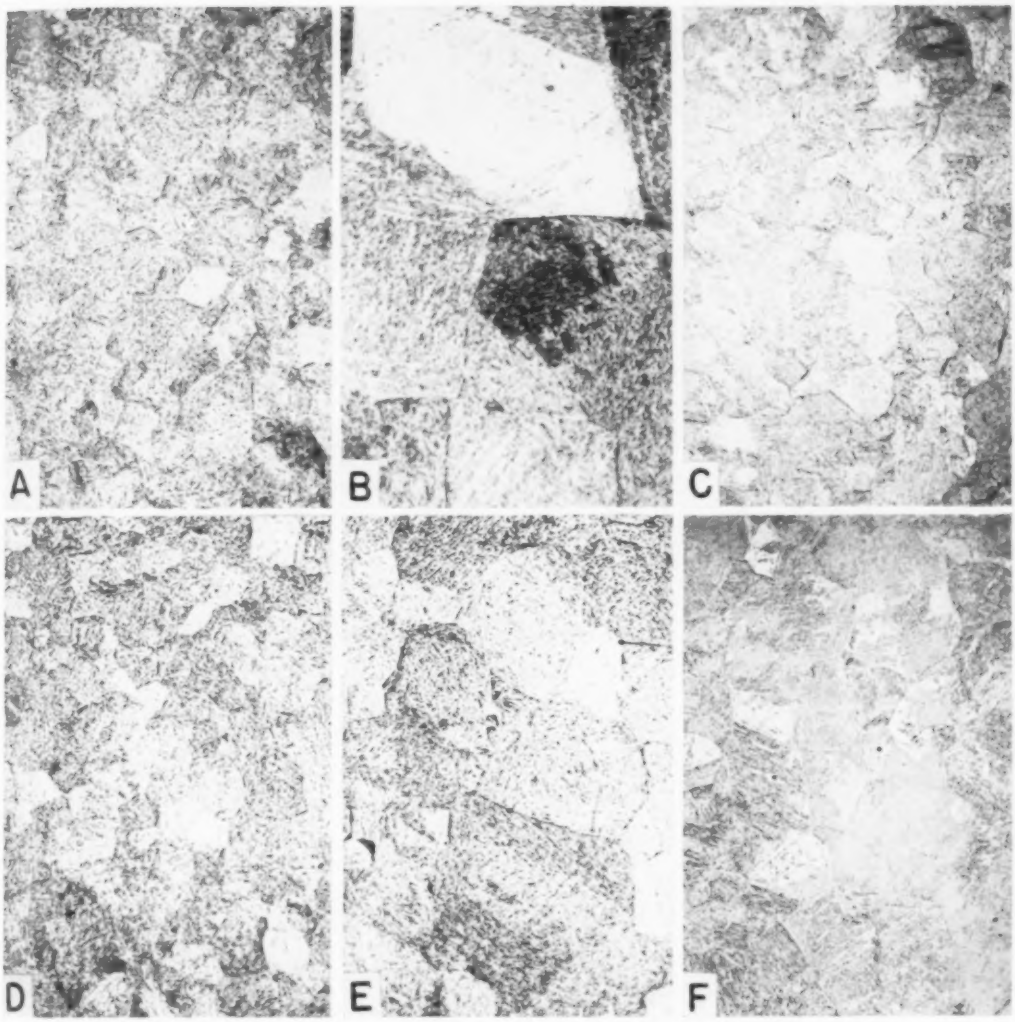

FIGURE 1. *Effects of boron and temperature on the austenite grain size of high-purity alloys.*

Etched with 1-percent picric—5-percent hydrochloric acid in alcohol, ×100.

Figure	Alloy	Percentage of—			Temperature	ASTM grain No.
		C	B	Al		
					°F	
A	B14	0.41	0.0024	0.003	1,500	4
B	B14	.41	.0024	.003	2,000	0
C	B12	.54	None	<.001	1,800	4
D	B2	.47	0.0020	Not detected	1,800	4
E	B2	.47	.0020	Not detected	1,800	1
F	B12	.54	None	<0.001	1,800	3

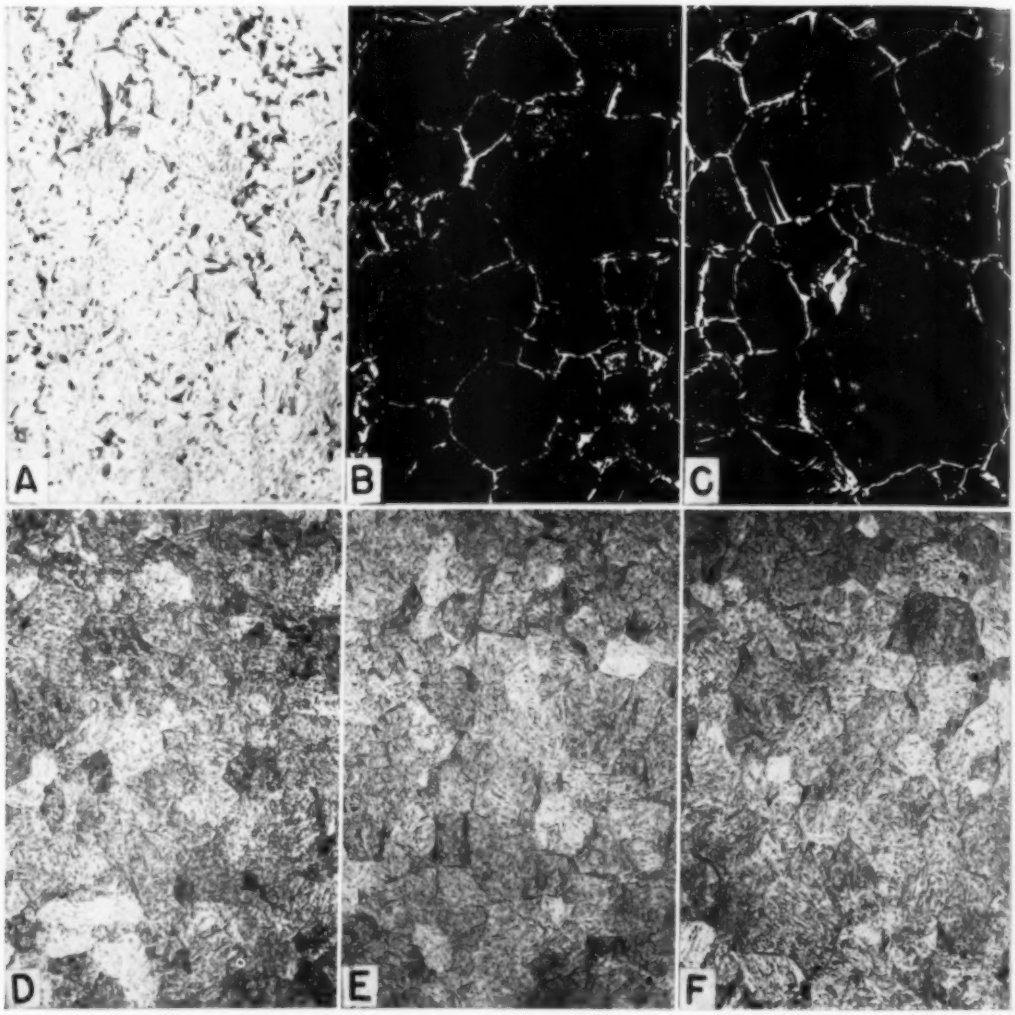

FIGURE 2. *Effects of rate of heating, temperature, and time at temperature on the austenite grain size of the 0.42-percent-carbon—0.67-percent-manganese alloy without boron (B13)*

A, B, C,—Photomicrographs of specimens, 1 in. in diameter by 4 in. long, heated relatively slowly to 1,500°, 1,700°, or 1,900° F, respectively, and held at temperature for 30 to 35 min (in furnace for 45 min); etched with 1-percent nital, x100. D, E, F—Photomicrographs of specimens, 1/10 by 1/10 by 0.04 in., heated relatively rapidly to 1,500°, 1,700°, or 1,900° F, respectively, and held at temperature for 15 min (in furnace for 17 min); etched with 1-percent picric—5-percent hydrochloric acid in alcohol, x100.

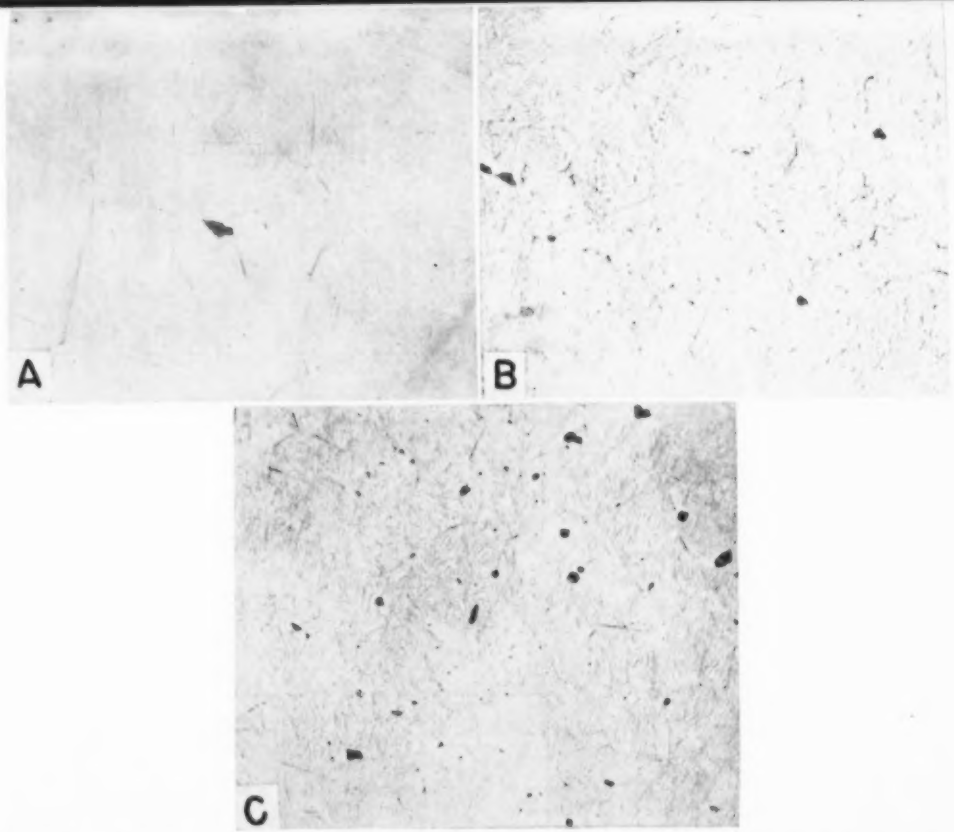

FIGURE 3. *Photomicrographs used as a "standard" for estimating the amounts of fine pearlite in the quenched specimens.*

Pearlite (dark) in a matrix of martensite. Etched with 1-percent nital, x100. A, Trace pearlite; B, 0.2-percent pearlite (amout corresponds to that produced when the specimen was cooled at the "critical rate"); C, 1.0-percent pearlite.

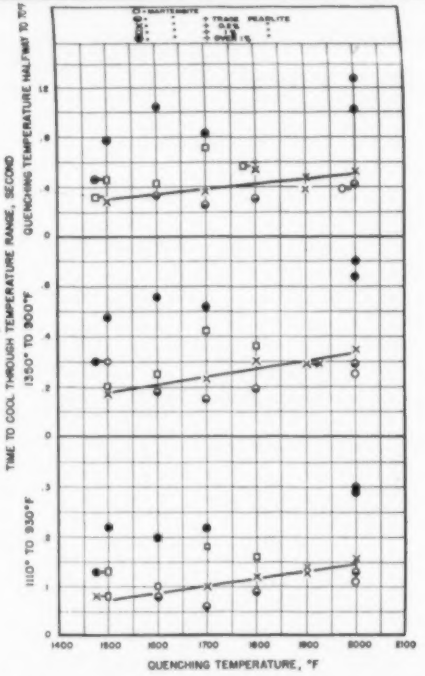

FIGURE 4. *Effect of cooling time on the structure of the 0.32-percent-carbon alloy (B8) quenched from different temperatures.*

The specimens were prepared from a homogenized bar.

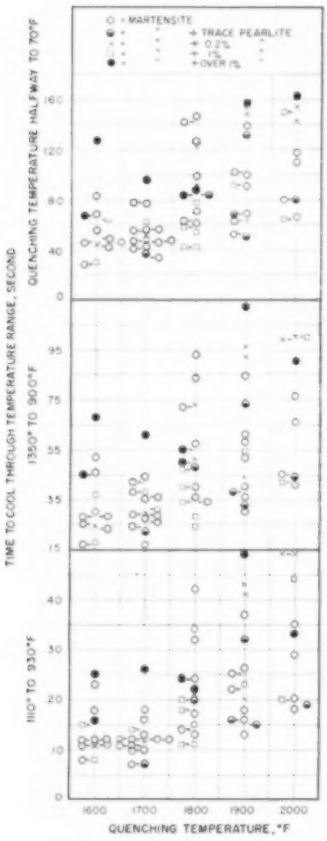

FIGURE 5. *Effect of cooling time on the structure of the 0.32-percent - carbon — 0.0021 - percent - boron alloy (B6) quenched from different temperatures.*

The specimens were prepared from a homogenized bar.

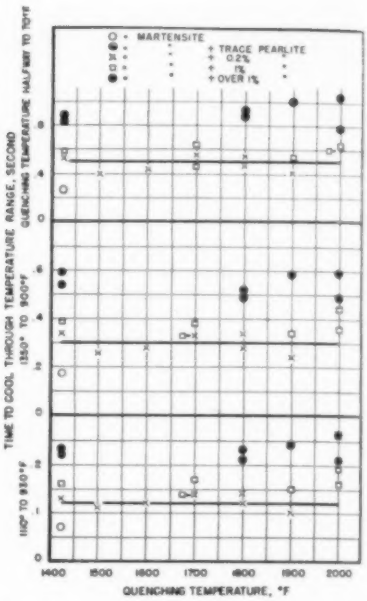

FIGURE 6. *Effect of cooling time on the structure of the 0.50-percent-carbon alloy (B7) quenched from different temperatures.*

The specimens were prepared from a homogenized bar.

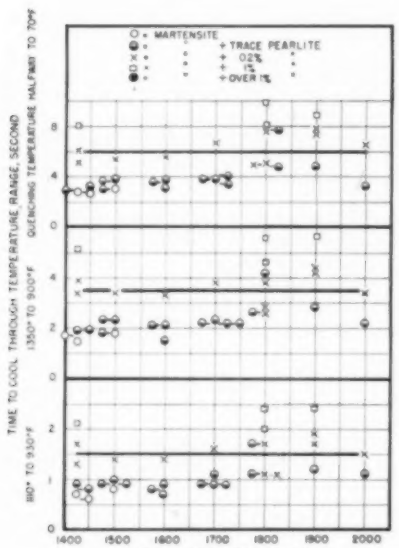

FIGURE 7. *Effect of cooling time on the structure of the 0.54- percent - carbon alloy (B12) quenched from different temperatures.*

The specimens were prepared from a homogenized bar.

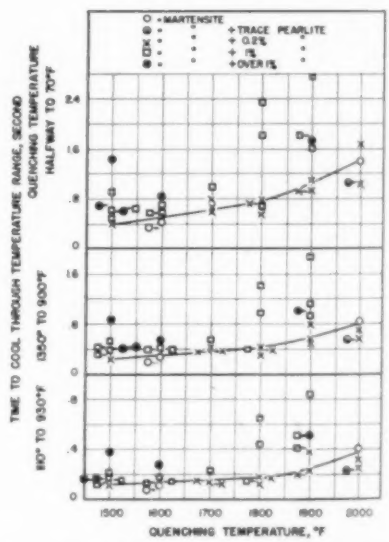

FIGURE 8. *Effect of cooling time on the structure of the 0.47-percent carbon, 0.0020-percent-boron alloy (B5) quenched from different temperatures.*

The specimens were prepared from a homogenized bar.

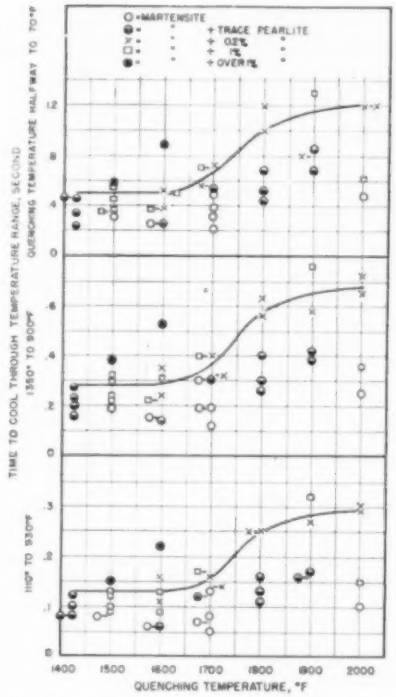

FIGURE 9. *Effect of cooling time on the structure of the 0.70-percent-carbon alloy (B10) quenched from different temperatures.*

The specimens were prepared from a homogenized bar.

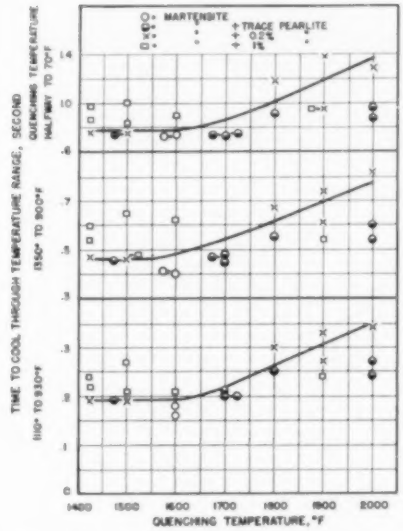

FIGURE 10. *Effect of cooling time on the structure of the 0.74-percent-carbon—0.0028-percent-boron alloy (B5) quenched from different temperatures.*

The specimens were prepared from a homogenized bar.

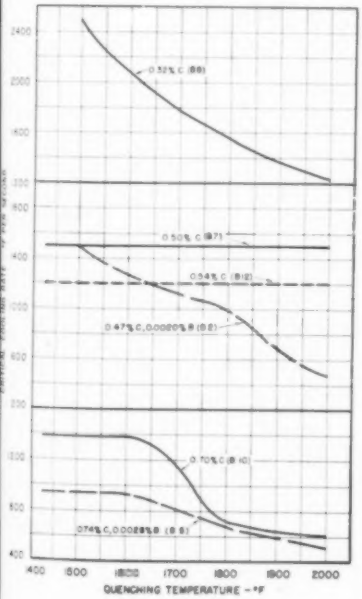

FIGURE 11. *Relation of critical cooling rate to quenching temperature of the iron-carbon alloys.*

The specimens were prepared from homogenized bars. Austenite grain size of the alloys is given in table 2.

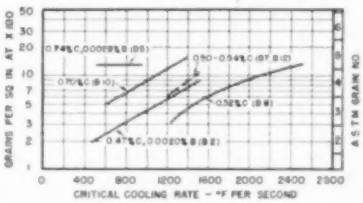
GRAINS PER SQ IN. AT X 100
ASTM GRAIN NO
0.74% C, 0.0020% B (B5)
0.70% C (B10)
0.50-0.54% C (B7, B12)
0.52% C (B9)
0.47% C, 0.0020% B (B2)
0 400 800 1200 1600 2000 2400 2800
CRITICAL COOLING RATE - °F PER SECOND

FIGURE 12.—*Relation of critical cooling rate to austenite grain size of the iron-carbon alloys.*

The specimens were prepared from homogenized bars.

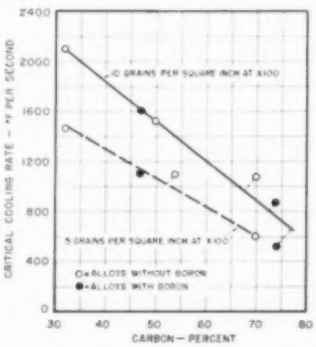
10 GRAINS PER SQUARE INCH AT X100
5 GRAINS PER SQUARE INCH AT X100
○=ALLOYS WITHOUT BORON
●=ALLOYS WITH BORON
CRITICAL COOLING RATE - °F PER SECOND
30 40 50 60 70 80
CARBON - PERCENT

FIGURE 13. *Relation of critical cooling rate to carbon content of the iron-carbon alloys.*

The specimens were prepared from homogenized bars.

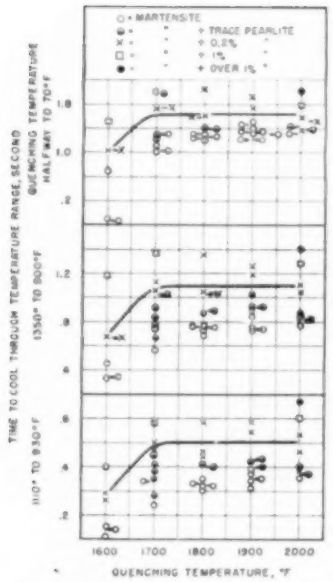

FIGURE 14. *Effect of cooling time on the structure of the 0.32-percent-carbon—0.0021-percent-boron alloy (B6) quenched from different temperatures.*

The specimens were prepared from the ingot.

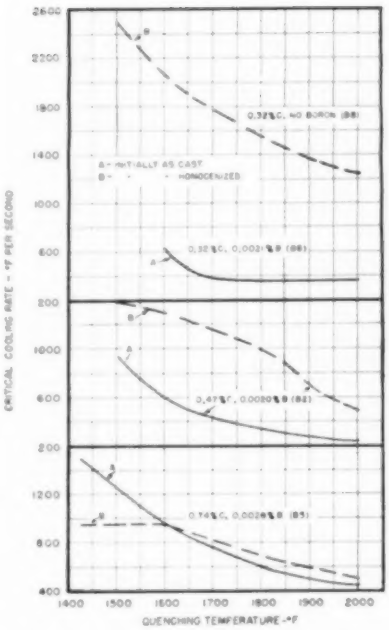
CRITICAL COOLING RATE - °F PER SECOND
A = INITIALLY AS CAST
B = " " HOMOGENIZED
0.32%C, NO BORON (B8)
0.32%C, 0.0021%B (B6)
0.67%C, 0.0030%B (B4)
0.74%C, 0.0026%B (B5)
1400 1500 1600 1700 1800 1900 2000
QUENCHING TEMPERATURE, °F

FIGURE 15. *Relation of critical cooling rate to quenching temperature of some of the iron-carbon alloys.*

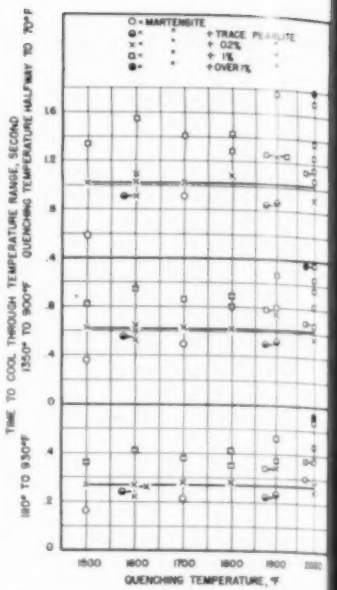

FIGURE 16. *Effect of cooling time on the structure of the 0.42-percent-carbon—0.67-percent-manganese alloy (B13) quenched from different temperatures.*

The specimens were prepared from a homogenized bar.

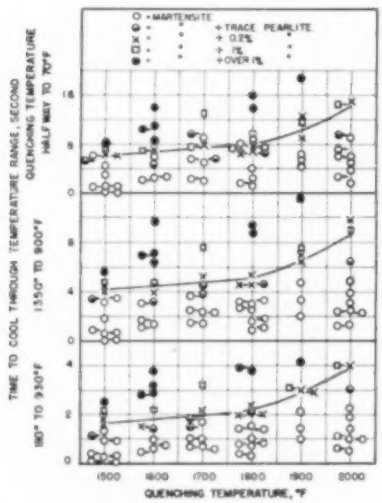

FIGURE 17. *Effect of cooling time on the structure of the 0.41-percent-carbon—0.64-percent-manganese—0.0024-percent-boron alloy (B14) quenched from different temperatures.*

The specimens were prepared from a homogenized bar.

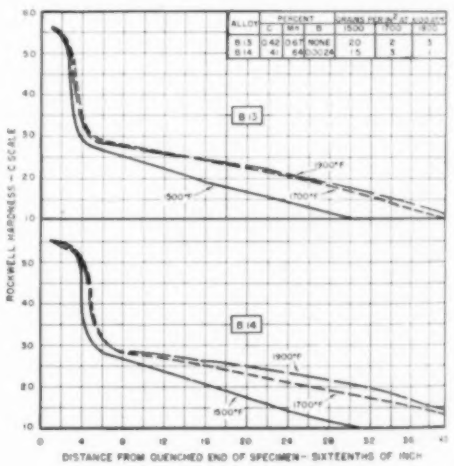

FIGURE 18. *Hardenability curves of the iron-carbon-manganese alloys.*

The specimens were normalized at 1,650° F before end-quenching from temperature as indicated.

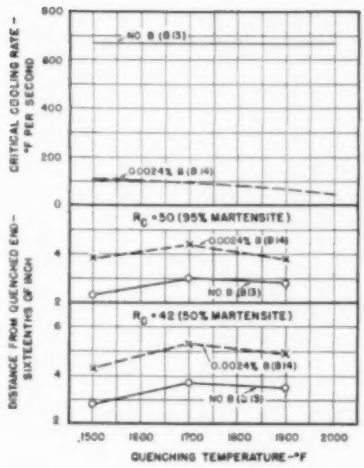
CRITICAL COOLING RATE – °F PER SECOND
NO. 8 (B13)
0.0024% B (B14)
R_Q = 50 (95% MARTENSITE)
R_Q = 42 (50% MARTENSITE)
DISTANCE FROM QUENCHED END – SIXTEENTHS OF INCH
QUENCHING TEMPERATURE – °F

FIGURE 19. *Relation of quenching temperature to the hardenability of the iron-carbon-manganese alloys.*

The specimens were prepared from homogenized bars. Austenite grain size of the specimens used for determining the critical cooling rate is given in table 2 and for the end-quenched bars in figure 18.

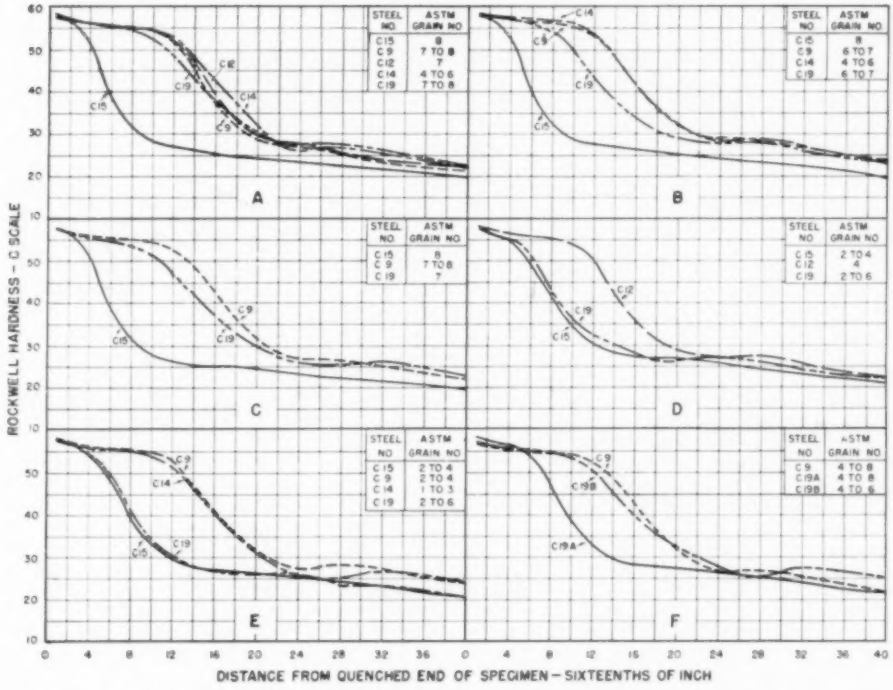

FIGURE 20. *Effect of prior history on the hardenability as determined in the end-quench test of some commercial steels containing 0.43 percent of carbon and 1.6 percent of manganese.*

Steel C15 without boron; C9, 0.0003 percent of B (grainal No. 79); C12, 0.0022 percent of B (ferroboron); C14, 0.0036 percent of B (ferroboron); C19, 0.0091 percent of B (grainal No. 1). All specimens were held for 45 min in the furnace at temperature just prior to end-quenching except as indicated. A, Specimens normalized at 1,650° F before end-quenching from 1,550° F; B, specimens normalized at 1,900° F before end-quenching from 1,550° F; C, specimens quenched from 1,900° F in water before end-quenching from 1,550° F; D, specimens normalized at 1,650° F reheated to 1,900° F, then cooled to 1,550° F and held for 30 min before end-quenching; E, specimens normalized at 1,650° F, reheated to 1,900° F, then cooled to 1,425° F and held for 30 min before end-quenching; F, specimens normalized at 1,650° F, reheated to 1,900° F, then cooled to 1,425° F and held for 30 min then quenched in water. The specimens were then treated as follows: Specimens C19 A and C9 reheated to 1,550° F and end-quenched; specimen C19 B reheated to 1,750° F and end-quenched.

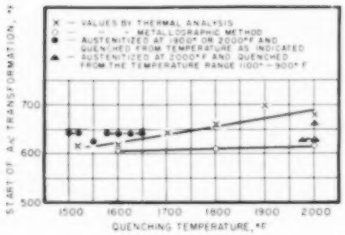

FIGURE 21. *Effect of quenching temperature on the temperature of the start of the transformation of austenite to martensite in a commercial steel containing 0.43 percent of carbon, 1.6 percent of manganese, and 0.0036 percent of boron (C14).*

The average size of the austenite grains ranged from about American Society for Testing Materials number 5 to 2 with change in temperature from 1,550° to 2,000° F.

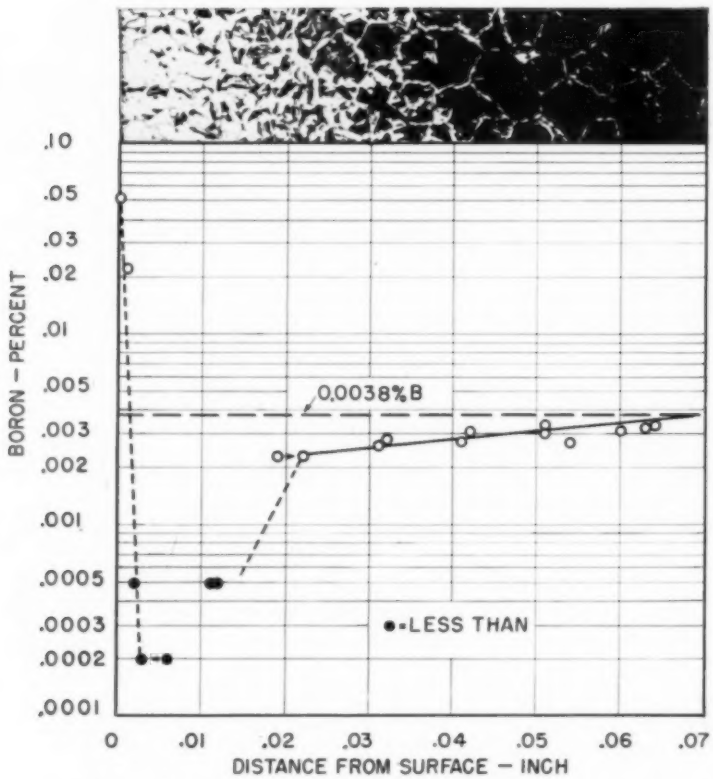

FIGURE 22. *Distribution of boron in a decarburized layer of a commercial boron-treated steel (C14).*

The specimen was decarburized by heating in a furnace (reducing atmosphere) at 1,900° F for 8 hr and then cooling in mica. The left edge of the photomicrograph corresponds to the original surface of the specimen, and the characteristic structure (not decarburized) is shown at the right, etched with 1 percent-nital ×100 (reduced approximately one-half in reduction). Determination for boron by spectrographic analysis was made on the heat-treated specimen at the surface and at various levels below this surface; the successive levels were obtained by progressive grinding. The nominal boron content of steel C14 was 0.0038 percent (heavy horizontal line) as determined spectrographically.

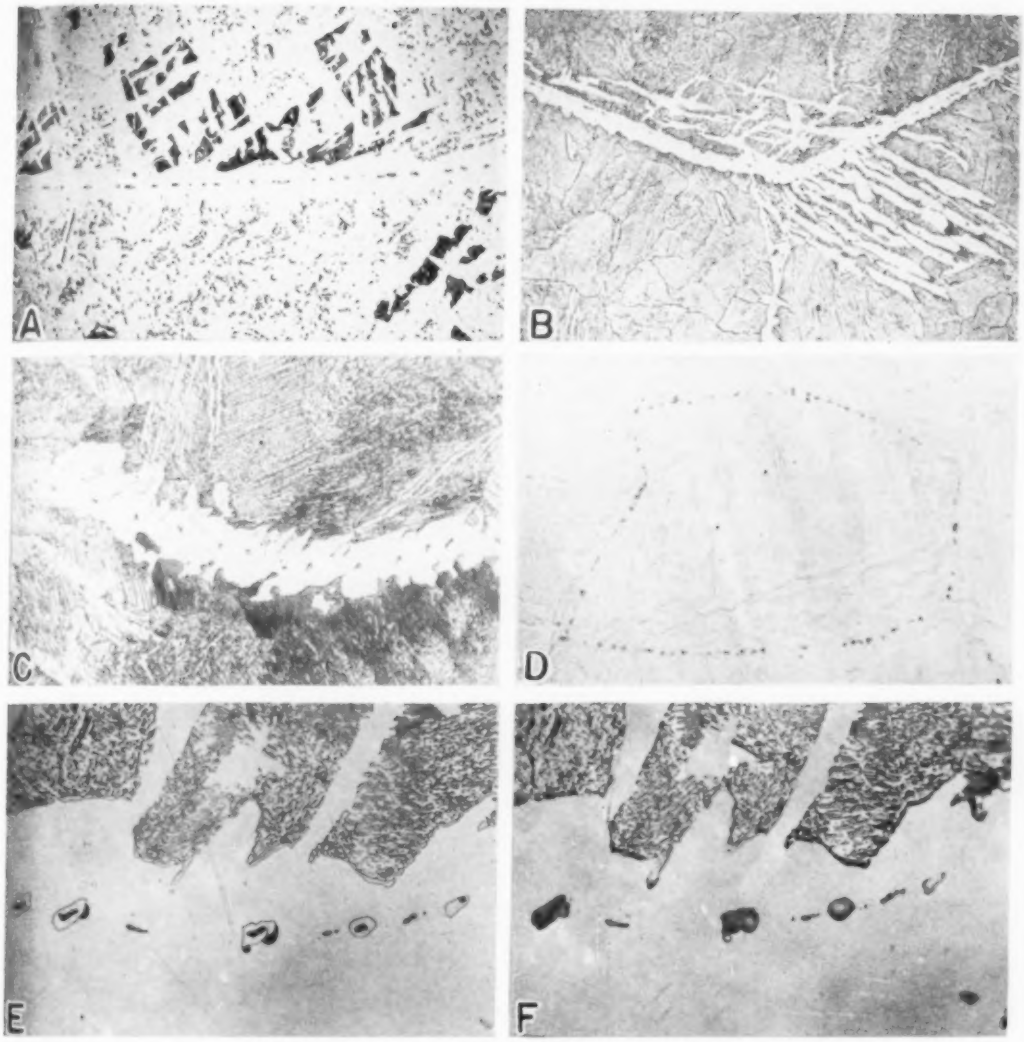

FIGURE 23. *Typical structures of boron-treated alloys as cast or as homogenized.*

A, Alloy (B6) containing 0.32 percent of carbon and 0.0021 percent of boron as cast. Ferrite (white) located in primary austenite grain boundaries contains spheroidized carbides; some spheroidization of carbides occurred during the cooling of the ingot, etched with 4-percent picral, ×100. B, alloy (B2) containing .C percent of carbon and 0.0020 percent of boron as cast, etched with 4-percent picral, ×100. C, alloy (B14) containing 0.41 percent of carbon, 0.64 percent of manganese, 0.0024 percent of boron as homogenized, etched with 1-percent nital, ×500. D, alloy (B2) as cast, unetched, ×100. E, alloy (B2) as cast, etched with 4-percent picral, ×500. F, same area as E, etched electrolytically with 10-percent sodium cyanide in water, ×500.

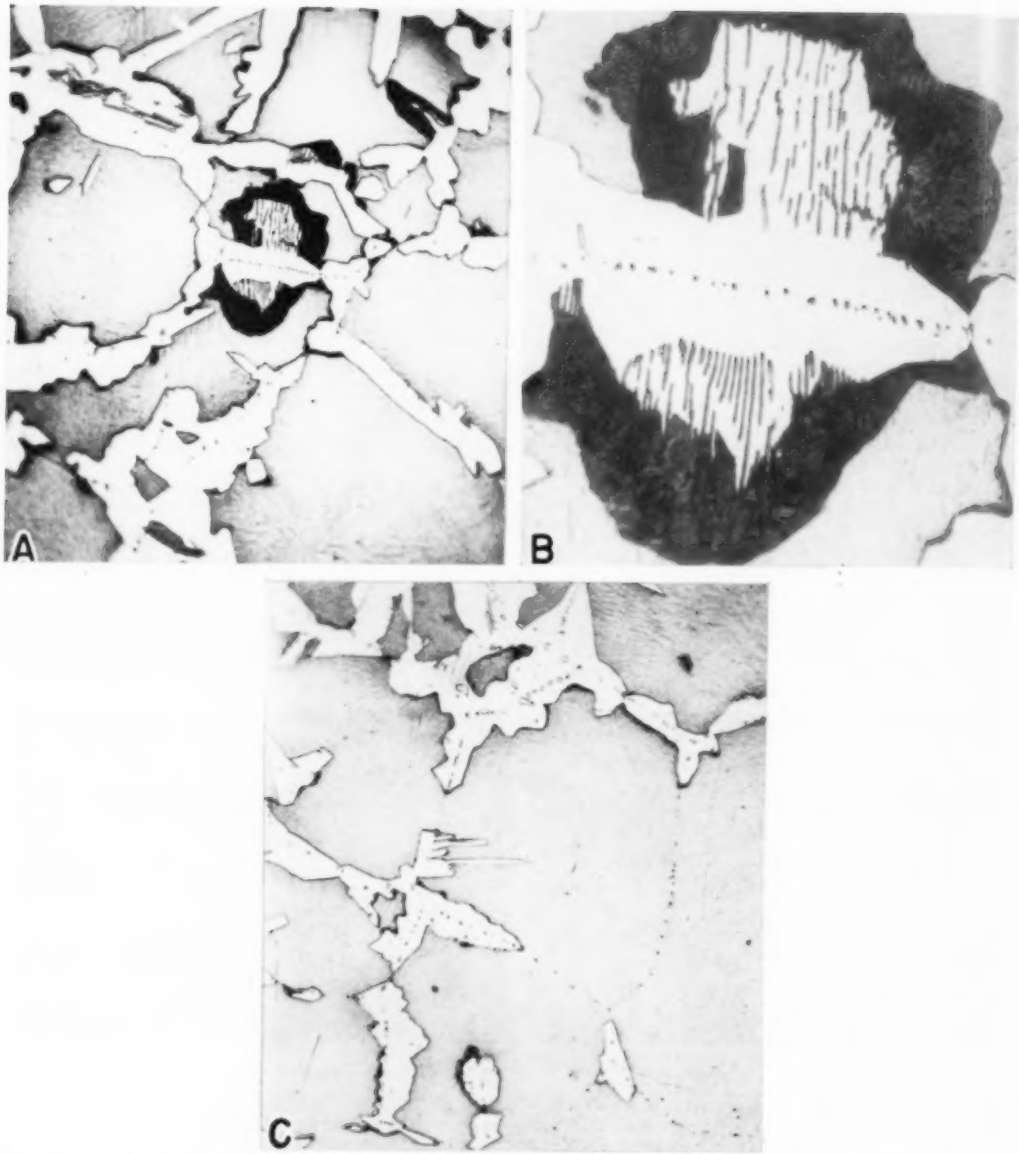

FIGURE 24. *Structure produced in a quenched specimen of the 0.47 percent carbon—0.0020-percent boron alloy (B2).*

A small specimen, initially as cast, was heated to 1,900° F for 3 min and then cooled in a lead bath at 1,300° F for 1 min., followed by quenching in a solution of sodium hydroxide in water at room temperature. Etched with 4-percent picral. A, ferrite network (light) containing some spheroid and elongated carbide particles, martensite (gray), coarse (laminated) and fine (dark) pearlite, ×500; B, pearlite area (shown near center of photomicrograph A) with spheroidized carbide particles extending nearly linearly across this area, ×2,000; C, partial network of ferrite containing carbide particles, martensitic matrix with a boron constituent (relatively fine and dark do), ×500. Note the continuity in the alinement of the carbide and boron containing particles.

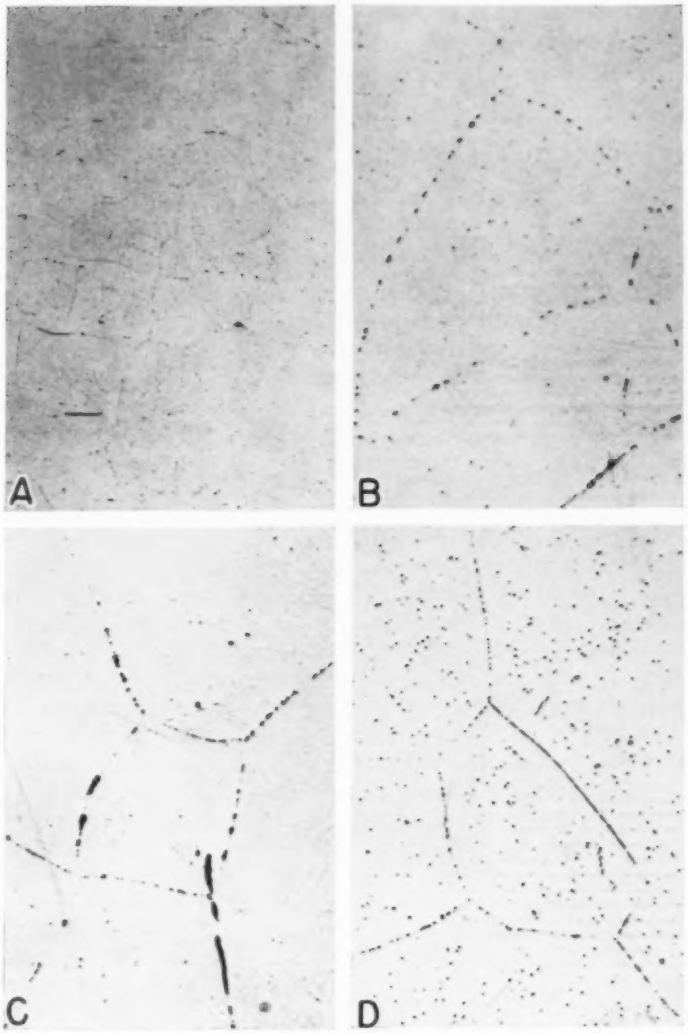

FIGURE 25. *Boron constituent in a commercial steel (C14).*

Etched with 4-percent picral. A, small specimen heated to 2,000° F for 20 min and then cooled in a lead bath at 1,200° F for 2 min, followed by quenching in water at room temperature. The boron constituent (dark etching dots) is located principally in the parent austenite grain boundaries, ×100; B, same specimen as A, ×500; C, small specimen heated to 2,000° F for 20 min and then quenched in iced sodium hydroxide water-solution, ×500; D, same specimen as C. Note the boron constituent also within the grains, ×500.

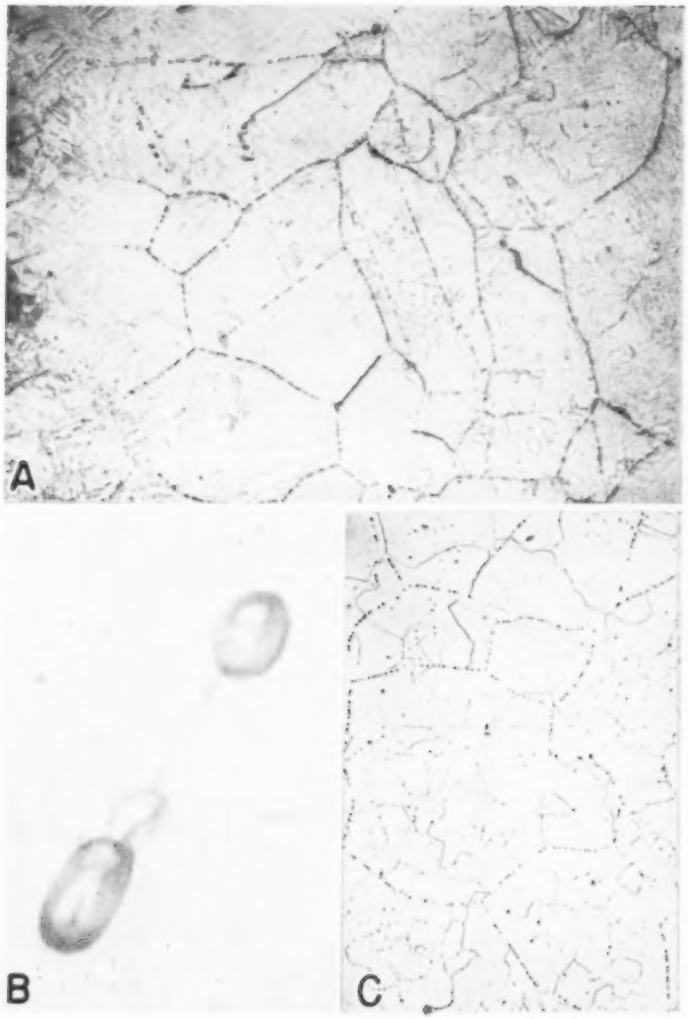

FIGURE 26. *Boron constituent in at high-purity iron-boron alloy (B4).*

Etched with 4-percent picral. A, small specimen, initially as cast, heated to 2,000° F for 3 min, and then cooled in a lead bath at 1,700° F for 5 min follow by quenching in sodium hydroxide solution at room temperature. The left edge of the photomicrograph corresponds to the original surface of the specimen. Note the boron constituent (dark etching dots) located in the parent grain boundaries and in parallel planes within some of the grains; it does not extend to the original surface of the specimen, ×100; B, same specimen as A, ×4,000; C, same specimen as A after reheating in a lead bath at 1,650° F for 5 min and then quenched in sodium hydroxide solution, ×100.

WASHINGTON, July 7, 1948.

U. S. Department of Commerce
National Bureau of Standards

Research Paper RP1939
Volume 41, December 1948

Part of the Journal of Research of the National Bureau of Standards

Absorption of Radio Waves Reflected at Vertical Incidence as a Function of the Sun's Zenith Angle

By Eloise W. Taylor

The diurnal variation of ionospheric absorption is related to the sun's zenith angle. The absorption values for this study were obtained from the continuous automatic field-intensity recordings made at the Central Radio Propagation Laboratory on two frequencies. Because of proximity of the receiving station to the transmitting station, reflections are obtained at nearly normal incidence. An analysis of data covering a period of 3 years indicates that little error is introduced by assuming a linear dependence of absorption upon the cosine of the sun's zenith angle.

Maximum ionospheric absorption of radio waves per unit length of virtual path occurs at that height where the product of the electron density and the frequency of collisions with gas molecules is a maximum. This may be shown to be the lower part of the ionosphere for certain radio frequencies. Here the ionization is produced mainly by ultraviolet radiation from the sun. Various theories of the formation of the E-layer indicate that the absorption should be proportional to some power of cos X, where X is the sun's zenith angle.

The effect of this absorption is to diminish the field intensity of the reflected wave relative to what it would be in absence of absorption. Thus, if E_0 is the intensity of the wave without loss of energy through absorption, and E is the intensity of the wave as actually received, then

$$E=E_0 10^{-A}, \tag{1}$$

where A is the index of absorption.

The purpose of this report is to express the diurnal variation of this so-called nondeviative absorption, the absorption without appreciable refraction, as

$$A=A_0 \cos^n \mathrm{X}, \tag{2}$$

in which X is the zenith angle of the sun and A_0 is the subsolar absorption on the frequency investigated.

In 1944 the Central Radio Propagation Laboratory began a program of recording continuous emissions at vertical incidence. For this purpose four frequencies, namely, 2,061, 4,272, 5,892, and 6,992 kc, were emitted from the radio-transmitting station at Beltsville, Md., and received at the laboratory at Sterling, Va. The base-line distance, about 60 km, is sufficiently short that the reflection can be considered to be at vertical incidence.

The recordings for 3 years, from March 1945 through February 1948, of the 2,061- and 4,272-kc frequencies were analyzed, and the results are presented in this paper. The two higher frequencies were above or near the critical frequency of the $F2$-layer for a considerable part of the time and have, therefore, been excluded from this study.

During the night when the absorption is negligible, the field intensity was assumed to be diminished only by the inverse distance attenuation. This field intensity is referred to as the unabsorbed field intensity. The absorption for any time can be found from the logarithm of the ratio of the received field intensity at that time to the unabsorbed field intensity. The recorded values are in logarithms of microvolts input to the receiver, thus the absorption for any value of cos X is the difference between unabsorbed field intensity and the field intensity received at the time for which that value of cos X obtains.

The median values of received field intensity in logarithms of microvolts input to receiver for each hour of the day were determined from the recordings. These data were grouped by seasons; summer—May, June, July, August; equinox—March, April, September, October; winter—

811266—49—3

TABLE 1. *Average values of absorption index on 2061-kc frequency at vertical incidence corresponding to the values of the cosine of the sun's zenith angle at the middle of the hour, calculated to the nearest 0.05*

The values in columns A are the average values of the absorption index and the values in columns N are the number of hours used to determine the averages

cos X	Apr., Sept., Oct., 1945		May, June, July, Aug., 1945		Nov., Dec., 1945; Jan., Feb., 1946		Mar., Apr., Sept., Oct., 1946		May, June, July, Aug., 1946		Nov., Dec., 1946; Jan., Feb., 1947		Mar., Apr., Sept., Oct., 1947		May, June, July, Aug., 1947		Nov., Dec., 1947 Jan., Feb., 1948	
	A	N	A	N	A	N	A	N	A	N	A	N	A	N	A	N	A	N
0.10	0.44	10	----	---	0.72	11	1.27	21	0.55	17	0.85	17	0.97	18	0.79	10	1.05	31
.15	.50	21	0.34	4	.72	36	0.59	22	.75	29	.84	49	.75	36	.64	42	1.03	78
.20	.59	38	.35	19	.79	73	.63	50	.51	43	.81	88	.76	56	.61	51	0.93	52
.25	.50	34	.46	40	.81	68	1.02	55	.73	40	1.02	64	.85	75	.80	38	1.00	67
.30	.58	41	.47	92	.95	85	1.11	55	.70	94	1.13	79	1.11	58	.82	85	1.23	112
.35	.55	53	.55	66	1.03	88	0.82	75	.90	62	1.23	93	1.09	83	.98	59	1.23	63
.40	.65	49	.56	35	1.14	123	.84	62	.77	40	1.44	123	1.11	61	1.02	37	1.39	134
.45	.80	53	.69	60	1.22	100	1.52	71	1.11	51	1.54	124	1.35	74	1.12	48	1.49	163
.50	.81	57	.73	94	1.32	129	1.17	79	1.06	94	1.60	152	1.43	77	1.31	80	1.52	130
.55	.93	56	.81	70	1.47	88	1.39	80	1.18	70	1.63	95	1.57	84	1.42	65	1.52	104
.60	1.05	73	.79	38	1.48	42	1.62	93	1.40	39	1.87	46	1.70	80	1.57	38	1.53	33
.65	1.12	90	.96	107	1.71	19	1.52	108	1.31	107	1.78	17	1.78	98	1.63	117	1.61	26
.70	1.20	75	1.12	88	----	---	1.67	101	1.54	83	----	---	1.79	96	1.81	54	----	---
.75	1.27	76	1.10	57	----	---	1.73	110	1.68	53	----	---	1.83	101	1.88	46	----	---
.80	1.24	73	1.24	146	----	---	1.81	102	1.64	134	----	---	1.92	90	1.93	136	----	---
.85	1.37	68	1.36	117	----	---	1.83	69	1.76	97	----	---	2.04	52	1.98	82	----	---
.90	1.54	24	1.44	226	----	---	1.93	26	1.96	213	----	---	2.06	25	2.01	183	----	---
.95	----	--	1.54	142	----	---	----	---	1.98	144	----	---	----	---	2.03	144	----	---

TABLE 2. *Average values of absorption index on 4,272 kc frequency at vertical incidence corresponding to the values of the cosine of the sun's zenith angle at the middle of the hour, calculated to the nearest 0.05*

The values in column A are the average values of the absorption index and the values in columns N are the number of hours used to determine the averages

cos X	Mar., Apr., Sept., Oct., 1945		May, June, July, Aug., 1945		Nov., Dec., 1945 Jan., Feb., 1946		Mar., Apr., Sept., Oct., 1946		May, June, July, Aug., 1946		Nov., Dec., 1946 Jan., Feb., 1947		Mar., Apr., Sept., Oct., 1947		May, June, July, Aug., 1947		Nov., Dec., 1947 Jan., Feb., 1948	
	A	N	A	N	A	N	A	N	A	N	A	N	A	N	A	N	A	N
0.10	0.23	11	0.13	22	0.13	41	0.32	24	-------	21	0.12	18	0.25	30	0.20	19	0.11	39
.15	.23	26	.21	48	.22	62	.17	46	0.27	41	.17	61	.22	45	.22	61	.16	62
.20	.22	60	.27	47	.30	84	.20	66	.29	44	.23	88	.25	61	.34	33	.22	83
.25	.22	60	.40	35	.30	63	.35	78	.42	28	.26	66	.22	69	.41	35	.24	69
.30	.35	30	.42	81	.34	84	.40	39	.51	73	.32	81	.37	58	.40	75	.34	78
.35	.35	62	.42	63	.42	88	.36	73	.57	54	.40	93	.37	73	.41	55	.35	88
.40	.37	59	.54	35	.45	125	.43	58	.51	24	.49	121	.44	59	.55	34	.50	122
.45	.45	72	.60	55	.55	164	.61	71	.68	40	.56	153	.50	89	.57	42	.59	157
.50	.53	76	.65	81	.60	128	.57	77	.71	73	.61	126	.62	77	.61	68	.65	126
.55	.60	81	.75	73	.74	91	.65	69	.73	55	.62	94	.67	90	.65	61	.67	94
.60	.64	85	.81	37	.71	39	.79	84	.83	27	.76	63	.80	89	.80	33	.64	43
.65	.72	99	.84	95	.84	22	.76	100	.79	78	----	---	.92	108	.84	65	.69	25
.70	.77	103	.92	86	----	---	.86	93	.91	67	----	---	.97	97	.93	71	----	---
.75	.81	102	.89	53	----	---	.93	99	1.03	47	----	---	1.10	103	1.15	40	----	---
.80	.91	91	.91	124	----	---	1.01	83	0.97	102	----	---	1.14	96	1.23	91	----	---
.85	1.00	65	.99	106	----	---	1.02	66	1.12	85	----	---	1.42	46	1.38	71	----	---
.90	0.91	25	1.00	211	----	---	1.09	22	1.18	166	----	---	1.47	19	1.50	125	----	---
.95	----	--	1.01	119	----	---	----	---	1.22	101	----	---	----	---	1.67	84	----	---

November, December, January, February. The cosine of the sun's zenith angle was calculated to the nearest five-hundredths for the middle of each hour. From these data the mean value of absorption corresponding to a particular position of the sun was determined. Corrections were made for the presence of the earth's magnetic field and for multiple reflections, so that the results are the average absorption index of the ordinary component of a single ray for each value of cos X for each season.

The values of absorption for the two lower frequencies (2,061 and 4,272 kc) are given in tables 1 and 2. The number of hours used to determine the mean value is also given. During the early morning hours, when the sun's zenith angle is great, the electron density of the *E*-layer is not high enough to reflect the 2,061-kc frequency. This accounts for the scarcity of data for these periods.

In figure 1 the values of the absorption index for the 2,061-kc frequency plotted against cos X are shown. A line was fitted to each set of points by visual adjustment and its slope determined. The

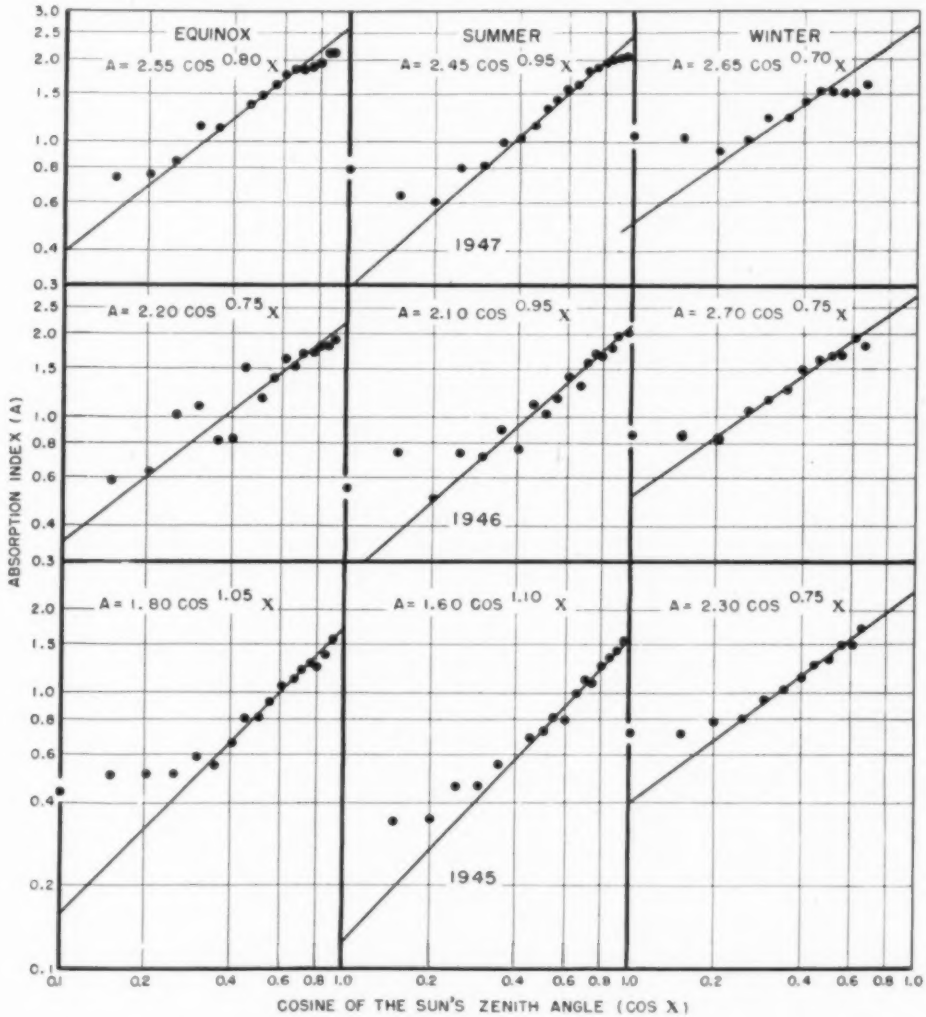

FIGURE 1. *Dependence of absorption at vertical incidence at 2,061 kc on cosine of sun's zenith angle.*

slope is the power of cos X and has a mean value of 0.87 for this frequency. The departures of the plotted points from a straight line for low values of cos X are perhaps due to the scarcity of data when the solar radiation angle is low, indicating inaccuracy of the law for periods near grazing incidence of solar radiation. In 1947 and 1948, the records show ground-wave rather than sky-wave propagation for several hours around noon. The recorded field-intensity values are higher than the sky-wave intensities, and the absorption values are greater than indicated. This was taken into account in fitting the lines to the data.

Figure 2 shows similar plots for the 4,272-kc frequency. The mean value of the slope is 1.07. Difficulty was encountered in analyzing these data, because the layer from which reflections are obtained appears to change during the day. Increases in absorption are attributed to increases in height of reflection. An appreciably greater change of log A with log cos X is noted during the equinox and summer of 1947 when the sunspot numbers were very high.

Table 3 gives the values of A_0, the absorption at cos X=1.00, for each season as obtained from the data for these two frequencies, and the mean sunspot number for the same period. Although the exact rate of change of A_0 with sunspot number

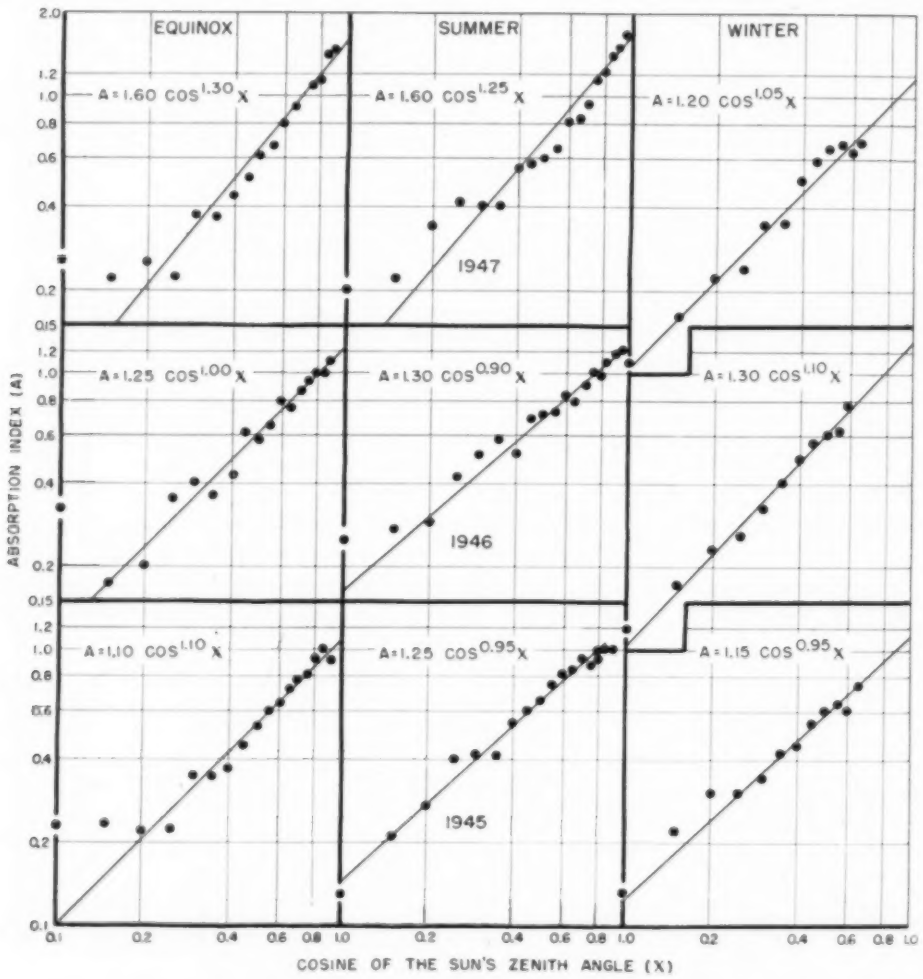

FIGURE 2. *Dependence of absorption at vertical incidence at 4,272 kc on cosine of sun's zenith angle.*

TABLE 3. *Intercepts (A_0) and slopes (n) of absorption equation $A = A_0 \cos^n X$ for 2,061 and 4,272 kc*

Year	Equinox					Summer					Winter				
	Sunspot number	2,061 kc		4,272 kc		Sunspot number	2,061 kc		4,272 kc		Sunspot number	2,061 kc		4,272 kc	
		A_0	n	A_0	n		A_0	n	A_0	n		A_0	n	A_0	n
1945	39	1.80	1.05	1.10	1.10	34	1.60	1.10	1.25	0.95	52	2.30	0.75	1.15	0.95
1946	87	2.20	0.75	1.25	1.00	95	2.10	0.95	1.30	.90	123	2.70	.75	1.30	1.10
1947	159	2.55	.80	1.60	1.30	185	2.45	.95	1.60	1.25	109	2.65	.70	1.20	1.05

has not been determined in this paper, the values show increases in absorption with increased sunspot numbers.

Although the slopes of the A—cos X curves are different for the two frequencies, the variations with season and sunspot number appear to be random. This slope, which represents the changes in absorption from one position of the sun to another, is the power to which cos X is raised in eq 2. The data analyzed in this paper indicate that the law of absorption is different for the two frequencies but constant with season and sunspot number. As the mean values of the slopes for both frequencies are close to unity, the first power of cosine X will express the diurnal variation of absorption sufficiently well for practical purposes.

It is concluded from this analysis that a linear dependence on cosine of the sun's zenith angle is a simple expression that will give the absorption to be expected on any particular frequency at vertical incidence in the daytime. Higher absorption than would be predicted by this law is observed when the sun's zenith angle is close to 90°. The absorption when the solar radiation is incident at other angles increases with increasing solar activity.

WASHINGTON, July 9, 1948.

U. S. Department of Commerce
National Bureau of Standards

Research Paper RP1940
Volume 41, December 1948

Part of the Journal of Research of the National Bureau of Standards

Destruction of Superconductivity by Current[1]

By Russell B. Scott

A series of measurements was made of the return of resistance in superconducting wires when the current was increased up to and beyond the critical value. Wires of pure indium of three different diameters were used, and measurements were made on each wire at four different temperatures. The transition curves for a wire of given diameter were reproducible and were independent of temperature. Measurements on sections of wire 0.6 millimeter long gave substantially the same results as measurements on long wires. The fraction of the normal resistance restored by the critical current varied from 0.77 for a wire 0.36 millimeter in diameter to 0.85 for wires 0.11 millimeter in diameter. The classical formula predicts a value of 0.50. The results are discussed in the light of Landau's theory of the intermediate state, and it is shown that the classical value may be approached for wires of large diameter.

I. Introduction

The reappearance of electrical resistance as the current is increased in a superconductor was discovered by H. Kamerlingh Onnes [1][2] in 1911. Since that time the phenomenon has been studied in several experimental investigations and has been considered from a theoretical point of view. Perhaps the most fruitful theoretical treatment was that given by Silsbee [2] in 1918 in which it was postulated that the magnetic field, associated with the current in a superconductor, is responsible for the restoration of resistance. That is, resistance reappears when the magnetic field reaches a critical value, regardless of whether the field is applied externally or is caused by the current in the conductor. This became known as the Silsbee hypothesis and has been verified in numerous experiments. Silsbee also reported a theoretical treatment suggested by Langevin, which described the resistance as a function of the current in a cylindrical wire as the current is increased up to, and beyond, the critical value. It was predicted that when the current reached the critical value the resistance would rise suddenly to one-half the normal value, and, as the current was further increased, the resistance would rise more slowly, approaching normal resistance asymptotically. The mathematical expression for the resistance was not included in Silsbee's paper, but F. London, in a similar analysis [3], gives the result,

$$R=\frac{R_n}{2}\left[1+\sqrt{1-\left(\frac{I_c}{I}\right)^2}\right],$$

where R is the resistance of the wire carrying the current, I; R_n is the normal resistance measured just above the transition temperature; and I_c is the current that will produce the critical magnetic field at the surface of the wire.

In this analysis the stable state of the conductor, carrying a current a little greater than I_c, is pictured as consisting of an outer shell of normally resistive metal surrounding an inner core of metal in the intermediate state, in which the magnetic field due to the current is exactly critical. Since at critical magnetic field the metal can be either superconducting or normally resistive, it is assumed that the intermediate core consists of layers of superconducting material separated by layers of resistive material, and that the thickness of the layers is a function of the radius such that the current will be distributed so as to maintain the critical value of the magnetic field throughout the core. This calls for a current density inversely proportional to the radius. At the critical value of the current the intermediate core extends to the surface of the wire and, as the current is increased above the critical value, the diameter of the intermediate core shrinks, causing a rise in the measured resistance.

[1] Supported by the Office of Naval Research, Contract NA-onr 12-48.
[2] Figures in brackets indicate the literature references at the end of this paper.

More recent experimental and theoretical investigations (see section VI) suggest that the simple theory just outlined will not account for all the results, because the distribution of normal and superconducting regions is restricted by the surface energy of the boundaries. Thus the pattern of superconducting and normal regions, which satisfies the conditions described above, may be inconsistent with the surface energy requirements.

It is the relation between current and resistance that is the subject of the present investigation. With one exception, the published experimental data give very little information concerning the shape of the transition curve. The exception is a paper by Shubnikov and Alexejevski [4] who found that the critical current caused the sudden reappearance of about 0.8 of the normal resistance in a tin wire immersed in helium II. Because of the marked discrepancy between this result and that predicted by the simple theory, it was considered worth while in the present work to make measurements on wires of different diameters and to conduct the experiments in such a way that the effects of heating by the current could be judged. Measurements were also made on short sections of wire to see if the results obtained on long wires were indicative of a fundamental behavior or were merely averages of more random effects in different parts of the wire.

II. Characteristics of the Specimens

The indium wires used for these experiments were extruded at room temperature through steel dies. A spectrochemical analysis of the indium showed the major impurity to be iron of the order of 0.1 weight percent. The superconducting elements, lead, tin, and thallium were present in amounts less than 0.01 percent. Mercury was not detected. Table 1 is a list of the dimensions of the specimens, their resistances at room temperature and the ratios of resistances just above the transition temperature to the resistance at room temperature. Specimen 1a, a duplicate of 1, was included because this fine wire was so fragile that it was feared there would be deformation when the specimens were mounted. Actually both specimens behaved almost identically, so results are given only for specimen 1.

TABLE 1. *Characteristics of the specimens*

Specimen	Diameter	Length	$R_{300°K}$	$\frac{R_{3.4°K}}{R_{300°K}}$
	mm	*mm*	*w*	
1	0.106	47	0.50	0.0013
1a	.106	47	.50	.0013
2	.286	47	.068	.0012
3	.357	47	.042	.0009
4 (section 1)	.106	0.57	.0059	.0013
4 (section 2)	.106	.63	.0065	.0012

III. Apparatus and Procedure

The cryostat used for this work consisted of a soda-glass Dewar flask for the liquid helium 6-cm inside diameter, 26 cm deep, in a brass jacket immersed in liquid hydrogen. The Pyrex Dewar containing the liquid hydrogen was also enclosed in a copper case, and this was immersed in liquid air. The liquid helium was produced with a separate Simon-type expansion liquefier provided with a transfer siphon so that the liquid helium could be delivered directly into the cryostat during the expansion. The helium produced in a single expansion, 200 to 300 cm, was so well-protected against heat leak in the cryostat that measurements could be taken for 24 hours or more.

The 47-mm specimens 1, 2, and 3 were mounted horizontally on a frame of mica and wood and were supported by the current and potential leads at each end, so that each specimen was in complete contact with the liquid-helium bath. The current and potential leads consisted of short lengths of indium welded to the specimen proper. The current leads, of greater cross section than the specimen, connected to lead (Pb) wires about 40 cm long, which were coiled in the liquid helium bath. The wires leading out of the bath were No. 37 AWG copper. The lengths of superconducting lead interposed between the copper wires and the specimen prevented heat developed in the copper from warming the specimens. The horizontal position of the specimens insured uniformity of temperature along the length.

Specimen 4 was a short length of indium wire provided with several potential taps spaced about 0.6 mm apart. The problem of obtaining close spacing of potential taps without seriously distorting the indium wire was solved by making two grids, each consisting of five separate parallel

platinum wires 0.07 mm in diameter strung on a mica frame and spaced about 1.2 mm apart. The indium wire was laid across one of the grids perpendicular to the platinum wires, and the other grid was placed on top so that the platinum wires made contact with the indium on alternate sides at intervals of about 0.6 mm, thus making 10 potential taps. However, spurious potentials appeared between some of the potential leads when no current was flowing, so not all of the taps were usable. An examination of the specimen under the microscope showed a slight bending of the indium wire, 15 or 20 deg, where the platinum taps made contact, but the sections between the contacts were straight. This specimen was mounted in the cryostat with the indium wire in a vertical position.

The diameters of the indium wires were measured with a traveling microscope, using a bright field. The method was checked by making measurements on other wires of hard metal, which could be measured independently with micrometer calipers. The accuracy of the method was estimated to be about 0.001 mm. The wires were of circular cross section, as evidenced by the fact that different orientations showed the same diameter. Under certain types of lighting, very fine grooves could be seen on the surface of the wires, probably caused by imperfections in the dies. These were estimated to be of the order of 0.001 mm deep.

Current was supplied to the specimens by a 90-v battery through a bank of rheostats arranged for fine adjustment. The specimen currents and potentials were measured with a Wenner potentiometer. For very small potentials the potentiometer setting was left at zero, and measurements were made by means of galvanometer deflections, the sensitivity being of the order of 0.01 μv. Temperatures were determined by measuring the vapor pressure of the bath with a mercury manometer. No correction was made for the hydrostatic pressure of the helium above the specimen. Constant temperature was obtained by manual adjustment of a valve in the helium pumping line, according to the indications of a differential oil-manometer. The handle of the valve was a brass bar about 80 cm long, which permitted fine adjustment. A constantan heating coil at the bottom of the liquid helium bath, dissipating 0.005 to 0.01 w, caused some stirring of the liquid and improved the constancy and uniformity of temperature. The temperature could be kept constant to about 1 or 2×10^{-4} deg for periods of 10 min. Changes in room temperature affecting the differential manometer caused slow drifts of bath temperature amounting to about 0.001 deg/hr. A constant uniform temperature could be achieved very quickly after reducing the pressure over the bath, but after increasing the pressure it was necessary to wait sometimes as long as 30 min before accurate observations could be made. The differential manometer was also used to measure small changes of temperature, such as those required in determining the normal temperature-transition curves of the specimens. All temperatures were computed by means of the vapor-pressure equation for helium I given by Lignac [5]:

$$\log p_{cm} = -4.7921\,T^{-1} + 0.00783\,T + 0.017601\,T^{2} + 2.6730.$$

The earth's field was neutralized with a pair of Helmholtz coils, 46 cm in diameter, surrounding the cryostat with their axis parallel to the earth's field. Another pair of Helmholtz coils of mean diameter 24 cm were used to produce a known uniform vertical field, in the region occupied by the specimens, for experiments on the restoration of resistance by an externally applied field.

The measurements on specimens 1, 2, and 3, and occasionally 1a, consisted of determinations of the normal temperature transitions with small specimen currents, and transitions with increasing and decreasing specimen current at four different constant temperatures below the normal transition temperature. Transitions with increasing and decreasing specimen current were also determined for several sections of specimen 4. When it was found that there was no appreciable difference in the behavior of different sections of specimen 4, only the data on sections 1 and 2 were recorded. Using potential taps about 3 mm apart, measurements of the restoration of resistance by a longitudinal magnetic field were made at three different temperatures.

811266—49——4

IV. Results

The normal transition curves for the three wires of different sizes are shown in figure 1. The specimen current for each wire was chosen to produce a potential at normal resistance of 1 to 2 μv, to give reasonable sensitivity for the resistance measurements. The displacement along the temperature axis of the curves for the larger wires carrying the heavier currents is no doubt caused by the magnetic field produced by the specimen current. The agreement of the three curves at the top of the transition suggests that this is the most reproducible part of the transition curve and should be considered the normal transition temperature. The value thus obtained, 3.409° K, is somewhat higher than the values in the literature for the normal transition temperature of indium. The steep slope of the transition at 2 ma is gratifying, because it shows that neither impurities nor the polycrystalline nature of the specimen were having much effect on the superconducting properties.

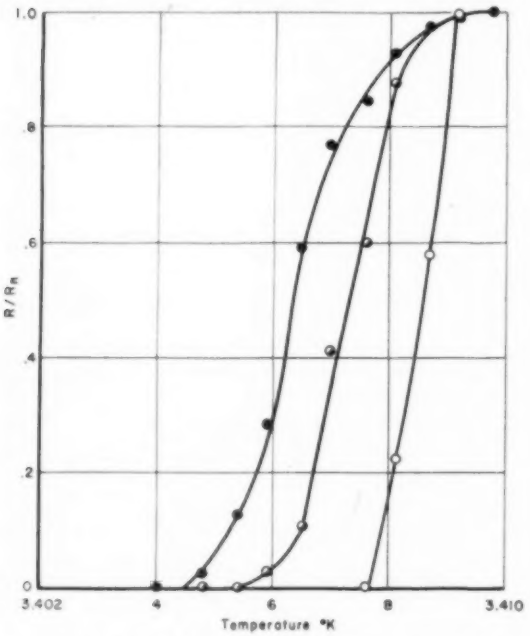

FIGURE 1. *Normal temperature-transitions of specimens 1, 2, and 3, with small measuring current.*

Specimen	Diameter	Measuring current
	mm	*ma*
○	0.106	2
◑	.286	23
●	.357	50

The transitions obtained by increasing the current through specimen 1 at four different constant temperatures are shown in figure 2, where the ratio R/R_n is plotted as a function of specimen current. R is the variable resistance of the specimen, and R_n is the value of R measured just above the normal transition temperature, or measured in an externally applied magnetic field of greater than critical intensity. It is seen that for each

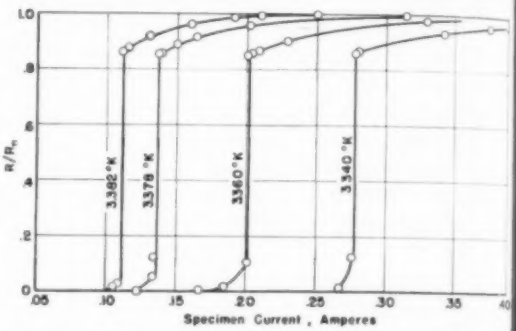

FIGURE 2. *Current-transitions of specimen 1 at four different constant temperatures.*

temperature there is a critical value of current that causes the resistance to rise suddenly to about 85 percent of the normal value. Further increase of current causes a gradual rise of resistance, the values of R/R_n approaching unity at high currents. The small resistance that appears at currents less than critical is probably caused by imperfections in the specimen. The results obtained at different temperatures can be correlated by plotting R/R_n as a function of I/I_c, where I is any value of the specimen current and I_c is the critical current. In such a plot all the data for a given specimen fall on a single curve. This is shown by the upper curve of figure 3, which includes the measurements made on specimen 1 at the highest and lowest temperatures. Data obtained at the lowest temperature on specimens 2 and 3 are also shown. Some of the current transition measurements were not plotted in figure 3 because the crowding of points would have caused confusion. Some of the observed points on specimens 1 and 3 were obtained with decreasing current as indicated by the arrowheads. A

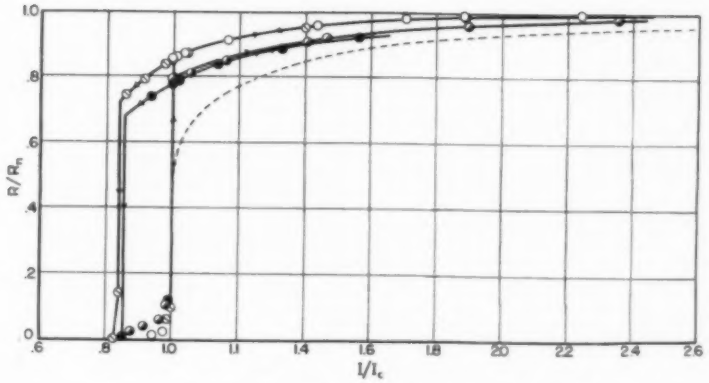

FIGURE 3. *Current-transitions of specimens 1, 2, and 3.*

The upper curve represents data on specimen 1 for the highest and lowest temperatures.

Specimen	Diameter	Temperature
	mm	°*K*
○ 1	0.106	3.3825
⊖ 1	.106	3.3401
◑ 2	.286	3.3410
● 3	.357	3.3403

currents greater than critical, the resistance was the same for increasing and decreasing currents, but when the current was reduced below the critical value there was hysteresis, the resistance remaining large until the current was about 85 percent of the critical value. However, the value of current at which the drop in resistance occurred was by no means as definite as the critical current at which the rise of resistance occurred; and, as will be seen later, some specimens showed no hysteresis. The theoretical curve shown by the dotted line is a plot of the equation given in the introduction.

Table 2 is a summary of the current-transition measurements on specimens 1, 2, and 3. R_c is the value of R at the top of the sudden rise of resistance. The last column gives values of the critical field, $H_c=4I_c/10d$, where I_c is the critical current in amperes and d is the diameter of the specimen in centimeters.

The current-transition data obtained at 3.340° K on the short sections of specimen 4 are shown in figure 4. The solid curve is the same as the upper curve of figure 3, representing the data on the long specimen of equal diameter. The deviations of the observed points from the curve appear to be random and of such magnitude that they

TABLE 2. *Summary of the current-transition data on the 47-mm specimens*

Specimen	Diameter	Temperature	Critical current, I_c	R_c/R_n	Critical field computed from I_c
	mm	°*K*	*ma*		*Oersteds*
1	0.106	3.3825	115.0	0.860	4.34
		3.3778	142.2	.853	5.37
		3.3603	207.4	.848	7.83
		3.3401	283.9	.855	10.71
2	0.286	3.3835	202.1	.794	4.09
		3.3779	353.6	.791	4.95
		3.3613	533.7	.796	7.46
		3.3410	725.2	.799	10.14
3	0.357	3.3837	369.8	.777	4.14
		3.3780	440.8	.774	4.94
		3.3611	668.1	.779	7.49
		3.3403	935.6	.782	10.48

can be attributed to experimental error. The obviously poor accuracy resulted from the very low resistance of the sections measured. For these short sections there was little or no hysteresis when the current was reduced, the resistance dropping almost to zero as the current fell below the critical value.

Figure 5 is a plot of the critical-field data. The solid circles represent measurements of the restoration of the resistance of specimen 4 by a longi-

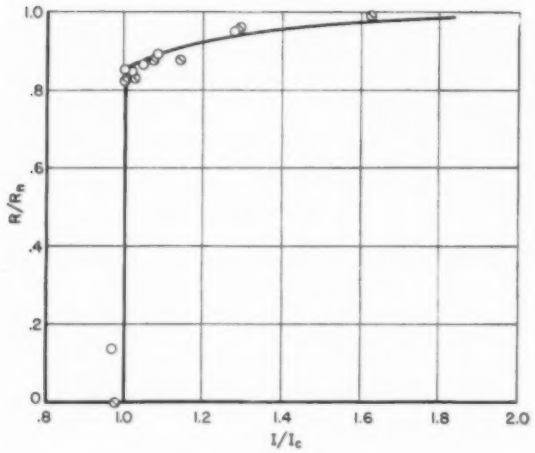

FIGURE 4. *Current-transitions of two sections of specimen 4 at 3.340° K.*

○, Section 1, length 0.63 mm; ⊖, section 2, length 0.57 mm.

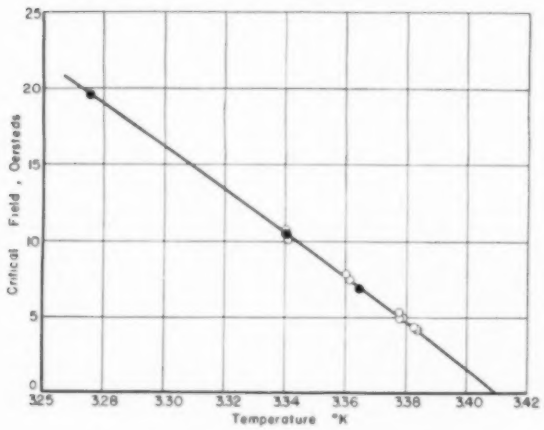

FIGURE 5. *Critical field measurements.*

Values of the critical external longitudinal field for specimen 4 are compared with values computed from critical currents. ●, Field applied externally; ○, field caused by critical current.

tudinal, externally applied magnetic field. The other circles represent the data on specimens 1, 2, and 3 given in table 2, where the critical field is computed from the critical current and the diameter of the wire. The agreement is excellent, the data accurately conforming with the Silsbee hypothesis and furnishing further evidence that the indium specimens behaved as ideal superconductors. Also, the curve through the data passes through the normal-transition temperature, 3.409° K, obtained independently (see fig. 1). As the data were distributed over a temperature range of only 0.14 deg, it was not considered worth while to use an analytical expression to fit the curve. Attempts to measure the critical field by applying it transversely were not very successful, because it was difficult to decide the value of the field at which the resistance reached the normal value. Also, the transition curves obtained were greatly dependent upon the specimen current, as may be seen in figure 6. These measurements were taken

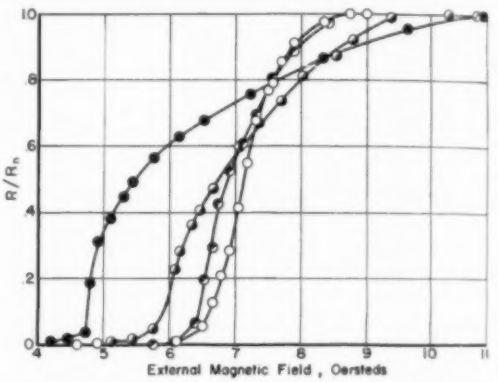

FIGURE 6. *Restoration of resistance by an externally applied transverse field*

○, 1 ma; ◐, 10 ma; ◑, 50 ma; ●, 100 ma.

on an earlier specimen of indium wire 0.106 mm in diameter, 10 cm long, in the shape of a W, mounted horizontally. The curves of figure 6 do not agree with similar measurements by De Haas, Voogd, and Jonker [6]; but, since they do not have a direct bearing on the present investigation, the matter was not pursued further.

V. Effect of Heat Produced by the Specimen Current

It is important to determine whether or not the temperature of the specimen is raised by the current. If there is appreciable heating, the temperature of the specimen may rise above the temperature of the bath when resistance appears. If this happened, part of the sudden rise of resistance could be attributed to a temperature change. The most direct evidence that heating effects are negligible is the fact that the initial rise of the resistance of a given specimen is independent of the critical current. This is seen in figure 2 and table 2. The power dissipated in a given wire varies by a factor of 6, without a significant difference in the

initial rise of resistance. Actually this result might have been predicted because the power dissipated is very small, varying from a minimum of 7 μw cm^{-2} for the largest wire at the highest temperature to a maximum of 270 μw cm^{-2} for the smallest wire at the lowest temperature. The greatest power, 270 μw cm^{-2}, would cause the evolution of vapor bubbles in the liquid helium amounting to only about 2 mm^3 per second per cm^2 of surface at the prevailing pressure of 300 mm Hg; so it is not surprising that the temperature of the wires is practically unaffected.

VI. Discussion

Some conclusions that may be drawn concerning the data just presented are as follows:

1. The indium used accurately obeys the Silsbee hypothesis.

2. The results on the destruction of superconductivity by current are definite and reproducible.

3. For a wire of given size, R/R_n is a function of I/I_c only and is independent of temperature over the range covered by the experiments.

4. If the intermediate state of the wire is assumed to consist of definite regions of normal and superconducting material, the experiments on the short sections of specimen 4 show that the structure is fine grained compared with a length of 0.6 mm.

5. The value of R/R_n at critical current is a rather weak function of the diameter of the wire and is smaller for the larger wires.

6. For the wires used in these experiments the fraction of the normal resistance, restored by current equal to or greater than the critical current, is considerably larger than is predicted by the theory of Langevin.

London [7] has suggested that the cause of the discrepancy between the results of the present experiments and those predicted by the theory lies in the nature of the intermediate state. He [8, 9] describes the intermediate state as consisting of finite regions of normally resistive material interspersed among other regions of superconducting material. The size and shape of these regions are influenced, not only by such considerations as were the basis of the analysis given by Silsbee, but also by the surface energy [10] of the boundaries separating superconducting and normal metal. Landau [11, 12, 13], in extending the theory, made predictions as to the sizes of the regions; and Meshkovsky and Shalnikov [14] have made measurements of the magnetic field distribution in the intermediate state for massive tin hemispheres, finding regions of normal and superconducting metal of the order of 1 mm in thickness in the monocrystalline specimens. Shoenberg [15] discusses similar effects in considering the problem of the restoration of resistance in superconducting cylinders by a transverse magnetic field. As far as is known, there has been no theoretical treatment based on Landau's theory for the restoration of resistance by current.

It is probable that the distribution of normal and superconducting regions required by the simple theory is inconsistent with the surface energy requirements. For example, the extremely thin regions of normal metal near the center of the wire, separating other regions that are superconducting, may be energetically invalid, and a minimum thickness may exist. This would make a big difference in the resistance of a fine wire in the intermediate state, but for very large wires the effect would not be so important. To furnish support for this idea, an attempt was made to find an empirical relation between the wire diameter and the resistance, R_c, at critical current, which would be consistent with the observations and would give the value $R_c/R_n=\frac{1}{2}$ for very large wires. Also it seems reasonable that such a relation should yield the value, $R_c/R_n=1$ for very fine wires. A relation that satisfies these conditions and fits the data very well is

$$\ln\left(\frac{2R_c}{R_n}-1\right)=-\sqrt{d}.$$

A plot of this function is shown in figure 7. The

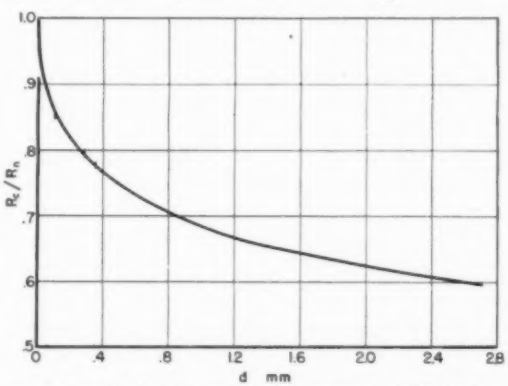

FIGURE 7.—*Graph of the empirical relation* $\ln[(2R_c/R_n)-1]=-\sqrt{d}$, *showing the agreement with observed values of* R_c/R_n.

curve represents the mathematical expression, and the short vertical lines represent the four observations on each of the three specimens 1, 2, and 3, as given in table 2.

It is recognized that the meager data furnish very flimsy support for the empirical relation. The real object in obtaining the equation was to demonstrate that the data are not in disagreement with the idea that the value $R_c/R_n=½$ may be approached with specimens of large diameter. Measurements on much larger wires would be required to establish experimentally a relation that could be accepted with confidence. If the relation given is approximately correct, the wire should have a diameter of 2.6 mm, or about seven times the diameter of the largest wire used in the present experiments, to give a value of 0.6 for R_c/R_n. This would call for specimen currents an order of magnitude greater than those used for specimens 2 and 3. The experimental arrangement used in this investigation did not permit the use of such large currents.

VII. References

[1] H. Kamerlingh Onnes, Commun. Phys. Lab. Univ. Leiden **13,** No. 133a (1913).

[2] Francis B. Silsbee, Bull. B. S. **14,** 301 (1918–19).

[3] F. London, A new conception of superconductivity, Actualites Scientifiques et Industrielles **458,** Exposés de Physique Théorique (Hermann & Cie., Paris, 1937).

[4] L. W. Shubnilov and N. E. Alexejevski, Nature **138,** 804 (1936).

[5] W. H. Keesom, Helium, p. 196 (Elsevier, Amsterdam, 1942).

[6] W. J. De Haas, J. Voogd and J. M. Jonker, Physica **1,** 281 (1933–34).

[7] F. London, Comments made at the Conference on Low Temperature Physics, sponsored by the Office of Naval Research at Yale University (Apr. 5 to 6, 1948).

[8] F. London, Physica **3,** 450 (1936).

[9] F. London, Nature **137,** 991 (1936).

[10] H. London, Proc. Roy. Soc. London **152,** 650 (1935).

[11] L. Landau, Nature **141,** 688 (1938).

[12] L. Landau, Physik. Z. Sowjetunion **11,** 129 (1937).

[13] L. Landau, J. Phys. USSR **7,** 99 (1943).

[14] A. Meshovsky and A. Shalnikov, J. Phys. USSR **11,** 1 (1946).

[15] D. Shoenberg, Size effects in superconductivity, Physical Society Cambridge Conference Report, p. 93 (1947).

WASHINGTON, July 20, 1948.

U. S. Department of Commerce
National Bureau of Standards

Research Paper RP1941
Volume 41, December 1948

Part of the Journal of Research of the National Bureau of Standards

Study of the Modifications of Manganese Dioxide

By Howard F. McMurdie and Esther Golovato

Past work on the modifications of manganese dioxide of interest in dry-cell manufacture is reviewed. New X-ray data, at both room and elevated temperatures, combined with differential heating curves lead to the conclusion that five types of manganese dioxide exist: (1) well-crystallized pyrolusite; (2) gamma manganese dioxide, a poorly crystallized pyrolusite; (3) ramsdellite; (4) cryptomelane, a form containing essential potassium or sodium; and (5) delta manganese dioxide, believed to be a poorly crystallized cryptomelane. The high-temperature X-ray diffraction data indicated the phase changes that cause the heating-curve effects. A new crystal form of manganosic oxide (Mn_3O_4), stable above 1,170° C, was found to be cubic of spinel structure. Fineness determinations by both the nitrogen adsorption and the X-ray line broadening methods were made on selected samples.

I. Introduction

During the years 1940–46 there was increased research on dry cells. This was stimulated by increased demand for the cells as well as new uses for them, combined with certain shortages of raw materials. This work disclosed among other things that manganese dioxide is not a simple compound with constant properties, and that its value as a depolarizer depends on properties other than merely purity. At that time a paper was written at this Bureau [1][1] giving some preliminary findings. Since then, additional work has been done both here and elsewhere [2] on manganese dioxide. The present paper is an attempt to evaluate the work done here and that reported by others. The work has not been confined to dry-cell technology, but was aimed toward a better general understanding of the oxide, its various forms, transformations, and means of identification. This information, it is hoped, will be of interest in mineralogy and crystallography as well as in electrochemistry.

II. Apparatus and Methods

In the present study, X-ray patterns were made on the North American Philips Geiger Counter X-ray Spectrometer by using unfiltered FeK radiation. The patterns were automatically recorded with a counter movement of 1° θ/min. With this equipment a flat specimen is used, and no special techniques were employed to prevent preferred orientation. It is realized that in a few cases this may have resulted in relative intensities that differ from those in other reports. This equipment in its commercial form is not capable of recording the diffraction effects at angles greater than 45° θ; thus, the back reflection lines are missed. Some conclusions are based in part on previous studies with the use of photographic methods.

The X-ray diffraction patterns at elevated temperatures were made in the apparatus described by Van Valkenburg and McMurdie [3]. With this, patterns could be obtained at various elevated temperatures with no intermediate cooling. In many measurements at high temperature, only the section of the pattern corresponding to angles less than 25° θ was scanned, as this was found to be sufficient to identify the phase present.

Differential heating curves on MnO_2 were made on 2-g samples by the method outlined by Speil and others [4]. Al_2O_3 (corundum) was used as an inert body. The temperature of the MnO_2, and the difference in temperature between the MnO_2 and the inert body were automatically recorded as the temperature was raised at a rate of about 8° C/min. The equipment used was described by Newman and Wells [5].

Electronmicrographs were made with the RCA model EMU microscope.

[1] Figures in brackets indicate the literature references at the end of this paper.

III. The Crystal Modifications of MnO_2

Although there is more general agreement on the forms of MnO_2 now than existed several years ago, there still is a certain amount of disagreement on the relations between the various forms. For example, all agree that gamma MnO_2 is a poorly crystallized material, but Cole and his coworkers [2] claim that it is closely related to ramsdellite, whereas McMurdie [1] has considered it related to pyrolusite. As a first step toward settling these questions, it must be agreed as to what lines in the X-ray diffraction pattern are essential to delineate a particular modification.

There is general agreement on the well-crystallized tetragonal form of MnO_2, pyrolusite. This was made artificially by Ferrari [6] and the crystal structure worked out. It was found to be of rutile structure with $a=4.44$ A and $c=2.89$ A. The lines for angles less than 40° θ, which are present in an X-ray pattern, using Fe radiation, are given in table 1. It will be seen that some of the lines reported by Fleischer and Richmond [7] are

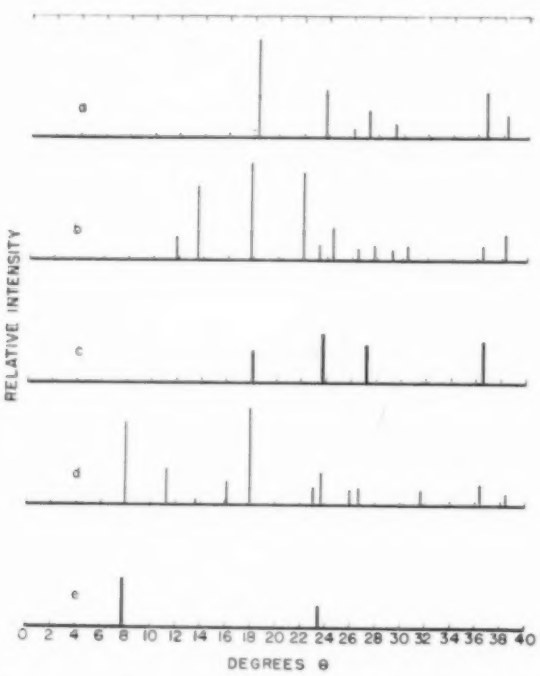

FIGURE 1. *X-ray diffraction patterns of various modifications of* MnO_2.

a, No. 45 pyrolusite; b, No. 42 ramsdellite plus pyrolusite; c, No. C16 gamma MnO_2; d, No. 45 cryptomelane; e, No. C1 delta MnO_2.

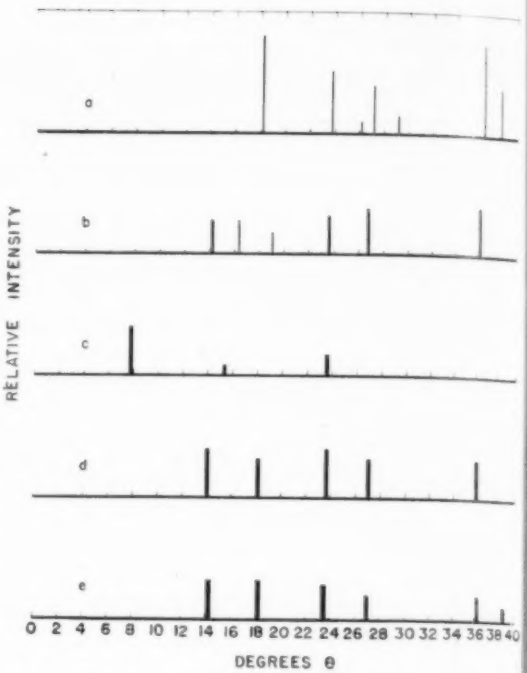

FIGURE 2. *X-ray diffraction patterns of various samples of* MnO_2.

a, No. C15, pyrolusite; b, No. C9 gamma MnO_2 plus cryptomelane; c, No. C11 delta MnO_2, d, No. 46 gamma MnO_2; e, No. C8 gamma MnO_2.

missing. These extra lines are not compatible with the structure given by Ferrari and are not found here in the purest samples. They are doubtless due to impurities. In figure 1, a,[2] the pattern of pyrolusite obtained from a sample of natural ore from Egypt is represented. The 110 and the 220 lines are possibly unduly strong because of preferred orientation in the flat holder. Figure 2, a, shows the pattern obtained from artificial material made by heating $Mn(NO_3)_2$. This pattern is similar to that of the one in figure 1, a, except for the increased broadness of the lines due to smaller crystal size.

The mineral name "polianite" was used for many years to indicate the well-crystallized form, as distinct from massive material called "pyrolusite". It has been shown beyond question [10] by X-ray diffraction that the two are identical and the name polianite is now discarded. It was a

[2] The θ (theta) values indicated on these figures are the angles of diffraction and are related to the d values shown in the tables by the Bragg equation $d=\lambda/2 \sin \theta$, where λ = wavelength of FeK α-radiation (1.936 A).

TABLE 1. *X-ray powder data*

Pyrolusite (No. 45)			Gamma (No. C16)			Ramsdellite [2]	
hkl	d	RI	hkl	d	RI [a]	d	RI
	A			*A*		*A*	
110	3.14	100	110	3.2	60	4.04	Very strong.
101	2.42	80	101	2.4	100	2.54	Strong.
200	2.22	10	..	.....	..	2.43	Medium.
111	2.12	50	111	2.11	70	2.33	Do.
210	1.985	10	..	.....	..	2.13	Medium strong.
211	1.635	80	211	1.63	80	2.05	Very weak.
220	1.570	30	..	.....	..	1.90	Medium.
..	.....	..	..	.....	..	1.65	Medium strong.
..	.....	..	..	.....	..	1.61	Do.

[a] All lines broad.

common belief years ago that the mineral that was without external crystal faces (then called pyrolusite) was superior for dry cells, because it was hydrated. There is at present no evidence of a hydrated form of MnO_2, no other essential elements being present.

Wad is a name that has been used to designate a massive or earthy mixture that is largely MnO_2, but it often contains large percentages of H_2O and BaO. It has no definite mineralogical meaning and actually consists of pyrolusite, psilomelane, cryptomelane, and other minerals [16].

A second well-crystallized form, which was reported first by Fleischer and Richmond [7] is ramsdellite. This is said to be orthorhombic, but the unit cell dimensions have not been given. Cole and coworkers [2] reported a pattern for this material that can be derived from that of Fleischer and Richmond by subtracting the lines of pyrolusite from the latter. Of the various samples of ramsdellite studied here, all have contained pyrolusite in varying degrees. It is believed, therefore, that the best pattern of ramsdellite is that reported by Cole. This is reprinted in table 1. The pattern of the purest ramsdellite obtained here is shown graphically in figure 1, b. Ramsdellite is not known to have been made artificially.

The modification of the greatest interest in battery technology, and about which the most confusion has arisen is gamma (γ)[3] MnO_2. This was first named by Glemser [8] and has been noted by many workers [9, 1]. It is found in natural ores and in artificial products and is generally considered a desirable form for battery use. The patterns reported for it vary, some workers cataloging several varieties [2]. The pattern reported by McMurdie [1] has been criticized as not including a line at a spacing of about 4 A (about 14°θ). Although it is true that in many cases, such as shown in figure 2, b, and figure 2, d, such a line does occur with a pattern that is otherwise mainly that of gamma, in other cases it is much weaker or absent. This would seem to indicate that it is not caused by the same phase as produces the gamma pattern and is not essential to it. The pattern shown in figure 1, c, is of an oxide made by pouring concentrated $Mn(NO_3)_2$ solution dropwise onto a hot plate near 400° C. This, except for the lack of the 4-A line, is approximately what is accepted as a gamma pattern. When this is compared with the pyrolusite pattern, it is seen that it is similar and varies in having broader lines (indicating smaller crystal size) and the absence of the 200, 210, and 220 lines. This would indicate a substance very poorly developed perpendicular to the *c* axis, and of very small crystal size. The cause of the line at 4 A, which occurs in some cases, is not known; it may be related to ramsdellite or groutite ($HMnO_2$) reported by Gruner [11]. Both of these phases give strong lines at about 4 A and may be present in poorly crystallized form with the poorly formed pyrolusite (gamma). The fact that various differences in the gamma MnO_2 pattern occur is not surprising, as the degree of crystallization and percentage of a second phase may vary over wide limits, thus giving a considerable range of patterns.

It is thought very unlikely that the differences, such as noted by Cole and coworkers [2], are caused by real differences in structure; they are probably different in degree of crystallization and of impurities. The pattern, as shown in figure 1, c, is believed to show the minimum number of lines that delineate this modification of MnO_2.

Cryptomelane occurs as a natural mineral, has been prepared (synthetically), and found to be isostructural with hollandite and coronadite [12, 13]. It is the alpha MnO_2 of Du Bois [18]. These minerals have been given the general formula $R\ Mn_8O_{16}$. R is K or Na in cryptomelane, Pb in coronadite, and Ba in hollandite. The name cryptomelane was proposed for the alkali-bearing compound by Richmond and Fleischer [14], it being the commonest of the minerals of this type.

[3] The terms *gamma* and *delta* used here in connection with types of MnO$_2$ are not considered to refer to distinct mineral forms, but rather to denote modifications of technical interest.

The unit cell as determined by Ramsdell [15] was found to be body-centered tetragonal with $a=9.82$ A and $c=2.86$ A. The pattern given in table 2 and shown in figure 1, d, agrees with this cell.

TABLE 2. *X-ray powder data*

Cryptomelane (No. 43)			Cryptomelane (No. 43)		
hkl	d	RI	hkl	d	RI
	A			A	
110	6.92	90	210	2.21	20
200	4.91	50	301	2.16	25
220	3.47	30	141	1.835	20
130	3.11	100	600	1.64	30
400	2.46	20	251	1.54	15
121	2.40	40			

Psilomelane is a name that has been used in connection with manganese dioxide minerals, and various formulae have been proposed for it. The most recent usage restricts psilomelane to a hydrous barium compound ($BaMnMn_8O_{16}(OH)_4$) [16] identical with romanechite. This mineral does not appear to be common among oxides proposed for battery use. Its X-ray pattern, however, is similar to that of cryptomelane and small amounts of psilomelane in mixtures are easily mistaken for cryptomelane.

Delta MnO_2 is a modification, similar to gamma MnO_2 in that it is poorly crystallized and that there is conflicting data on the essential lines. This modification was so designated by McMurdie [1] and is believed to be the same as the material called amorphous by Gruner [12] and manganous manganite by Feitnecht and Marti [17]. Cole and coworkers [2] prepared a sample giving the two lines reported by McMurdie (at 2.41 and 1.42 A) and also a type with more lines, particularly one at 7.13 A. These samples in many cases could be changed to cryptomelane by boiling or heating. With the Geiger-counter equipment in use here at the moment, the patterns of various samples have been repeated. This apparatus does not indicate the lines with as small interplanar spacings as was observed by the film method formerly used, but does give better delineation of lines at greater spacings. The fewest lines found on a sample in the θ range covered are shown in figure 1, e. Another pattern is shown of a similar sample with additional lines in figure 2, c. One sample of delta MnO_2 was found occurring naturally and is shown in figure 3, d. The evidence is that delta

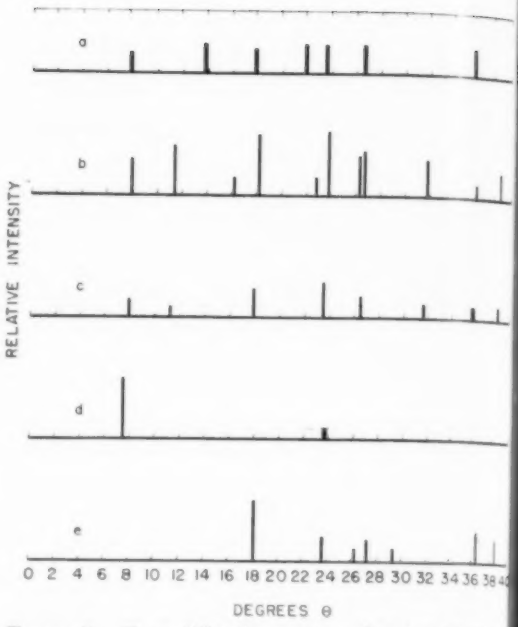

FIGURE 3. *X-ray diffraction patterns of various samples of* MnO_2.

a, No. 34 gamma MnO_2 plus cryptomelane; b, No. C5 cryptomelane; c, No. C9 gamma MnO_2 plus cryptomelane; d, No. 39 delta MnO_2; e, No. 2 pyrolusite.

bears to cryptomelane a similar relation as that of gamma to pyrolusite in being very finely crystalline; and since various degrees of crystallinity can exist, the pattern will vary.

Consideration has been given to the possibility of a hydrated form of MnO_2. Such a compound has not been found. Weiser [20] made MnO_2 samples by various wet methods, and although no X-ray data are given, from samples prepared by similar methods by others, it is known that the samples must have included delta and gamma specimens. These were dried at various temperatures, and he states that no evidence was found that hydrates exist and that the water of the finely divided forms is adsorbed.

IV. Occurrence of the Modifications

Patterns have been made here on samples, both artificial and natural, that have been proposed for or used for battery depolarizers. The principal MnO_2 modification, as determined by X-ray diffraction, and the source of the sample are given in table 3. The method of manufacture and of treatment of some commercial ores is not known

Although it would add to the value of this report if these data were known, it would also be of value to have exact comparative data on the behavior of these ores in cells. In many cases, however, data are available by which ores can be roughly classified. In column 5 of table 3, ratings are given on these for which some information was available. The rating from A to D in descending order of value or capacity is admittedly rough, but is believed to be of some interest. The number assigned to an ore is that used throughout the report.

TABLE 3. *Samples of manganese dioxide*

Sample	Source	Pattern	Percentage of MnO_2	Rating
		Natural samples		
1	New Brunswick	Pyro	72	C
2	Java	do	86	C
3	Mexico	do	81	D
4	Nova Scotia	do	83	C
5	Utah	do	82	D
6	Arizona	do	78	C
7	Mexico	Pyro+crypt	78	D
8	Australia	Crypt	81	B
9	California	Gamma	68	A
10	Morocco	Pyro	91	D
11	Mexico	Crypt	78	C
12	Cuba	Pyro	.....	C
13	Gold Coast	Gamma	86	A
14	Greece	do	62	B
15	Arkansas	Pyro	82	C
16	Mexico	do	61	D
17	Phillipines	do	69	C
18	Virginia	Crypt	73	B
19	Java	Pyro	88	B
20	Papua	Gamma	88	A
21	South America	Pyro	78	C
22	Cuba	do	87	D
23	Morocco	do	87	C
24	Montana	do	83	C
25	Africa	Gamma+crypt	74	A
26	Caucasia	Pyro	86	B
27	California	Gamma	66	A
28	India	Pyro+crypt	84	C
29	Montana	Crypt	.....	B
30	Brazil	Pyro	.....	.....
31	Nevada	do	67	C
32	Wyoming	do	83	C
33	China	do	81	C
34	Human China	Gamma+crypt	.....	A
35	India	Pyro+crypt	83	C
36	Utah	Crypt	69	B
37	Nova Scotia	Pyro	88	C
38	do	do	88	B
39	Canada	Delta	68	B
40	Morocco	Pyro	91	D

TABLE 3. *Samples of manganese dioxide*—Continued

Sample	Source	Pattern	Percentage of MnO_2	Rating
		Natural samples		
41	Lower California	Pyro+crypt	76	C
42	New Mexico	Ram+pyro	.....	.....
43	Tombstone, Ariz	Crypt	>90	.....
44	Virginia	do	75	.....
45	Egypt	Pyro	99	.....
46	Gold Coast	Gamma	.....	A
47	Japan	Pyro	85	B
48	Sugar Stick, Ariz	Crypt	>90	.....
		Artificial samples		
C1	Chemical	Delta	.....	B
C2	Electrolytic	Gamma	.....	A
C3	No. 10 "treated"	do	.....	A
C4	No. 12 "treated"	do	.....	A
C5	No. 11 "treated"	Crypt	.....	B
C6	No. 13 "treated"	Gamma	.....	A
C7	Electrolytic	Gamma+crypt	.....	A
C8	Chemical	Gamma	.....	.....
C9	do	Gamma+crypt	.....	.....
C11	do	Delta	.....	A
C13	do	do	.....	.....
C14	Electrolytic	Gamma	.....	A
C15	Pyro from $Mn(NO_3)_2$.	Pyro	.....	.....
C16	Gamma from $Mn(NO_3)_2$.	Gamma	.....	.....

In this work no attempt has been made to prepare material in various ways, but from the findings reported here and in previous papers certain conclusions can be drawn.

Pyrolusite (well crystallized) occurs commonly in nature and can be prepared artificially by heating Mn $(NO_3)_2$; by hydrolysis of $MnCl_4$ [2], and by heating certain cryptomelane or delta samples [2]. Gamma samples become better crystallized and form pyrolusite on heating [2, 8]. It has been shown by several investigators [2, 7] that ramsdellite changes to pyrolusite on heating near 500° C.

Gamma manganese dioxide (poorly crystallized pyrolusite) occurs to some extent in nature. The well-known Gold Coast ore is largely of this form, and other occurrences are listed in table 3. The gamma manganese dioxide was prepared here by heating a saturated solution of Mn $(NO_3)_2$ quickly and is of common occurrence in electrolytically prepared samples. Cole [2] prepared

gamma chemically by various means but was unable to foretell when gamma and when cryptomelane would result. The patterns of samples C3 and C4, table 3, indicate that the "treatment" used formed gamma from well-crystallized pyrolusite. The treatment was done by a commercial battery company and is not known to us. From discharge data available, it is evident that the reduction of crystal size (and thus increased surface) resulting from the process improved the ore for battery use.

Cryptomelane has been made by Cole [2] and in this laboratory by precipitation of MnO_2 from $KMnO_4$ solution. In some cases, the poorly crystallized delta MnO_2 resulted, and cryptomelane was made from this by heating. Cole [2] found that electrolysis of solutions containing K or Pb gave a material with a cryptomelane pattern. (The pattern of coronadite is similar to that of cryptomelane and may be the form resulting in the case of Pb). Sample C5,[4] with presumably the same treatment as samples C3 and C4, gave a cryptomelane pattern, just as did the untreated material. Cryptomelane, of an extremely fibrous nature, was found to result from autoclaving certain samples of delta and gamma MnO_2 [1]. In nature cryptomelane is very abundant [7].

Delta MnO_2, believed to be poorly crystallized cryptomelane is found rarely in nature, only one such sample being available here (sample 39, fig. 3, d), but it is formed from $KMnO_4$ solution by precipitation with HCl. It is found as a major constituent in many chemically produced oxides.

Ramsdellite is known to occur with certainty only at Lake Valley, N. Mex. Here it is intimately related to the pyrolusite. It is not known to have been made artificially.

V. Particle Size and Shape

Because the action of MnO_2 in dry cells is largely a surface action, the degree of fineness is important. The gamma and delta MnO_2 are finely divided, as shown by the line broadening in the diffraction patterns. This fine crystal size and high surface area are also shown by the electron microscope. Sample 13, figure 4, a, consists of fuzzy clumps of short fibers or plates, which is typical of gamma samples. Figure 4, b shows the fine fraction of C1 (delta). These particles are very thin plates. Sample C4 (fig. 5, a) indicates the fibrous nature of this artificial gamma MnO_2 made from the well-crystallized pyrolusite (sample 12) shown in figure 5, Figure 6, a and b, shows a cryptomelane before and after treatment (samples 11 and C5) showing very well crystallized particles in both cases. Figure 7, a and b, shows the extreme acicular crystals of cryptomelane formed by autoclaving.

Measurement of the specific surface of several samples was made by the nitrogen adsorption method [21].[5] The samples were evacuated at room temperature overnight. Nitrogen gas was adsorbed on the surface at liquid nitrogen temperature (−195° C). The surface areas of the samples were calculated according to the Brunauer, Emmett, and Teller equation [28] and assuming an area of 16.2 A^2 as the area of a nitrogen molecule. The results are given in table 4.

TABLE 4. *Fineness of* MnO_2 *samples by nitrogen adsorption method*

Sample	Surface area	Rating
	m^2/g	
C1	57.6	B
C2	44.1	A
C13	40.2	
C7	35.4	A
C4	18.5	A
13	7.5	A

As a further measure of particle size, the average crystallite size of several samples of gamma and delta oxides were calculated by the method of X-ray line broadening [26, 27]. This method gives the average crystal size rather than the size of particles, which may be made up of many small single crystals. The breadths of the peaks on the recorded pattern are measured at one-half intensity and compared with the width of similar peaks of well-crystallized samples (crystals over 0.1 μ). This increased width is caused by the small crystal size and is used in the calculation as follows:

$$L=\frac{0.89\lambda}{Bc\cos\theta},$$

where

L = average crystallite diameter, A
Θ = Bragg angle
λ = wavelength of X-ray beam
Bc = increased peak width at one-half intensity, radians.

[4] Sample numbers refer to list of samples in table 3.

[5] The specific surface measurement was made by R. F. Blaine of the fine laboratory of this Bureau.

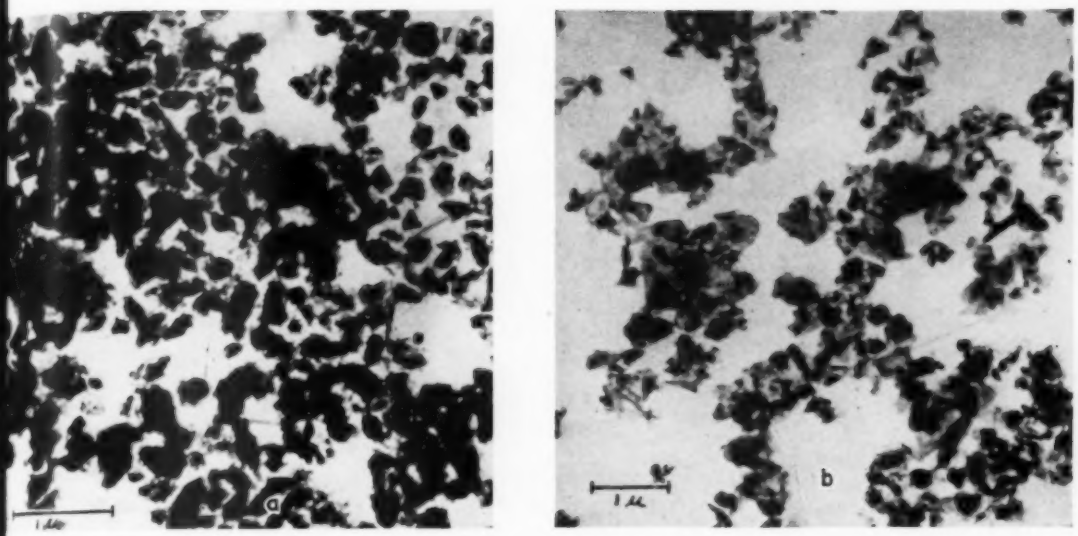

FIGURE 4. *a, Electron micrograph of fine fraction of sample 13 (gamma); b, electron micrograph of sample C1 (delta).*

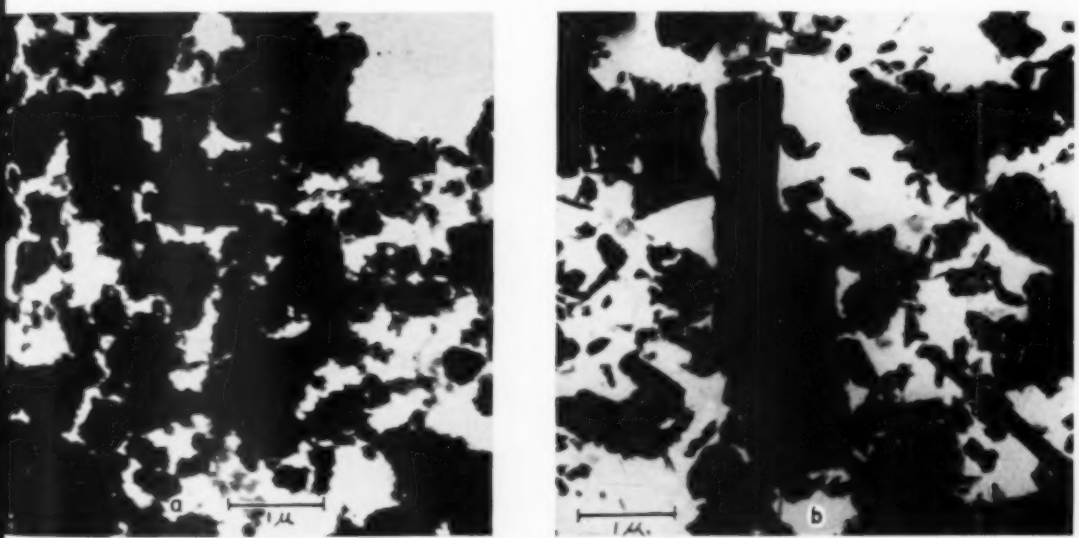

FIGURE 5. *a, Electron micrograph of sample C4 (gamma); b, electron micrograph of sample 12 (pyrolusite).*

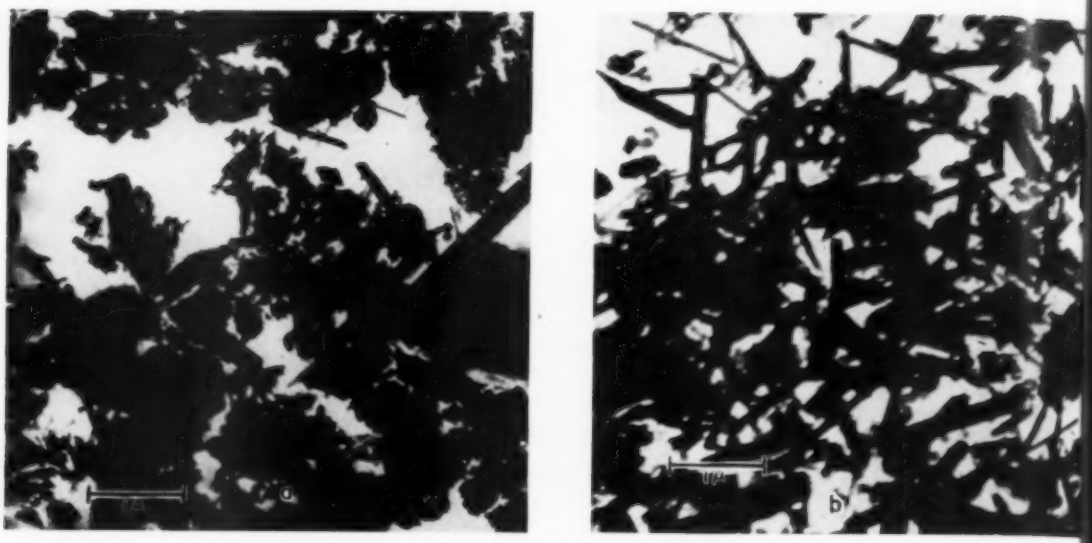

FIGURE 6. *Electron micrographs of a sample of cryptomelane.*

a, Before treatment (sample 11); b, after treatment (sample C5).

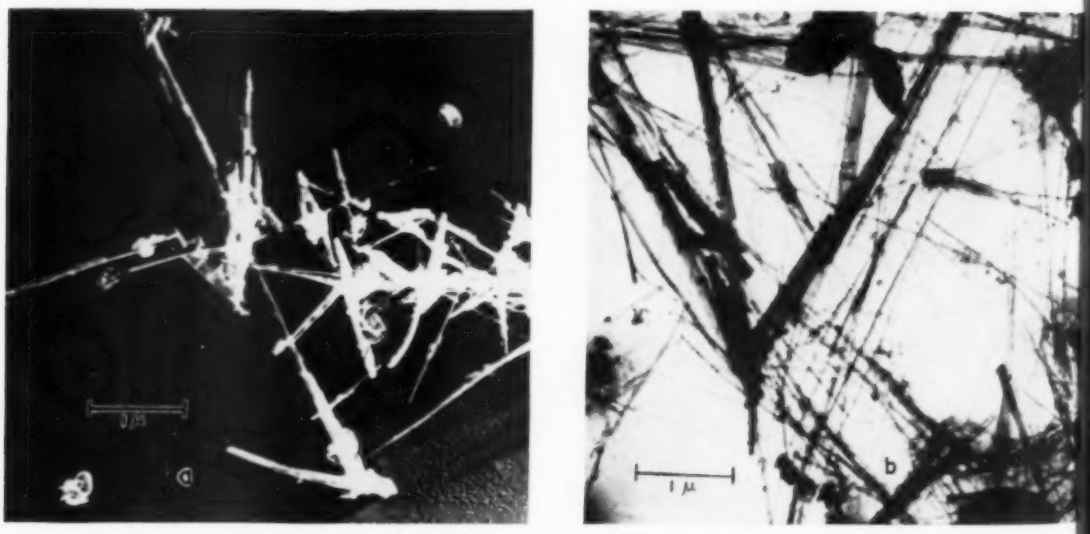

FIGURE 7. *Electron micrograph of cryptomelane formed by autoclave treatment.*

a, Shadowed; b, unshadowed.

The results were as follows:

Sample	Average diameter
	Å
13	207
34	176
C1	117
C2	173
C5	249
C3	220. 5

VI. Heating Curves and High-Temperature X-Ray Diffraction

Differential heating curves have long been used to investigate clays and other inorganic solids [22 to 24]. Such methods indicate the temperature, direction, and intensity of thermal changes that take place when a sample is heated (or cooled) at a constant rate. These changes may be the result of decomposition, reduction, oxidation, inversion, melting, or other change in phase. Any particular compound will undergo certain changes, resulting in peaks on the heating curves that are typical, just as are the lines of a diffraction pattern. Such curves can then be used empirically as a means of identification and analysis; but if the phase change causing the thermal effect can be determined, much more can be learned about the properties and nature of the material. In this study, heating curves of a number of MnO_2 samples were made and with some samples X-ray patterns were made at a series of temperatures, making it possible to determine the phase change involved in the heating curve. This was done with the equipment described above. The patterns, in most cases, were made at 100° C intervals up to about 1,300° C. At each temperature, about 15 min was required to obtain the pattern and 20 to 30 min taken between patterns to obtain the next higher temperature. Thirty-seven heating curves were made; figures 8 and 9 give typical data from different samples of MnO_2, and table 5 shows the phases present at various temperatures on certain samples.

On pyrolusite of high purity, such as sample 45 (fig. 8, b), the heating curve is quite simple. There are endothermic breaks at about 670° C, 950°, and 1,170° C. Sample C15 (fig. 8, a) gave similar results, except that the first break was at a slightly

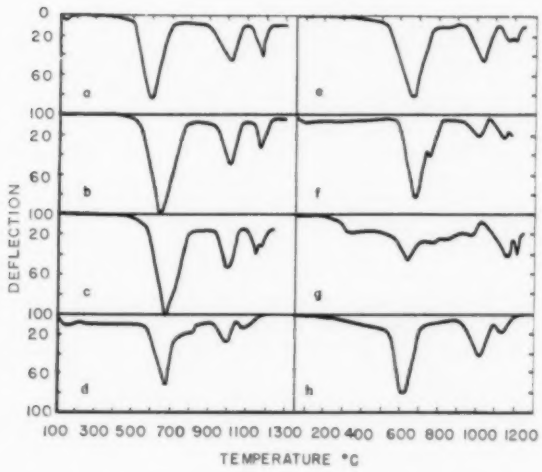

FIGURE 8. *Heating curves of various* MnO_2 *samples.*

a, No. C15 pyrolusite; b, No. 45 pyrolusite; c, No. 40 pyrolusite; d, No. 3 pyrolusite; e, No. 2 pyrolusite; f, No. 26 pyrolusite; g, No. 13 gamma MnO_2; h, No. 46 gamma MnO_2.

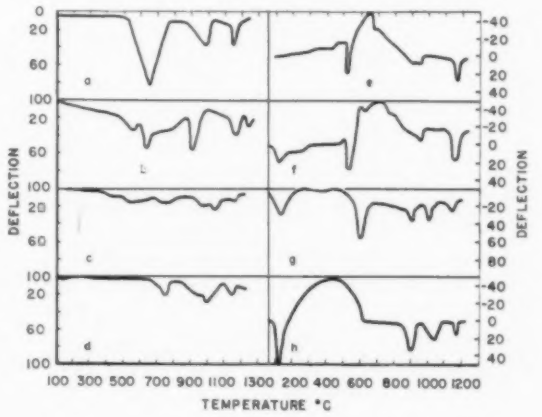

FIGURE 9. *Heating curves of various* MnO_2 *samples.*

a, No. 42 ramsdellite plus pyrolusite; b, No. 43 cryptomelane; c, No. 44 cryptomelane; d, No. 36 cryptomelane; e, No. C14 gamma MnO_2; f, No. C2 gamma MnO_2; g, No. C8 gamma MnO_2; h, No. C13 delta MnO_2.

lower temperature. The X-ray data clearly show that the 600° to 700° C thermal effect is due to loss of oxygen and the formation of bixbyite (Mn_2O_3), and that the break at about 950° C is further loss of oxygen and the formation of hausmannite (Mn_3O_4).

The thermal change at 1,170° C is more complex. It was known from previous studies that even after prolonged heating to 1,300° C, diffraction patterns made at room temperature were of hausmannite,

TABLE 5. *Results of high-temperature X-ray diffraction studies of manganese dioxide*

Temperature	Major phase present for sample—										
	26	C15	42	46	43	48	36	C2	C11	C1	C8
°C											
25	Pyro	Pyro	Ram & Pyro	Gamma	Crypt	Crypt	Crypt	Gamma	Delta	Delta	Gamma.
200	do	do	do	do	do	do	do	do	do	do	do
300	do	do	do	do	do	Crypt	do	do	Delta	do	do
400	do	do	do	do	Crypt	do	do	Gamma	do	Delta	do
500	Pyro	do	Pyro	Pyro	do	do	do	do	do	do	Crypt.
600	do	do	do	do	Crypt	do	do	Bix	do	Crypt	Crypt & Bix.
700	Pyro & Bix.	Bix	Bix	Bix	Crypt & Haus	Crypt & Bix.	Crypt	do	Bix	Crypt & Bix	Do.
800	Haus	do	do	do	Haus	do	Crypt & Haus	do	do	Bix	Do.
900	do	Bix	do	do	do	Bix	Haus	do	do	do	Bix.
1,000	do	do	Haus	Haus	do	do	do	Haus	do	Haus	Haus.
1,100	do	Haus	do	do	do	do	do	do	Haus	do	do
1,200	Spinel	Spinel	Spinel	Spinel	do	do	do	Spinel	do	do	Spinel.
1,300	do	do	do	do	do	do	do	do	do	do	do

therefore no further reduction was to be expected. It was found that if after reaching 1,200° C, the furnace was cooled, an exothermic break took place near 1,100° C with samples of high purity. The X-ray study indicated that at 1,170° C there was a rapid and readily reversible inversion from hausmannite (Mn_3O_4) to a cubic substance with a unit cell of 8.7 A. This indicates that Mn_3O_4 ($MnO.Mn_2O_3$) forms a spinel structure, isostructural with $MgO.Al_2O_3$ above 1,170° C. The spinel structure is one in which there are many substitutions and which occurs under very diverse conditions [25]. Hausmannite structure in itself is definitely tetragonal but is a distorted spinel structure; thus the inversion at 1,170° C is a simple one, occurs quickly, and is reversible and therefore of the α-β quartz inversion type. The data from the pattern made at 1,200° C are given in table 6, along with the room temperature data for bixbyite and hausmannite.

The heating curve for the sample (42 in fig. 9, a) containing the highest percentage of ramsdellite was very similar to that of pyrolusite. There was a section below the first break at 670° C where heat was being absorbed and where the X-ray patterns indicated a change to pyrolusite. This change from ramsdellite to pyrolusite does not appear to occur sharply or to be accompanied by a large energy effect and is not reversible. After the change to pyrolusite, the results were the same as with pure pyrolusite.

Samples of gamma oxides of natural origin such as 46 (fig. 8, h) gave heating curves similar to well-crystallized pyrolusite, except that the first break was slightly lower in temperature. The data in table 5 indicate a change to pyrolusite but apparently this was not accompanied by a large heat effect. After 670° C, the results were the same as with pure pyrolusite. Sample C8 (fig. 9, g) was a very lightweight artificial oxide which changed from gamma to cryptomelane on heating and then changed over a long range of temperature to bixbyite. It contained a large amount of water, which gave the peak near 150° C.

Samples C14 and C2 (fig. 9, e and f), both of

TABLE 6. *X-ray patterns of the lower oxides of manganese*

Bixbyite [7]			Hausmannite [7]			(No. 42 at 1,200° C) Mn Spinel		
hkl	d	ri	hkl	d	ri	hkl *	d	ri
	A			A			A	
200	4.67	10	101	4.85	70	111	5.1	80
210	4.20	10	112	3.05	50	220	3.09	20
211	3.82	60	200	3.87	20	311	2.63	100
220	3.35	10	103	2.74	90	222	2.51	15
310	2.99	30	202	2.46	100	400	2.17	15
222	2.72	100	004	2.33	50	422	1.769	10
321	2.51	20	114	2.02	60	333	1.668	20
400	2.370	40	..	1.809	10	440	1.532	18
411 330	2.206	20	..	1.775	50	....	.....	....
420	2.104	10	..	1.686	20	....	.....	....
332	2.004	40	..	1.626	15	....	.....	....
422	1.920	10	..	1.568	60	....	.....	....
500 430	1.869	40	..	1.534	80	....	.....	....

* Based on cubic with $a=8.7$ A.

gamma ore of electrolytic origin, gave patterns with a large exothermic break near 700° C. This is thought to result from oxidation of the carbon present. But for this effect, the curve would be similar to other ores.

Cryptomelane and delta samples gave a variety of types of heating curves. It is understandable that this would be true when one considers the range of composition of samples with cryptomelane-type patterns and the fact that these samples are not pure. The first main temperature effect ranges from 550° C in sample 43 (fig. 9, b) to 760° C in sample 36 (fig. 9, d), and as a whole the break is not as pronounced as with pyrolusite. From 700° to 1,100° C, the curves vary greatly. It becomes evident why this is so when the X-ray data is examined. Some cryptomelane samples, such as 43 and 36, go directly from cryptomelane to hausmannite with no intermediate stage of bixbyite. Others change gradually to bixbyite (as 71 and 48). This is probably due to the effect of certain impurities on the transformation. In one case (sample 26), a sample of pyrolusite gave a double break (fig. 8, f) between 600° and 700° C and showed formation of hausmannite with only a partial fomation of bixbyite. Some of the extra thermal effects at high temperatures were unexplained. Sample 43, for example, gave an unidentified phase above 1,200° C. Fusion causes some of the extra breaks at high temperature in cases of certain samples.

VII. Conclusions

1. There are five major types of manganese dioxide of importance to battery technology: (a) Pyrolusite; (b) gamma MnO_2, a form of pyrolusite of fine crystal size, (c) ramsdellite, (d) cryptomelane, a compound of variable composition with essential K or Na, (e) delta MnO_2, apparently a finely crystalline form of cryptomelane.

2. The heating curves of the various types fall into two general groups, one containing pyrolusite, ramsdellite and gamma, the other, cryptomelane and delta.

3. The latter group gives a greater variety of heating curves, partly because of a greater range of composition.

4. Impurities, which may or may not affect the oxides for battery use, have a strong influence on the heating curves, which makes it doubtful if this test can be of definite value, used alone, to evaluate oxides.

5. Gamma samples break down to bixbyite at a lower temperature than well-crystallized pyrolusite.

6. The shape of the fine fractions as seen in the electron microscope is distinctive.

7. The specific surface of commercial samples varies widely, being highest on artificial oxides.

The authors thank the U. S. Geological Survey and the commercial battery manufacturers for furnishing samples of manganese dioxide. They are also grateful to E. S. Newman of this Bureau for help in obtaining the heating curves, and to G. W. Vinal for many helpful suggestions.

VIII. References

[1] H. F. McMurdie, Microscopic and diffraction studies on dry cells and other raw materials, Trans. Electrochem. Soc. **86,** 313 (1944).

[2] W. F. Cole, A. D. Wadsley, and A. Walkly, An X-ray diffraction study of manganese dioxide, Trans. Electrochem. Soc. Preprint 12–2.

[3] A. Van Valkenburg, Jr. and H. F. McMurdie, High temperature X-ray diffraction apparatus, J. Research NBS **38,** 415 (1947) RP1782.

[4] S. Speil, L. H. Berkelhamer, J. A. Pask, and B. Davies, Differential thermal analysis—its application to clays and other aluminous minerals, U. S. Bur. Mines, Tech. Pap. 664.

[5] E. S. Newman and L. S. Wells, Effect of some added material on dicalcium silicate, J. Research NBS **36,** 137 (1946) RP1696.

[6] A. Ferrari, L'esame rongtenographico, dei reticoli cristallini del fluoruro manganoso e del biossido di manganese, Acad. naz. Lincei **3,** 224 (1926).

[7] M. Fleischer and W. E. Richmond, The oxides of manganese, Econ. Geo. **38,** 269 (1943).

[8] O. Glemser, Uber eine neue Modification des Mangan dioxyds, Ber deut. chem. Ges. [B], **72,** 1879 (1939).

[9] F. Schossberger, Uber die rontgenograph Untersuchung von naturlichen un kunstlichen Braunstein, Physik. Ber. **22,** 1340 (1941).

[10] A. St. John, The crystal structure of manganese dioxide, Phys. Rev. **21,** 389 (1923).

[11] J. W. Gruner, Groutite, $HMnO_2$, a raw mineral of the diasporegoethite group, Am. Mineral **32,** 654 (1947).

[12] J. W. Gruner, The chemical relationship of cryptomelane (psilomelane) hollandite and coronadite, Am. Mineral **28,** 497 (1943).

[13] C. Frondel and E. W. Heinrich, New data on hetaerolite hydrohetaerolite, coronadite and hollandite Am. Mineral **27,** 48 (1942).

[14] W. E. Richmond and M. Fleischer, Cryptomelane, a

new name for the commonest of the "Psilomelane" minerals, Am. Mineral **27,** 607 (1942).

[15] L. S. Ramsdell, The unit cell of cryptomelane, Am. Mineral **27,** 611 (1942).

[16] C. Palache, H. Berman, and C. Frondel, The system of mineralogy, 7th ed. (John Wiley and Sons, Inc., New York, N. Y., 1935).

[17] W. Feitknecht and W. Marti, Uber die Oxydation, von Mangen hydroxyd mit molekalaren Sauerstoff, Hel. Chem. Acta **28,** 129 (1945).

[18] M. P. DuBois, Contribution a l'etude des oxyden du Manganese, Ann. de Chimie **5,** 411 (1936).

[19] Von Julius Meyer and R. Kanters, Zur Kenntnis des dreiwertagen Mangans VII, Z. anorg. Chem. **185,** 178 (1929).

[20] H. B. Weiser, Inorganic colloid chemistry, **II,** the hydrous oxides and hydroxides (John Wiley and Sons, Inc., New York, N. Y., 1935).

[21] P. H. Emmett, Symposium on new methods for particle size determination in the subuene range, Am. Soc. Testing Materials (March 1941).

[22] S. Cailiere, S. Henin, and L. Tane, Investigations of the differential thermal analysis of clays, Compt. rend. **223,** 383 (1946).

[23] R. E. Grim and R. A. Rowland, Differential thermal analyses of clay minerals and other hydrous materials, Am. Mineral **27,** 746, 801 (1942).

[24] R. E. Grim, Differential thermal curves of prepared mixtures of clay minerals, Am. Mineral **32,** 49 (1947).

[25] R. W. G. Wyckoff, The structure of crystals, 2d ed. p. 290 (Chemical Catalog Co., New York, N. Y. 1931).

[26] M. H. Jellinek and I. Fankuchen, X-ray diffraction examination of gamma alumina, Ind. Eng. Chem. **37,** 158 (1945).

[27] G. H. Cameron and A. L. Patterson, Symposium on radiography and X-ray diffraction, Am. Soc. Testing Materials, p. 324 (1936).

[28] S. Brunauer, P. H. Emmett, and E. Teller, Absorption of gases in multimolecular layers, J. Am. Chem. Soc. **60,** 309 (1938).

WASHINGTON, June 11, 1948.

U. S. Department of Commerce
National Bureau of Standards

Research Paper RP1942
Volume 41, December 1948

Part of the Journal of Research of the National Bureau of Standards

Laboratory Evaluation of a Method Proposed by Gnam for Measuring the Temperature of Rotating Parts

By Andrew I. Dahl and Paul D. Freeze

A thermocouple application suggested by Gnam for measuring the temperature of rotating parts without slip rings or telemetering has been investigated. A rotating circuit, consisting of a thermocouple in series with the rotor coils of a converter, and a stationary circuit, consisting of the stator coils of the converter and a transformer, are linked magnetically. One thermocouple junction is fixed to the rotating part whose temperature is to be measured, and the other protrudes from a hollow shaft into a furnace. The temperature of the rotating part is stationary circuit, as determined by an oscilloscope, used as a null indicator. Full-scale application of this system seems practicable.

I. Introduction

As one phase of a project at the National Bureau of Standards sponsored by the Bureau of Ships, Department of the Navy, for studying means of measuring temperatures of interest in operating gas turbines, a method proposed by E. Gnam [1] for determining the temperature of rotating parts, such as turbine blades, has been evaluated. The proposed method seemed attractive, as it involved neither slip rings nor telemetering.

The small-scale apparatus used in these tests differs considerably from that of Gnam and was not intended as a prototype for installations on actual turbines. However, it is believed that the present results show that full-scale application would be practicable and provide the basic information required for designing a service unit.

II. Laboratory Test System

The basic elements of the measuring system can be explained by reference to a schematic diagram, figure 1. Two separate circuits, linked magnetically, are involved. All parts of one circuit rotate, while all parts of the other are stationary.

The rotating circuit consists of a nickel-chromel thermocouple in series with the moving coils of a specially designed converter. One junction is located on a rotating part whose temperature is to be determined, and the other is coaxial with and protruding from the hollow shaft of the converter. The protruding junction is surrounded by a furnace whose temperature can be controlled and measured by conventional means. When its temperature is equal to that of the second junction, the only emfs in the rotating circuit are strays that can be kept very small.

The stationary circuit consists of the fixed coils of the converter connected to an impedance-matching transformer and an oscilloscope for indicating output.

The details of the converter used in the laboratory tests are shown in figure 2. In designing this converter, representatives of the Electricity and Optics Division of the National Bureau of Standards were concerned initially as to whether adequate sensitivity could be achieved and particularly as to the proper width of the air gaps in the magnetic circuit. It seemed desirable, therefore, to build the laboratory unit with the pole faces normal to the axis of the shaft and to provide for adjusting the gaps by changing the position of the rotor on the shaft.

It also seemed desirable to connect the two coils of each circuit by magnetic circuits of high permeability. Hence the two poles (each ¼ in. diameter by 5/16 in. long) of each unit were machined on the end of an appropriate cylinder of Mu metal. A cylindrical shield of Mu metal was provided to shield the coils from external magnetic fields. All Mu-metal parts were finally

[1] A new apparatus for measuring the temperature at machine parts rotating at high speeds, E. Gnam, NACA Technical Memorandum No. 1080, April 1945. Original in Motortechnische Z. 5, No. 10, 289 (Oct. 1943).

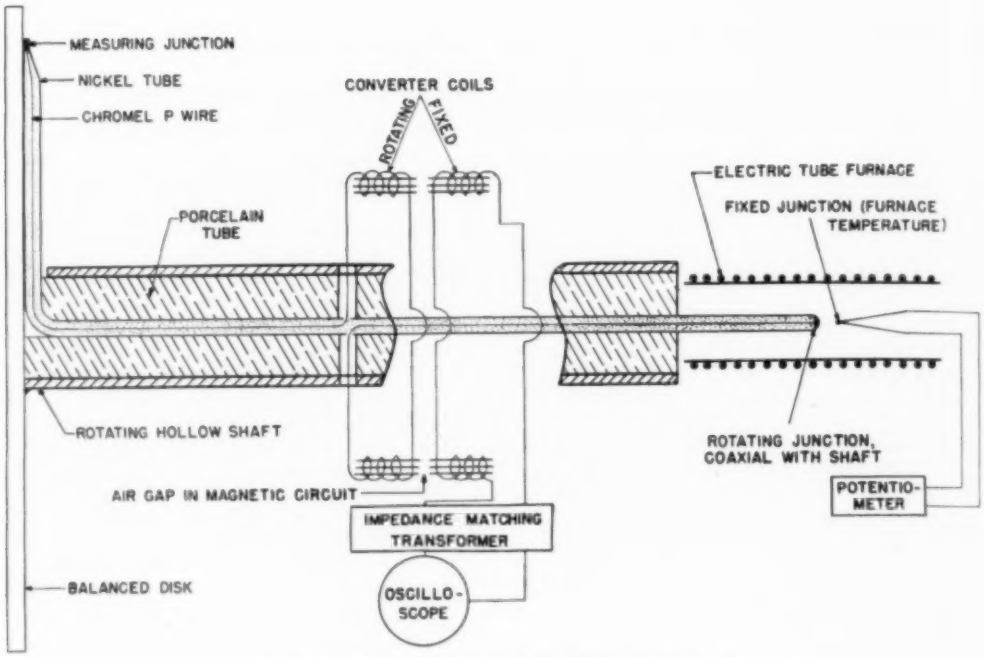

FIGURE 1. *Schematic diagram of the laboratory apparatus.*

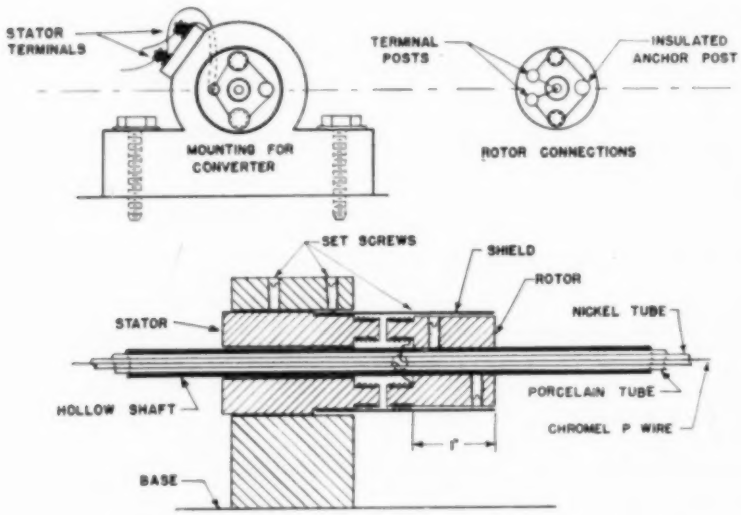

FIGURE 2. *Details of converter used in tests.*

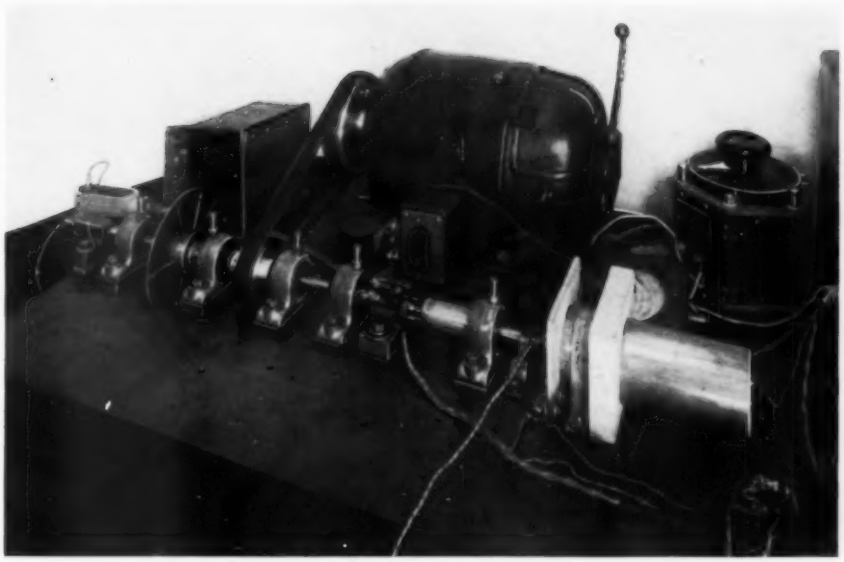

FIGURE 3. *Apparatus used in tests.*

nealed in hydrogen for 4 hours at about 2,000° F improve the permeability, which is normally creased by cold working.

Each of the four coils was wound with 85 turns No. 26 insulated copper wire. The two rotor ils were connected in series, as were the two ator coils. The rotor unit was attached to the aft by set screws. The stator unit and the lindrical shield were mounted in a brass housing ured to the base.

Figure 3 shows the apparatus used in these tests. he shaft is a stainless steel tube ((⅜-in. outside ameter and 0.06-in. wall) provided with five llow-block ball bearings secured to a plane cast n base. These bearings can be identified by e vertical oilers. The longitudinal position of e shaft is fixed by a ball thrust bearing at the xtreme left.

The disk used to simulate a turbine wheel is in. in diameter and 1/16 in. thick, with five equally aced radial slots to reduce warping when flame applied at the periphery. One junction of the ermocouple can be seen in an almost vertical sition on the near side of the disk.

To the rear of the disk stands a metal box, rtly open on the left, which was set over the sk during the tests. An oxyacetylene flame was rected through the opening in this box to heat e periphery of the disk.

The shaft is driven through a light fabric belt by a variable-speed alternating-current motor. Final adjustment of the shaft speed to any chosen value, as indicated by a Strobotac, was made by applying a rubber brake to the left face of the motor pulley.

The converter is shown in its mount between the last two bearings on the right. Near the right-hand bearing and surrounding the shaft is the cylindrical shield of Mu metal, which, during operation, is moved to the left to surround the coils of the converter that are barely visible because of their small size.

Mounted at the right of the base plate and concentric with the shaft is the tube furnace, which surrounds the second junction of the rotating thermocouple. The temperature of this furnace is controlled by adjusting a Variac and indicated by a chromel-alumel thermocouple. The necessary instruments, being standard items, are not shown in the photograph.

One of the problems in a system of this type is to design the rotating thermocouple so that the emf generated by its rotation in external magnetic fields (such as that of the earth) are negligibly small. This can be accomplished by making the two thermoelements coaxial, which in turn can be achieved by using one in tubular form around the other in the form of an insulated wire. Since

the thermoelectric properties of the combination nickel-chromel *P* are favorable, and since nickel tubing can be procured and worked with ease, this construction was used for the rotating couple. A porcelain tube served to center the thermocouple and to insulate it from the shaft. The nickel tube was insulated from the rotating disk by a sleeve of fiber glass.

The resistance of the rotating circuit at room temperature is about 2.5 ohms, divided about equally between the rotor coils and the thermocouple. All electrical connections in the stationary indicating circuit are made with shielded wire.

III. Calibration and Performance Tests

Although the measurements in actual service would be made by using the oscilloscope as a null instrument to indicate equality of temperature of the two rotating junctions, the potentialities of the method can be studied best when the temperatures of these two junctions differ by a known amount. Hence most of the present measurements were of deflections of the oscilloscope beam. To make such observations comparable it is necessary to keep the amplification factor constant, and this was done, as nearly as was practicable, throughout all of the observations reported here.

Several series of tests were made, only one operating factor being varied in each.

1. Deflection Versus Temperature Difference

At a constant shaft speed of 5,000 rpm and gap width of 0.003 in., and with the rotating disk at the temperature of the room, the temperature of the junction rotating within the furnace was raised by small increments, with the results shown in figure 4. The average deflection under these conditions was 0.077 in./° F.

The observations shown in figure 4 were made over a period of several weeks, during which the gap width was changed many times. Inability to readjust the gap to exactly 0.003 in. is responsible for part of the spread. Some of it was probably caused by imperfect magnetic shielding and some by small changes in amplification.

It will be noted that the furnace temperature had to be made 7 deg F less than the disk temperature in order to obtain a minimum deflection. It is believed that this effect is produced by residual magnetism in the Mu metal, which produced a

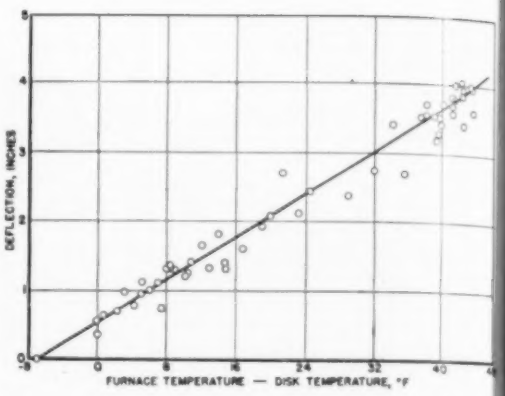

FIGURE 4. *Sensitivity at 5,000 rpm with an air gap of 0.003 in.*

small voltage in the stator of the converter when no current flowed through the rotor coils.

The differences in temperature between furnace and disk were measured in this case directly by a chromel-alumel thermocouple having one junction in the furnace and the other at the disk. Since the junction could not be held against the disk while the latter was rotating, measurements of ΔT were made before and after each operation, and the average of these two values was plotted in the figure.

In addition to the effect of residual magnetism, the effects of external magnetic fields and of unequal air gaps were not completely eliminated, as evidenced by the fact that the oscilloscope trace could never be made a horizontal straight line. This trace, however, showed a sudden and marked change when the net voltage in the rotating circuit was zero. Because of this sudden change in the trace, there is no difficulty in determining the null condition.

2. Deflection Versus Shaft Speed

Again the gap was maintained at 0.003 in. and three trials were made over the range 1,000 to 10,000 rpm. In one the rotating circuit was open, so that the effect of residual magnetism in the magnetic circuit was determined. The results are shown in the lower curve of figure 5. In the others, constant differences of 10 and 20 deg F were maintained between the furnace and the disk, with the results shown in the upper curves of figure 5. All of the results show the

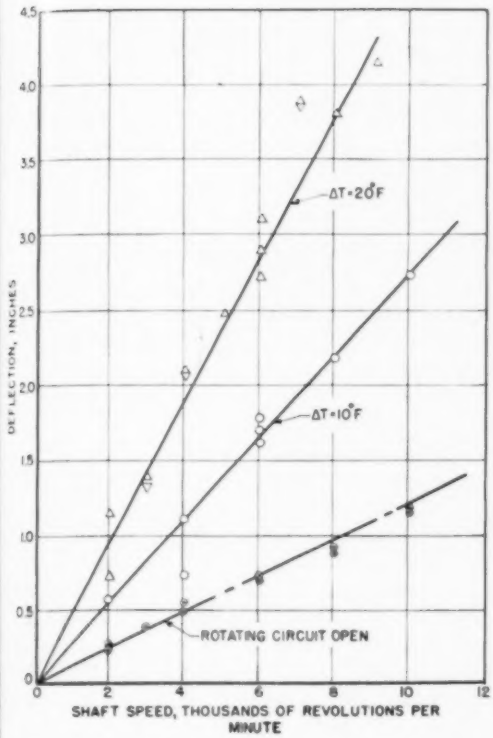

FIGURE 5. *Sensitivity as a function of shaft speed with an air gap of 0.003 in.*

the observed deflection is directly proportional to the shaft speed.

Typical oscilloscope traces at 6,000 rpm and with temperature differences of 10 and 20 deg F are shown in figure 6. The squares on the oscilloscope scale are 0.1 in. on a side.

3. Deflection Versus Gap Width

The magnetic linkage between the stator and rotor of the converter and hence also the voltage induced in the rotor are a function of the width of the air gaps. With shaft speed constant at 6,000 rpm and with a constant temperature difference of 10 deg F between the furnace and the disk, a series of tests was made at various gap widths from 0.002 to 0.021 in., with the results shown in figure 7. As was anticipated, the sensitivity decreases rapidly as the air gap is increased from a small value, and this decrease becomes more gradual as the gap is widened.

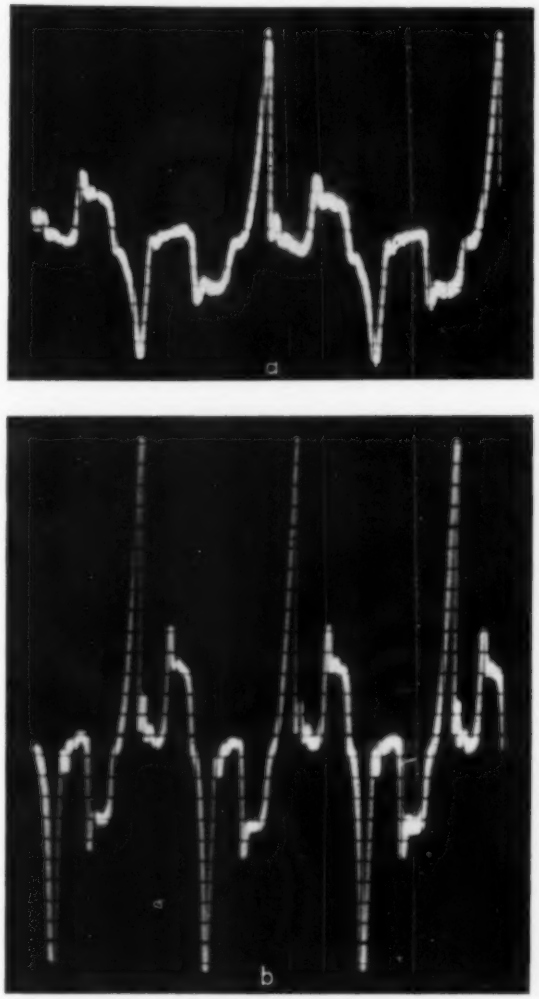

FIGURE 6. *Typical oscilloscope traces.*

a, $\triangle T = 10°$ F; rpm = 6,000; b, $\triangle T = 20°$ F; rpm = 6,000.

If it is necessary, from a mechanical standpoint, to design the operating unit with a gap width that is relatively great, the loss in sensitivity therefrom can be overcome by increasing the number of poles on the converter. From the data of figure 7 it can be seen that increasing the gap width from 0.003 to 0.01 in. reduced the sensitivity by 50 percent. However, some sensitivity can be regained by the use of a four-pole converter instead of the present two-pole converter.

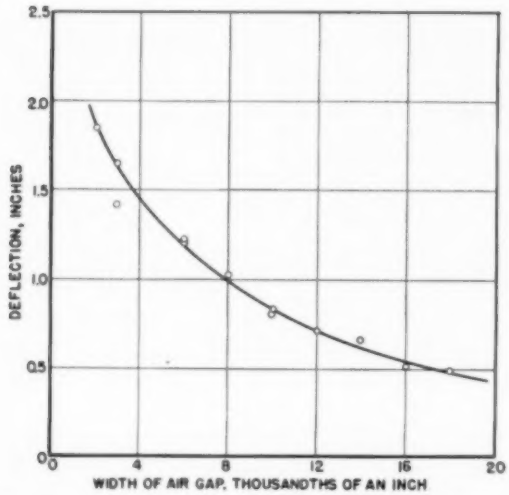

FIGURE 7. *Sensitivity as a function of the width of the air gap.*

rpm=6,000; $\triangle T$=10° F.

4. Tests at Elevated Temperature

In all of the tests that have been discussed, the disk was at the temperature of the room. The results, however, are applicable at higher temperatures, since the changes in resistance and in thermoelectric properties of the nickel-chromel couple with temperature are of secondary importance.

Performance tests were also conducted by heating the periphery of the disk with an oxy-acetylene flame. A metal housing around the disk during these tests served to concentrate the flame on the periphery of the disk and to shield other parts of the apparatus against overheating.

At speeds up to 10,000 rpm and disk temperatures to 1,500° F, it was a simple matter to detect by eye a marked change in the pattern on the oscilloscope screen when the net emf in the rotating circuit became zero. Thus there is every reason to believe that the method can be applied for measuring the temperatures of rotating parts.

IV. Discussion of Possible Full-Scale Application

It is obvious that a system such as has been described would be difficult to install on an existing full-scale turbine. Actually it seems probable that provision for installing such a system would have to be made during the design and construction of the turbine. Another serious disadvantage is that the system would become quite complicated if it were to be used for measuring the temperature at more than one point, since a multiple unit would require either switching from one working junction to another or a converter for each working junction.

Some features of the laboratory unit would require considerable change in full-scale application. Principal among these is the air gap in the magnetic circuit of the converter. In the laboratory apparatus longitudinal movement of the shaft was prevented by thrust bearings, and there was no thermal expansion to contend with. Hence the width of the gap could be fixed by positioning the rotor on the shaft. In the actual turbine the shaft may move longitudinally, so that the stator of the converter would have to follow the movement of the shaft, if gap width is to remain constant. A mechanism capable of accomplishing such positioning of the stator would be quite complex.

It is believed, however, that the converter can be redesigned along the following lines to eliminate all need for moving the stator. The pole pieces of both stator and rotor should be made radial rather than parallel to the shaft, so that the rotor could be surrounded by the stator, in the manner indicated in figure 8. The air gap would thus be an annulus, and it seems reasonable that the gap between stator and rotor poles could be of the order of 0.01 in.

If the minimum practicable air gap is decided upon and the normal speed of the shaft is known, the circuit and pick-up unit required to provide the desired sensitivity can then be designed. D

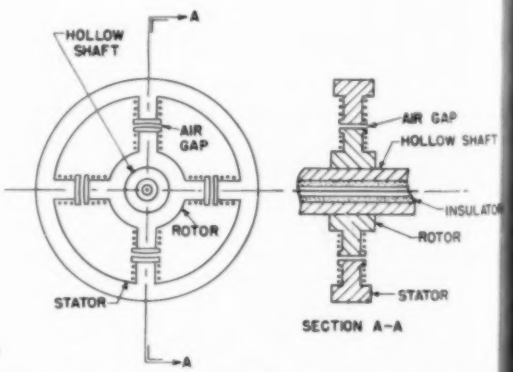

FIGURE 8. *Schematic diagram of a converter for full-scale applications.*

should be noted that if a multipolar unit is to be used, the matching of impedances within the circuit must be considered. It is believed that a unit having a sensitivity of 10° F is feasible with an air gap of 0.01 in. and a shaft speed of 6,000 rpm.

It will be noted that the above estimates pertain to the accuracy with which the temperature indicated by the measuring junction is observed and not to the actual temperature of the turbine blade. If the measuring junction is completely buried in the blade and in good thermal contact with it, these two temperatures may be nearly the same.

As to the rotating thermocouple itself, the use of an insulated chromel *P* wire within a nickel tube would seem to be well suited for full-scale application.

The rotating parts of the laboratory apparatus were not balanced dynamically. Since the full-scale application would be so much larger than the laboratory version, it is possible that the problem of achieving proper balance would be more serious. With radial rotor coils located at a considerable distance from the axis of the shaft, it may be necessary to confine the windings mechanically.

Since the magnetic shielding of the laboratory apparatus was not entirely satisfactory, even more effective shielding should be applied to the full-scale converter.

V. Conclusion

The present tests on a laboratory scale indicate that the method examined has considerable promise for measuring the temperature of rotating parts. Principal limitations are that the system would be difficult to install on an existing turbine and that it is suited for measuring the temperature at one point only. On the basis of present experience, several suggestions are made as to the design of a full-scale unit.

The assistance of F. K. Harris and A. W. Spinks of the Electricity and Optics Division in the design of the converter and in improving the electrical system, and of A. F. Baillie in the mechanical design and construction of the entire test system, is gratefully acknowledged.

Washington, July 27, 1948.

811266—49——5

U. S Department of Commerce
National Bureau of Standards

Research Paper RP1943
Volume 41, December 1948

Part of the Journal of Research of the National Bureau of Standards

Amides of Glucuronic, Galacturonic, and Mannuronic Acids

By Harriet L. Frush and Horace S. Isbell

Heretofore the amides of glucuronic, galacturonic, and mannuronic acid were not known, and methods were not available for their preparation. It has now been found possible to obtain the amides of uronic acids from the corresponding 1-amino-uronamides by selective hydrolysis of the glycosylamino group. An aqueous solution of the 1-amino-uronamide is treated with an acid or a suitable cation exchange resin that replaces the glycosylamino group by a hydroxyl, forming the free amide. The new compounds, like the sugars, have a free reducing group, and hence they are capable of existing in the pyranose, furanose, and open-chain forms and of displaying mutarotation. D-Glucuronamide, D-mannuronamide, and D-galacturonamide were separated in the alpha pyranose form. The beta pyranose modification of D-galacturonamide was also obtained. The amides are stable crystalline substances, that should prove to be useful representatives of a new class of carbohydrate derivatives.

I. Introduction

The development of methods for the production of uronic acids [1] [1] and the recognition of their possible therapautic uses [2] make desirable the investigation of the amino derivatives of these substances. In a previous paper from this laboratory [3] it was shown that mannuronic lactone (I) reacts with 2 moles of ammonia, and that the crystalline product, 1-aminomannuronamide (II) contains a glycosylamino group and an amide group.[2] It has now been found that similar products can be obtained from the esters or lactones of glucuronic and galacturonic acids and that all three 1-amino-uronamides can be selectively hydrolyzed to give new crystalline amides (III, IV, V, VI) of the corresponding uronic acids. Although the amides of a number of substituted uronic acids are known [4], previous attempts to prepare the unsubstituted amides have been unsuccessful, presumably because of contamination with the 1-amino-uronamides. This difficulty has now been overcome by first isolating the amino-uronamide, and thereafter removing the glycosylamino group.

In all three 1-amino-uronamides, the glycosylamino group is so labile that it is hydrolysed

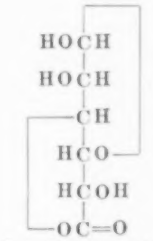

I. D-Mannuronic lactone.

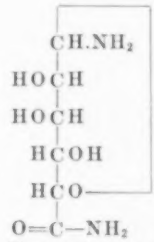

II. 1-Aminomannuronamide.

III. α-D-Mannuronamide.

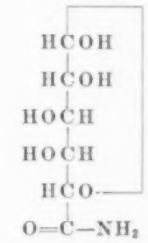

IV. α-D-Galacturonamide

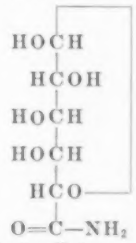

V. β-D-Galacturonamide.

VI. α-D-Glucuronamide.

[1] Figures in brackets indicate the literature references at the end of this paper.

[2] The uronic acids also react with alkyl and aryl amines to form substituted 1-amino-uronamides. A number of these compounds and some of their characteristic reactions will be described in a future publication.

slowly by dilute acid at room temperature. Figures 1, 2, and 3 show the pH titration curves obtained when 0.1 *N* HCl was added portion-wise to 75 ml of a solution containing 0.275 g of the 1-amino-uronamide. Sufficient time was allowed after each addition of acid for the pH of the solution to attain equilibrium. The 1-aminomannuronamide used was substantially pure, but the analogous derivatives of galacturonic and glucuronic acid were amorphous or partially crystalline, and, as indicated by the titration curves, had a purity of 87 and 68 percent, respectively. The nearly horizontal portion on the left of the curve is caused by the cleavage of ammonia from the glycosylamino group; the leveling off of the curve at the right of the figure is caused by hydrolysis of the amide nitrogen. On evaporation, solutions obtained after the addition of acid to pH 4 gave the pure crystalline amide corresponding to the 1-amino-uronamide used.

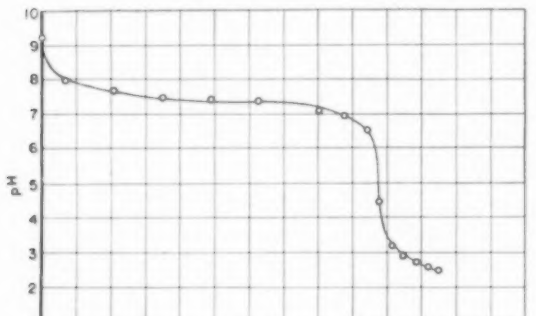

FIGURE 1. pH *titration curve for 1-aminomannuronamide.*

0.1 *N* HCl added portionwise to 75 ml of a solution containing 0.275 g of 1-aminomannuronamide.

Conversion of the 1-amino-uronamide to the corresponding amide was accomplished in several ways. The amino compound was treated with an equivalent quantity of dilute acid, and the resulting ammonium salt of the acid employed was removed by means of ion-exchange resins. When sulfuric acid was used for the hydrolysis, the ion-exchange resins were unnecessary, and the sulfate ion was removed by an equivalent quantity of barium hydroxide. It was also found that ion exchange resins of the carboxylic acid type were particularly suitable for hydrolysis of the 1-amino-

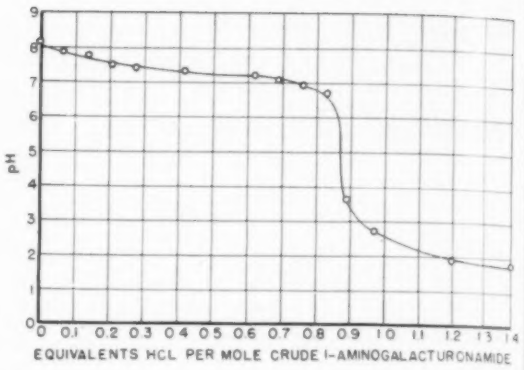

FIGURE 2. pH *titration curve for 1-aminogalacturonamide.*

0.1 *N* HCl added portionwise to 75 ml of a solution containing 0.275 g of crude 1-aminogalacturonamide.

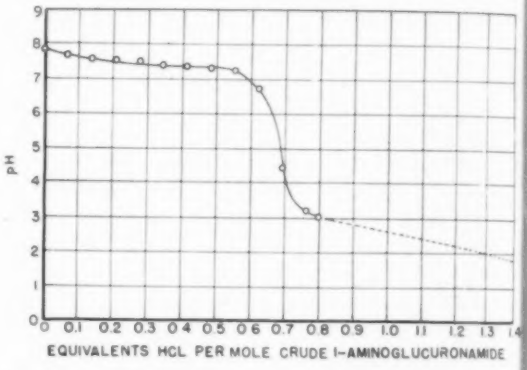

FIGURE 3. pH *titration curve for 1-aminoglucuronamide.*

0.1 *N* HCl added portionwise to 75 ml of a solution containing 0.275 g of crude 1-aminoglucuronamide.

uronamides, and that when these resins were used, previous acid treatment was unnecessary.

The new amides are substituted sugars capable of existence in the open chain, and the several ring modifications characteristic of the aldoses. Two crystalline modifications of galacturonamide have been isolated. One of these is an alpha pyranose analogous to α-D-galactopyranose; the other is a hydrate having the beta pyranose structure. Mannuronamide crystallizes as an anhydrous alpha pyranose, and glucuronamide as an alpha pyranose hydrate.

It was previously reported [3] that 1-aminomannuronamide could be acetylated and that the crystalline acetate, on deacetylation, yielded crystalline 1-*N*-acetylaminomannuronamide. In analogous manner, 1-*N*-acetylaminogalacturon-

amide has now been obtained; a comparative study of the properties of these two substances will be reported in a later publication.

II. Experimental Details

1. D-Mannuronamide

D-Mannuronamide was prepared from the 1-amino-D-mannuronamide previously reported, by removal of the glycosylamino group with a cation exchange resin of the carboxylic acid type, as follows: Twenty grams of 1-aminomannuronamide was dissolved in 500 ml of water, and the solution was passed slowly through a column of cation exchange resin.[3] The effluent was treated with a decolorizing carbon, filtered, and concentrated to a thick sirup, to which methanol was added from time to time until the total volume was 75 ml. After 24 hr, the truncated prisms that had formed were collected on a funnel, washed with aqueous methanol, and dried in a vacuum desiccator; they weighed 11.5 g. A second crop weighing 4.8 g was obtained by concentrating the mother liquor and again adding methanol. Mannuronamide was recrystallized in high yield by dissolving the material in water at room temperature, concentrating the solution to a sirup under reduced pressure, and cautiously adding methanol as crystallization proceeded. After one recrystallization, mannuronamide melted sharply at a point between 145° and 150° C, which depended on the rate of heating. In 4-percent aqueous solution, $[\alpha]_D^{20} = +2.4$ (1.4 min); $-10.4°$ (30 min). The properties were unchanged by further recrystallization. Analysis: Calculated for $C_6H_{11}O_6N$: C, 37.31; H, 5.74; N, 7.25. Found: C, 37.5; H, 5.9; N, 7.3.

Mannuronamide has also been prepared equally satisfactorily by the methods described for the preparation of galacturonamide and glucuronamide.

2. 1-Amino-D-galacturonamide

Fifty grams of α-D-galacturonic acid was converted to the methyl ester by dissolving it in 1,500 ml of a 0.02 *N* solution of HCl in absolute methanol and maintaining the solution at 0° C for 65 hr [5]. The methyl galacturonate was not isolated, but a stream of dry ammonia gas was bubbled through the solution until it was substantially saturated, and it was then allowed to stand for several days in the refrigerator. The partially crystalline material that separated was collected on a filter, washed with methanol, and dried in air. It weighed 24 g. The crude material gave the following analysis: Calculated for $C_6H_{12}O_5N_2$: C, 37.50; H, 6.29; N, 14.58. Found: C, 36.2; H, 6.5; N, 13.3.

1-Aminogalacturonamide is difficult to purify; it separates from solution as double-refracting clumps of indeterminate structure that sometimes contain amorphous material. Titration of a solution of the crude 1-amino-galacturonamide with dilute acid gave the curve shown in figure 2. The inflection indicates a purity of approximately 87 percent, and shows that the material is largely a glycosyl amine analogous to 1-aminomannuronamide (see fig. 1). Three minutes after dissolution in water the crude 1-aminogalacturonamide in 2-percent solution had a specific rotation of $-21.4°$. On standing there was a gradual drift in rotation, and after 102 hr $[\alpha]_D^{20} = -24.4°$. The substance was used without further purification for the preparation of crystalline galacturonamide.

3. D-Galacturonamide

To 20 g of crude 1-amino-D-galacturonamide dissolved in 500 ml of water, 145 ml of 0.7 *N* H_2SO_4 was added gradually over the course of 2 hr. The resulting solution was then treated with an exactly equivalent quantity of a solution of barium hydroxide in order to remove sulfate ion. The mixture was filtered, and the filtrate concentrated under reduced pressure to a thick sirup, which crystallized after standing for 2 days in a vacuum desiccator over calcium chloride. The crystals were separated, washed with aqueous methanol and air-dried; they weighed 15.0 g. A small second crop was separated from the mother liquor.

In a separate experiment the ammonium and sulfate ions were removed by successive passage of the acid-treated solution through columns of cation and anion exchange resins,[4] and the amide was obtained from the effluent in approximately the same yield as that reported above.

Galacturonamide crystallizes in both the alpha and beta modifications. The former is anhydrous, the latter a monohydrate. To prepare the beta modification, 10 g of the crude galacturonamide

[3] Amberlite IR-50, Resinous Products & Chemicals Co., Philadelphia, Pa.

[4] Zeo-Rex H and De-Acidite, Permutit Co., New York, N. Y.

was dissolved with slight warming in 10 ml of water, and the solution was treated with a decolorizing carbon, filtered, and allowed to stand for 2 hr at room temperature. Ethanol was then added almost to the point of turbidity (approximately 60 ml). In the course of several hours, long, slender prisms separated abundantly. The crystals were collected on a filter, washed with aqueous ethanol, and air-dried; they weighed 7.7 g. Additional material was reclaimed from the mother liquor. β-Galacturonamide hydrate was twice recrystallized by the method described. Analysis: Calculated for $C_6H_{11}O_6N.H_2O$: C, 34.12; H, 6.21; N, 6.63. Found: C, 34.2; H, 6.5; N, 6.9.

β-Galacturonamide monohydrate is stable in air, but when heated in a vacuum oven at 60° C, it slowly loses water. In a melting point tube heated at about 6 deg a minute, the substance melts at 113° to 116° C. It then resolidifies and melts with decomposition at 172° to 178° C. In 4-percent aqueous solution $[\alpha]_D^{20}=-21.4°$ (3 min); +14.6° (22 hr).

By crystallization in the following manner anhydrous α-galacturonamide was obtained: Ten grams of pure β-galacturonamide monohydrate was dissolved in 20 ml of warm water, and the solution was filtered with the aid of a decolorizing carbon and concentrated in vacuum to a thick sirup ($n_D^{20}=1.507$). Thirty milliliters of hot methanol was added, and the mixture was kept in a stoppered flask at a temperature of 60° C for a period of 4 hr. α-Galacturonamide crystallized in good yield in slender flat plates, which were separated, washed with methanol, and air-dried. The yield was 8 g. Analysis: Calculated for $C_6H_{11}O_6N$: C, 37.31; H, 5.74; N, 7.25. Found: C, 37.3; H, 5.9; N, 7.2.

α-Galacturonamide melts with decomposition at 172 to 178° C, is soluble in water, slightly soluble in methanol and ethanol, and insoluble in ether. In 4-percent aqueous solution $[\alpha]_D^{20}=+80°$ (3 min); +15.9° (22 hr).

4. 1-*N*-Acetylamino-D-galacturonamide

In the procedure described below, 1-amino-D-galacturonamide was acetylated and the O-acetyl groups of the sirupy acetate were removed by ammoniacal methanol to yield 1-*N*-acetylaminogalacturonamide. Five grams of finely powdered 1-aminogalacturonamide was added to an ice-cold mixture containing 20 ml of acetic anhydride and 50 ml of pyridine. The suspension was shaken at 0° C for 20 min and at room temperature for 18 hr.[5] Ten volumes of petroleum ether were then added in order to precipitate the acetate, which separated as a sirup.[6] The sirupy phase was extracted successively with several portions of petroleum ether and finally was dissolved in methanol. The methanolic solution was saturated at 0° C with ammonia and concentrated under reduced pressure to a sirup that was then extracted three times with isopropyl ether. When the residue was dissolved in a few milliliters of ethanol and allowed to stand, large rectangular prisms separated from the solution in the course of 2 days. The yield of crude product was 3 g.

To recrystallize, *N*-acetylaminogalacturonamide was dissolved in six parts of hot water. The solution was filtered and cooled to room temperature, and isopropanol was added almost to the point of turbidity. The hydrated crystals, large rectangular prisms, when air-dried, melted at 103° to 107° C, $[\alpha]_D^{20}=-48.1°$ (water, c=2). The constants were unchanged after further crystallization. Analysis: Calculated for $(C_8H_{14}O_6N_2)_2.5H_2O$: C, 34.41; H, 6.86; N, 10.03; H_2O, 16.13. Found: C, 34.6; H, 6.9; N, 10.0; H_2O, 15.8.

5. 1-Amino-D-glucuronamide

Six grams of pure glucurone was suspended in 120 ml of absolute methanol at 0° C, and a stream of dry ammonia gas was passed into the solution until it was substantially saturated. The material was stored for several days in the refrigerator, and during this time a flocculent amorphous precipitate formed. When separated, and dried over calcium chloride in a vacuum desiccator, it weighed 3.5 g. In 2-percent aqueous solution the crude material showed a gradual change in specific rotation over the course of many days. $[\alpha]_D^{20}=-14.0°$ (5 min); −7.9° (28 hr); −3.9° (5 days).

Figure 3 shows the change in pH when a solution of the crude 1-aminoglucuronamide was titrated slowly at room temperature with 0.1 *N* acid. The inflection is less sharp than that of

[5] The acetylation mixture assumed a striking deep-blue color, which disappeared slowly after the addition of petroleum ether.

[6] Extraction with chloroform was found to be impracticable because of the relatively high solubility of the crude acetate in water. In one preparation the acetylation mixture was poured into ice water, and after several chloroform extractions, most of the acetate was still present in the aqueous portion.

titration curve of 1-aminomannuronamide but indicates the presence of a glycosyl amine with a purity of approximately 68 percent. The crude 1-aminoglucuronamide was used without purification for the preparation of crystalline glucuronamide.

6. D-Glucuronamide

Crude 1-amino-D-glucuronamide (3.1 g) was dissolved in 50 ml of water, and 128 ml of 0.0993 *N* HCl was added over the course of 1 hr.; the pH of the resulting solution was 3.0. The material was then passed through columns of cation and anion exchange resins [7] to remove ammonium chloride, and concentrated under reduced pressure to a thin sirup, which crystallized on addition of methanol. The crystals weighed 2.35 g.

To recrystallize, one part of the glucuronamide was dissolved in three parts of water with slight warming. The solution was filtered with the aid of a decolorizing carbon, and isopropyl alcohol was added almost to the point of turbidity. D-Glucuronamide monohydrate crystallized in high yield in the form of slender prisms, which were separated after 24 hr and dried in a vacuum desiccator over calcium chloride. Heated slowly, they melted at 113° to 117° C, resolidified, and finally decomposed above 150° C. $[\alpha]_D^{20}=+78°$ (3 min); +31.6° (22 hr) (water, c=2). Analysis: Calculated for $C_6H_{11}O_6N.H_2O$; C, 34.12; H, 6.21; N, 6.63. Found: C, 34.2; H, 6.2; N, 6.7.

III. Summary

Methods are reported for the preparation of the amides of mannuronic, galacturonic, and glucuronic acids. It has been found that the corresponding 1-amino-uronamides prepared by a method previously reported are selectively hydrolysed at room temperature by dilute acid, which replaces the glycosylamino group by hydroxyl. After removal of the ammonium salt of the acid employed, the free uronamides were crystallized. These substances, like the sugars, have a free reducing group and hence are capable of existing in the pyranose, furanose, and open-chain forms, and of displaying mutarotation.

D-Mannuronamide $C_6H_{11}O_6N$, truncated prisms, melting point 145° to 150° C with decomposition, has a specific rotation, $[\alpha]_D^{20}$, of +2.4° (1.4 min) changing in 30 min to −10.4° (water, c=4). It thus appears to be an alpha pyranose modification.

D-Galacturonamide crystallizes in two modifications: an anhydrous alpha pyranose form, $C_6H_{11}O_6N$, slender flat plates, melting point 172° to 178° C with decomposition, has a specific rotation, $[\alpha]_D^{20}$, of +80° (3 min), and +15.9° (22 hr) (water c=4); a beta pyranose hydrate $C_6H_{11}O_6N.H_2O$, long slender prisms, melting point 113° to 116° C with decomposition, has a specific rotation, $[\alpha]_D^{20}$, of −21.4° (3 min), and +14.6° (22 hr) (water, c=4).

By low-temperature acetylation of 1-aminogalacturonamide followed by deacetylation with ammonia, a crystallinehydrate of 1-*N*-acetylaminogalacturonamide was obtained, $(C_8H_{14}O_6N_2)_2.5H_2O$, which melted at 103° to 107° C, and had a specific rotation, $[\alpha]_D^{20}$, of −48.1° (water, c=2).

D-Glucuronamide was obtained by selective hydrolysis of crude 1-aminoglucuronamide. The crystals, long slender prisms, were found to be an alpha pyranose hydrate $C_6H_{11}O_6N.H_2O$, melting point 113° to 117° C. $[\alpha]_D^{20}=+78°$ (3 min); +31.6° (22 hr) (water, c=2).

The authors are indebted to Nancy B. Holt for assistance in various phases of the work, and to Rolf A. Paulson for the analyses reported in this paper.

IV. References

[1] H. H. Mottern and H. L. Cole, J. Am. Chem. Soc. **61,** 2701 (1939); W. W. Pigman, J. Research NBS **25,** 301 (1940) RP1325; H. S. Isbell and H. L. Frush, J. Research NBS **32,** 77 (1944) RP1576; H. L. Frush and H. S. Isbell, J. Research NBS **33,** 401 (1944) RP1617; **37,** 321 (1946) RP1750.

[2] E. A. Peterman, J. Lancet **67,** 451 (1947).

[3] H. L. Frush and H. S. Isbell, J. Research NBS **41,** 11 (1948) RP1898.

[4] S. Luckett and F. Smith, J. Chem. Soc. **1940,** 1506; H. G. Sammons, J. Shelswell, and R. T. Williams, Biochem. J. **35,** 557 (1941); S. P. James and F. Smith, J. Chem. Soc. **1945,** 739.

[5] E. F. Jansen and R. Jang, J. Am. Chem. Soc. **68,** 1457 (1946).

WASHINGTON, SEPTEMBER 24, 1948.

[7] Amberlite IR-100-H and IR-4-B, Resinous Products and Chemicals Co., Philadelphia, Pa.; other commercially available ion exchange resins are equally satisfactory.

U. S. Department of Commerce
National Bureau of Standards

Research Paper RP1944
Volume 41, December 1948

Part of the Journal of Research of the National Bureau of Standards

Absorption Spectra of Methane in the Near Infrared

By Richard C. Nelson,[1] Earle K. Plyler, and William S. Benedict

A grating spectrometer with a PbS cell for detector has been used for the measurement of the infrared absorption bands of methane in the region of 1.66 μ. Many lines of the P, Q, and R branches of the 1.66-μ band have been observed.

These are well resolved and are of the correct structure and spacing for the F_2 component of $2\nu_3$. The lines for values of J up to 10 are sharp, showing no indication of splitting due to interaction with neighboring states or to centrifugal distortion. The rotational constants obtained for this band are $B'=5.178$, $\zeta_3=0.0346$. The latter value is lower than in the ν_3 fundamental. Other bands observed are more complex and irregular, presumably due to mutual interaction.

In the infrared spectrum of methane there are two strong bands, the fundamental frequencies, ν_3 at 3020.3 cm^{-1}, and ν_4 at 1306.2 cm^{-1}. Because of the symmetry of the molecule, the other two fundamentals ν_1 at 2914.2 cm^{-1} and ν_2 at 1526 cm^{-1}, are not active in the infrared, although these frequencies may appear in combination bands with the other frequencies and their overtones, to give bands in the near infrared. Many previous studies, both experimental and theoretical, have been made of the methane molecule. A good discussion of the general problem, including references to the literature, may be found in Herzberg's book [1].[2] One of the unsettled problems concerns the influence of the Coriolis forces in the fine structure of the overtone and combination bands. Accordingly it was thought that further experimental data with higher resolution would be of value. The present paper reports such data in the regions from 1.5 to 1.7 μ, and from 1.15 to 1.19 μ, with particular emphasis on one band of relatively simple structure, the F_2 component of $2\nu_3$, at about 6,004 cm^{-1}. Quite recent studies on the atmospheric absorption have revealed the presence of methane bands [2]. McMath, Mohler, and Goldberg [2] have also studied the $2\nu_3$ band under high resolution.

In our studies, high resolution was obtained by the use of a specially designed grating instrument, which employs a PbS photo-conducting cell constructed by Cashman [3] as the detecting unit. One of the authors [4] has previously given a description of the instrument and only a brief outline of the arrangement will be repeated here.

Figure 1 shows the plan of the optical parts of the spectrometer. The system is designed according to the arrangement described by Pfund [5]. The paraboloidal mirrors have a focal length of 2 m and are 12 in. in diameter. The grating has 15,000 lines per inch and the ruled surface is 3 by 5 in., giving a theoretical resolution in the first order of 75,000. An ellipsoidal mirror, with a conjugate focal ratio of 1:3, was used to focus the energy from the exit slit onto the PbS cell. With this magnification, spectrometer slits 18 mm in length could be used with the PbS cell, which possessed a sensitive surface 7 mm long. A tungsten lamp was used as the source, and a quartz lens focused the filament on the entrance slit of the spectrometer. The absorption cell, which was 60 cm in length, was placed in front of the entrance slit. A chopper, which interrupts the radiant energy approximately 1,000 times a second, was placed immediately in front of the entrance slit.

For any selected region the grating was rotated continuously. The driving mechanism has five scanning speeds, and the Speedomax recorder has six speeds for the chart, a selection which made it possible to have dispersions of 50 to 0.02 A/mm on the recording chart.

A special narrow-band-pass amplifier was used with the PbS cell. The over-all voltage gain was

[1] Research Associate, Northwestern University.
[2] Figures in brackets indicate the literature references at the end of this paper.

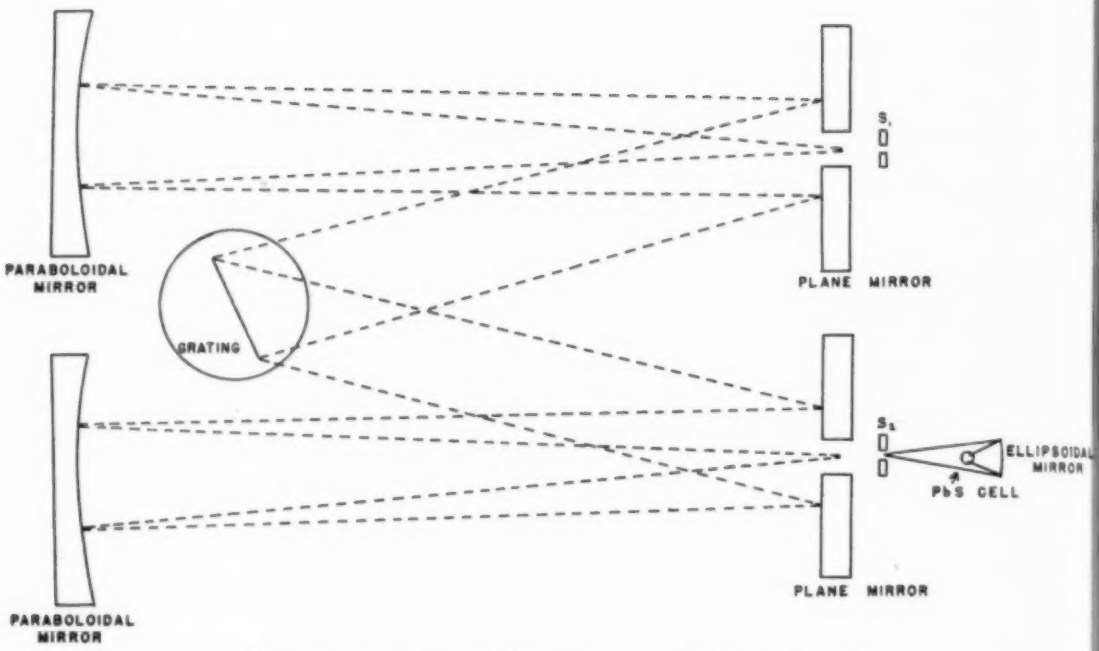

FIGURE 1. *Arrangement of the optical components of the spectrometer.*

approximately 1.8×10^8. The details of the amplifier have been given in a previous publication [4].

In the region around 1.66 μ, runs were made at two dispersion scales on the recorder chart. Measured wavelengths are largely based on two runs made with slits 0.7 cm^{-1} spectral width, the dispersion on the chart being about 15 cm^{-1}/in. A commutator in the gear train driving the grating actuated a pen that placed marks on the paper corresponding to equal increments of motion of the nut upon the tangent screw, which moves the grating.

Wavelengths were measured with reference to lines of the Hg spectrum. A record of the spectrum in all orders over the desired region was made. Then using the lines 15295.2, 5460.74 (3d order), and 4358.35 A (4th order), a quadratic expression was obtained for wavelength in terms of measurements on the scale impressed on the record. An equation of the form $\lambda_1=\lambda_0+da+d^2b$ is obtained, where λ_1 is the wavelength corresponding to any number d, representing the difference between respective scale readings for λ_1 and λ_0. The λ_0, a, and b are constants that are determined from the scale readings of the three lines used for calibration. During continuous operation of the instrument, the line 15295.2 A was recorded, followed by the absorption spectrum of CH_4, and the record was completed by recording 4358.35×4. The measured separations of the initial and final Hg lines were alike, and the previously found expression was used for computing wavelengths of absorption lines.

Another run was made with slits 0.3 cm^{-1} spectral width, and dispersion on the chart of about 5 cm^{-1}/in. to bring out fine detail.

Measurements were made both on natural gas (80% CH_4) and Matheson CH_4, 99 percent pure, in a cell 60 cm long. The light source in all cases was a tungsten filament.

Figure 2 shows the results for the 1.66-μ region. The strong rotational lines of the P and R branches of the $2\nu_3$ band of methane can readily be identified. About 19 lines are observed for the R branch with the 60-cm cell at atmospheric pressure. In addition there are present a number of less intense lines which appear between these lines. The less intense lines repeat well on successive runs. Beyond the 10th line of the P branch, the structure becomes complex. This structure may be part of another band. There is a narrow region of the spectrum without any lines, followed by another set of com-

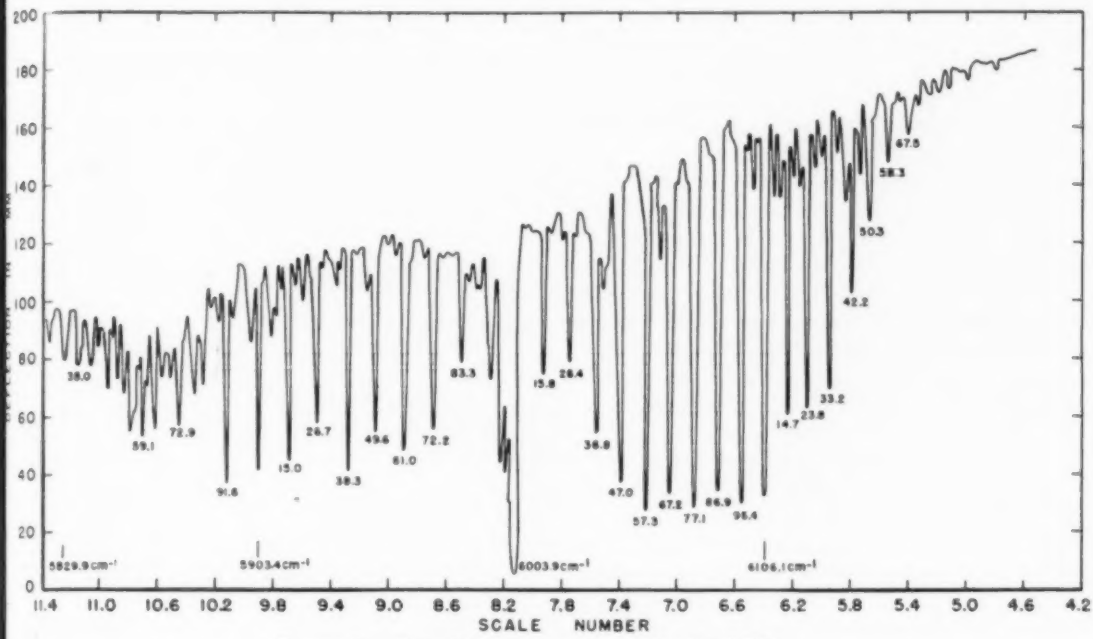

FIGURE 2. *Absorption spectrum of the 1.66-μ band* CH_4.
The cell was 60 cm in length and the gas at atmospheric pressure.

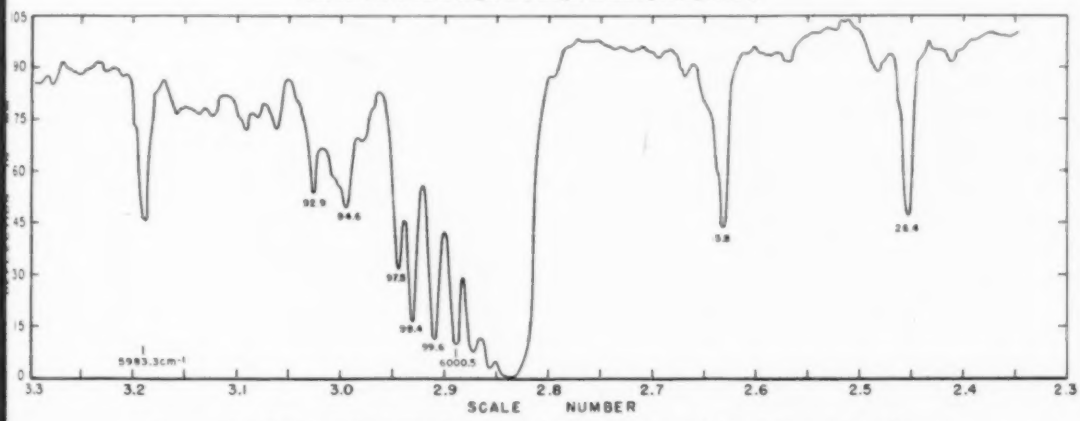

FIGURE 3. *Center of the 1.66-μ band, showing fine structure states of the zero branch.*

ex lines. These lines may be part of a combination band, but no term assignment fits very well. When the absorption of the gas was measured with spectral slit of 0.3 cm^{-1}, the zero branch showed more structure. Figure 3 shows the central part of the band. The gas was at atmospheric pressure for these observations. When a smaller pressure of gas was used, better separation of the stronger components of the Q branch was obtained, but the less intense components were not present.

The intensities given are measured to within 2 percent. The stronger lines may actually be more intense than the measurements indicate. That is, the finite slit widths may make it impossible to find the maximum absorption at the center of the lines. All faint lines that measure less than 3 percent are arbitrarily marked 2 percent in intensity. The intensity figures in the table denote the percentage absorption of the minimum point of the lines.

All the observed lines of appreciable intensity for the region are listed in table 1. Wave numbers of some of the lines are marked for identification. A sufficient number of lines are numbered on the figure so that the tables can be related to the experimental results. The band for the 1.10- to 1.13-μ region, shown in figure 4, does not have the regular structure as observed in the $2\nu_3$ band. The wavelengths and intensities of all the lines are given in table 2.

The $2\nu_3$ band gives sufficient data for calculating some of the constants of methane. The only lines in the CH_4 absorption that can be given a definite interpretation are listed in table 3. These are the strongest lines in the region, and form a band consisting of P, Q, and R branches of simple structure, the band bearing a marked resemblance to the ν_3 fundamental. The vibrational transition involved, $2\nu_3$, is the first overtone of that fundamental. The theory of the structure of this band has been given by Johnston and Dennison, [6] and by Shaffer, Nielsen, and Thomas [7]. The first-named authors have pointed out that the upper level is six-fold degenerate in the zeroth-order approximation, but that the first-order Coriolis interaction due to the internal angular momentum of the vibration removes the degeneracy, giving six different energies for each value of the rotational quantum number J. At $J=0$, these may be grouped into three sub-bands of different symmetry. Transitions are permitted from the ground state to only one of these sub-bands, the triply-degenerate F_2; and for each branch, $\Delta J=-1$, 0, or $+1$, transitions are permitted to only one of the three components, thus giving the band of simple structure, as observed.

The second-named authors have considered the effect of second-order interactions, which in principle may further remove the degeneracy of the energy levels, splitting each J level into a number of components of different K, and which may permit transitions from the ground state to the E subband. (These authors gave selection rules and intensities for the band which differ from those of Johnston and Dennison [6], and which appear to be in error.) The second-order interactions are of two types; first, those due to centrifugal stretching and distortion of the molecule; and second, those due to resonance interactions between the vibrational level and other neighboring levels of the same total (vibrational plus

TABLE 1. *Wavelength, wave number, and intensity of the observed lines in the 1.66-μ region*

Wavelength	Wave number	Absorption	Wavelength	Wave number	Absorption
A	*cm*$^{-1}$	*Percent*	*A*	*cm*$^{-1}$	*Percent*
16112.7	6204.6	3	16859.9	5929.6	5
16143.6	6192.7	2	16868.0	5926.7	50
16148.5	6190.8	2	16884.7	5920.9	10
16165.9	6184.1	2	16894.6	5917.4	5
16175.6	6180.4	2	16901.4	5915.0	50
16185.3	6176.7	2	16918.9	5918.9	20
16200.3	6171.0	2	16934.8	5903.4	50
16209.6	6167.5	5	16943.2	5900.4	20
16233.7	6158.3	10	16968.5	5891.6	55
16254.8	6150.3	20	16977.2	5888.6	10
16260.2	6148.2	5	16995.3	5882.4	25
16267.2	6145.6	30	17003.6	5879.5	25
16276.2	6142.2	30	17022.7	5872.9	30
16281.4	6140.3	15	17030.6	5870.2	20
16288.2	6137.1	10	17040.1	5866.9	15
16309.2	6133.2	50	17048.4	5864.1	30
16309.6	6129.7	5	17052.8	5859.1	30
16315.3	6127.3	5	17076.4	5854.4	30
16325.1	6123.8	50	17081.8	5857.6	20
16331.4	6121.5	10	17090.1	5849.7	15
16338.6	6118.8	10	17100.5	5846.2	20
16349.4	6114.7	55	17110.6	5842.7	10
16356.0	6112.3	10	17117.2	5840.5	15
16362.2	6110.0	10	17133.3	5835.0	15
16372.6	6106.1	70	17148.3	5829.9	15
16386.6	6100.9	10	17164.7	5824.3	20
16398.7	6096.4	70	17200.9	5812.0	15
16424.2	6086.9	70	17209.4	5809.2	10
16450.6	6077.1	75	17217.2	5806.5	10
16477.4	6067.2	65	17222.6	5804.7	20
16488.6	6063.1	15	17232.6	5801.3	10
16504.5	6057.3	70	17244.2	5797.5	10
16532.5	6047.0	65	17256.3	5793.4	15
16553.1	6039.5	15	17265.3	5790.4	25
16560.5	6036.8	50	17279.3	5785.7	20
16589.0	6026.4	30	17304.1	5777.4	25
16618.4	6015.8	30	17315.1	5773.7	15
16651.1	6003.9	85	17345.5	5763.6	15
16659.8	6000.8	65	17378.5	5752.6	15
16663.2	5999.6	55	17395.5	5747.0	10
16666.5	5998.4	50	17415.1	5740.5	10
16677.1	5994.6	25	17456.1	5727.1	15
16681.8	5992.9	20	Q BRANCH[a]		
16688.3	5990.6	5			
16692.9	5988.9	5	16650.4	6004.2	100
			16651.1	6003.9	100
			16652.7	6003.4	100
16708.5	5983.3	25	16654.7	6002.7	100
16725.2	5977.4	5	16656.9	6001.9	90
16739.5	5972.2	45			
16771.1	5961.0	50	16659.8	6000.8	90
16781.3	5957.4	70	16663.2	5999.6	90
			16666.5	5998.4	80
16803.1	5949.6	45	16669.0	5997.5	65
16811.3	5946.7	15	16674.3	5995.6	25
16826.0	5941.5	5			
16835.2	5938.3	50	16677.1	5994.6	45
16848.5	5933.6	5	16681.8	5992.9	40

[a] These data refer to fig. 3.

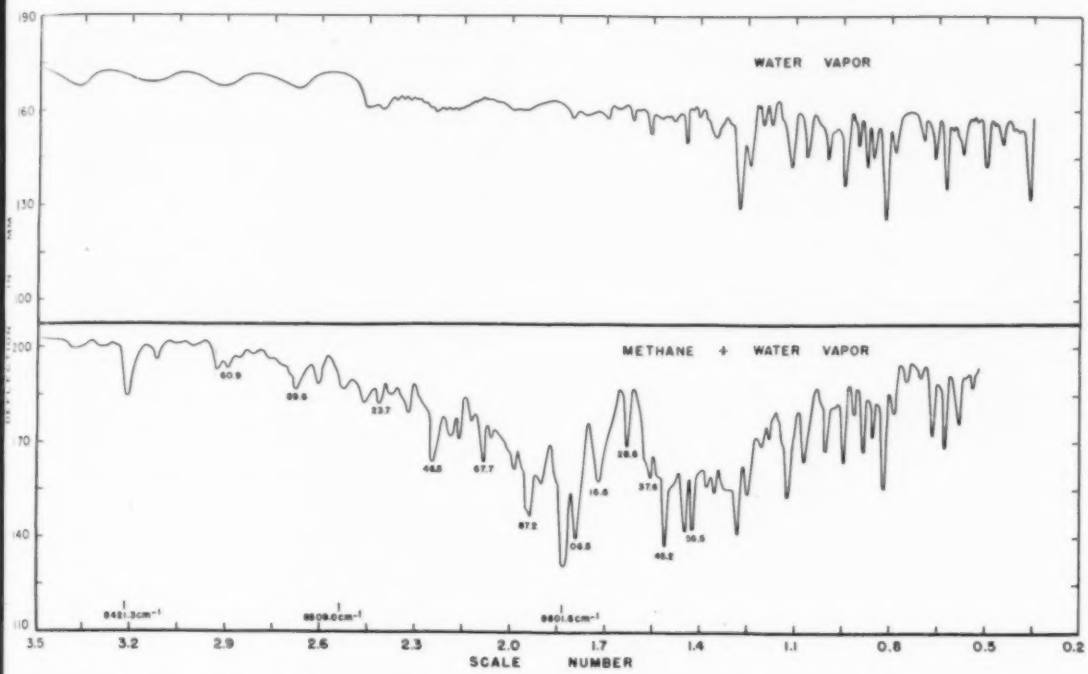

FIGURE 4. *Upper curve shows the absorption of water vapor in the atmosphere; lower curve is the absorption of methane interposed on the atmospheric absorption.*

TABLE 2. *Wavelength, wave number, and intensity of observed lines in the 1.16-μ region*

Wave number	Wave-length	Absorp-tion	Wave number	Wave-length	Absorp-tion
cm^{-1}	*A*	*Percent*	cm^{-1}	*A*	*Percent*
8656.5	11548.9	30	8567.7	11668.5	15
8645.2	11563.9	30	8546.5	11697.5	15
8637.6	11574.0	20			
8628.6	11586.2	15	8523.7	11728.8	10
8616.6	11602.3	20	8509.0	11749.0	5
			8489.6	11775.9	5
8606.5	11615.9	30	8460.9	11815.9	2
8601.6	11622.6	35	8421.3	11871.4	10
8587.2	11642.0	25			

rotational) symmetry. The centrifugal splitting is roughly independent of the particular vibrational level in question, and is proportional to $(J+1)^2$. The resonance splitting, proportional to $J(J+1)$, is very dependent on the vibrational state. Thus in the ν_4 fundamental [8], the splitting is experimentally observable as low as $J=3$, and has been well accounted for [11] by the second-named effect. In the ν_3 fundamental [8] however, and equally so in the $2\nu_3$ band here studied, the experimental observation is that the lines of the P and R branches are sharp and narrow, and agree in position and intensity with the predictions of the first-order theory, except for relatively small correction for centrifugal stretching, up to $J=11$. This shows that the second-order interactions leading to splitting are of comparatively minor importance in $2\nu_3$. Presumably such interactions are much more important for the other overtone and combination bands in the region, resulting in bands of much more complex structure which we are unable to interpret.

The following equations represent the observed lines to the required accuracy:

$$\left.\begin{aligned} R \text{ branch: } & \nu=\nu_0+B'[(J+1)(J+2)+2\zeta(J-1)]-B''J(J+1)-4D(J+1)^3 \\ Q \text{ branch: } & \nu=\nu_0+B'[(J(J+1)-6\zeta]-B''J(J+1) \\ P \text{ branch: } & \nu=\nu_0+B'[(J-1)J-2\zeta(J+2)]-B''J(J+1)+4DJ^3. \end{aligned}\right\} \quad (1)$$

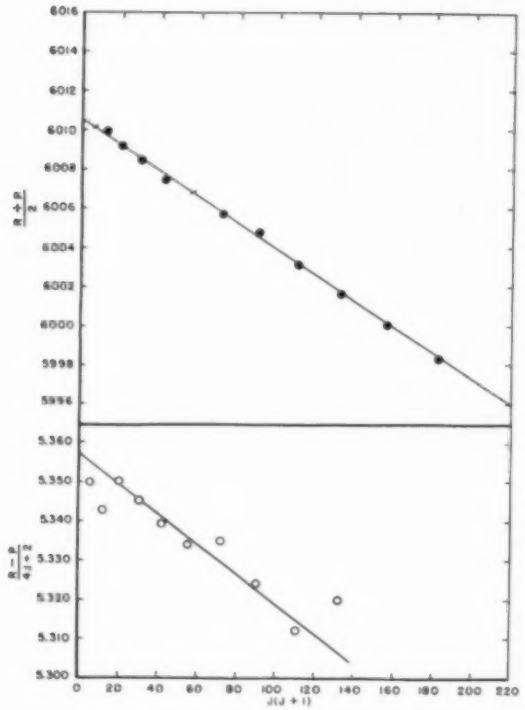

FIGURE 5. *Plot of the experimental data for the determination of the molecular constants.*

Upper plot is based on eq 3, and the lower plot is based on eq 2.

The following combinations of eq. 1 are useful in deriving the values of the constants:

$$\frac{R(J)-P(J)}{4J+2}=B'(1+\zeta)-2D[J(J+1)+1] \quad (2)$$

$$\frac{R(J)+P(J)}{2}=Q(J)+B'(1+3\zeta)= \quad (3)$$
$$\nu_0+B'(1-3\zeta)+(B'-B'')J(J+1).$$

In these equations, ν_0 is the band origin, B' and B'' are the effective reciprocal moments of inertia for the upper and ground vibrational levels, respectively, J is the rotational quantum number of the lower level, ζ is the constant representing the angular momentum due to the upper-state vibration, and D is the constant representing the correction due to centrifugal stretching. As explained above, the effect of the centrifugal forces is both to stretch the molecule, resulting in an equal lowering of all levels of equal J, and to distort it, resulting in a splitting of those levels. We have calculated both effects for the ground vibrational state, making use of the published formulas [7]; the former effect is larger by a factor of about 3. Hence it is permissible, for lines where the experimental splitting is unobservable, to make use of a single constant D to correct for the centrifugal stretching, as is the common practice with diatomic or linear molecules.

In Figure 5 are plotted the values of the left-hand sides of eq 2 and 3 as a function of $J(J+1)$. The points fall quite well on straight lines, up to $J=11$, the slopes and intercepts yielding the following combinations of constants: $B'(1+\zeta)=5.357$ cm^{-1}, $D=1.9\times10^{-4}$ cm^{-1}, $\nu_0+B'(1-3\zeta)=6010.45$ cm^{-1}, $(B'-B'')=0.066$ cm^{-1}. The value of D is not well determined by the data of figure 5; the slope as drawn is the theoretically calculated value, and also fits the data for the ν_3 fundamental.

In order to obtain the values of the individual constants, use is made of data from other bands to obtain B'', the rotational constant of the ground state, common to all bands. By working up in an analogous way the data of Nielsen and Nielsen [8] on the ν_3 fundamental, and of Dickinson, Dillon and Rasetti [9] on the Raman lines of the same band, we obtain $B''=5.244$ cm^{-1}. (This compares favorably with the value proposed by Child [10], 5.252 cm^{-1}, from an analysis of the ν_2 and ν_3 fundamentals. The perturbations in the latter band, however, make it somewhat less suitable for a precise evaluation). This yields for the P sub-band of 2 ν_3, $B'=5.178$ cm^{-1}, $\zeta=0.0346$, $\nu_0=6005.81$ cm^{-1}. The corresponding values for ν_3 are $B'=5.207$ cm^{-1}, $\zeta=0.0536$, $\nu_0=3018.3$ cm^{-1}. If there were only harmonic terms in the potential energy, the value of ζ for the two bands should be the same. The observed difference is far beyond the experimental error and must be due to anharmonic terms in the potential energy.

According to eq 3, there should be a constant difference of $B'(1+3\zeta)=5.72$ cm^{-1} between $[R(J)+P(J)]/2$ and $Q(J)$. This is very nearly what is observed, although the lines in the Q branch, being not quite fully resolved, are not known with great accuracy. There is, however, a slight but definite anomaly near $J=9$, as shown by the differences in table 3. It would appear that the Q branch is weakly perturbed by another vibrational level with zero internal angular momentum and a different value of B', so that cross-

TABLE 3. *Identified lines in the $2\nu_2$ band of* CH_4

J	R(J)		Q(J)		P(J)	
	Observed	Calculated	Observed	Calculated	Observed	Calculated
	cm^{-1}	cm^{-1}	cm^{-1}	cm^{-1}	cm^{-1}	cm^{-1}
0	6015.8	6016.17	.....	.....	.....	.....
1	6026.4	6026.38	.....	6004.60	5994.2	5994.22
2	6036.8	6036.83	6004.2	6004.34	5983.3	5983.25
3	6047.0	6047.10	6003.9	6003.94	5972.2	5972.14
4	6057.3	6057.25	6003.4	6003.41	5961.0	5960.93
5	6067.2	6067.23	6002.7	6002.75	5949.6	5949.58
6	6077.1	6077.05	6001.9	6001.96	5938.3	5938.13
7	6086.9	6086.71	6000.8	6001.04	5926.7	5926.59
8	6096.4	6096.19	5999.6	5999.98	5915.0	5914.94
9	6106.1	6105.52	5998.4	5998.75	5903.4	5903.20
10	6114.7	6114.66	5997.5	5997.47	5891.6	5891.36
11	6123.8	6123.61	5995.6	5996.02	5879.5	5879.43
12	6133.2	6132.39	5994.6	5994.44	5866.9	5867.43
13	6142.2	6140.94	5992.9	5992.72	5854.4	5855.35
14	6150.3	6149.33	.....	.....	.....	.....
15	6158.3	6157.52	.....	.....	.....	.....

ng with the F_2° component occurs near this point. The perturbing level may be the A_1 sublevel of 2 , or possibly some other combination band with A_1 symmetry.

In addition to the good agreement between the observed and calculated frequencies, the relative intensities of the lines, especially in the P and R branches, show excellent agreement with those calculated by Jahn [11]. In particular, the relative weakness of the lines with $J''=5$ and strength of those with $J''=6$ is markedly apparent.

The ultimate goal of a study of the CH_4 spectrum is to derive constants that will yield the observed positions, effective moments of inertia, and effective ζ's of all observable overtone and combination bands, and to explain these in terms of a potential function. From the small number of completely interpreted bands this is not yet possible, although the present work is a short step in that direction. Further experimental study under high resolution of CH_4 and its deuterated derivatives, and further theoretical studies using a potential function of somewhat greater simplicity than that of Shaffer, Nielsen and Thomas [7], are required. A simplification of the experimental band structure may be expected if measurements are made at low temperatures.

References

[1] Gerhard Herzberg, Molecular spectra and molecular structure (D. Van Nostrand Co., New York, N. Y., 1945).

[2] Marcel V. Migeotte, Phys. Rev. **73,** 519 (1948); R. R. McMath, O. C. Mohler, and L. Goldberg, Phys. Rev. **73,** 1203 (1948).

[3] R. J. Cashman, Proc. Nat. Elec. Conf. **2** (Chicago, 1946).

[4] R. C. Nelson and W. R. Wilson, Proc. Nat. Elec. Conf. **3** (Chicago, 1947).

[5] A. H. Pfund, J. Opt. Soc. Am. & Rev. Sci. Instr. **14,** 337 (1927).

[6] D. M. Dennison and M. Johnston, Phys. Rev. **47,** 93 (1935).

[7] W. H. Shaffer, H. H. Nielsen, and L. H. Thomas, Phys. Rev. **56,** 895, 1051 (1939).

[8] A. H. Nielsen and H. H. Nielsen, Phys. Rev. **54,** 118 (1938).

[9] R. G. Dickinson, R. P. Dillon, and F. Rasetti, Phys. Rev. **34,** 582 (1929).

[10] W. H. J. Childs, Proc. Roy. Soc. (London) **153,** 555 (1936).

[11] H. A. Jahn, Proc. Roy. Soc. [A], **168,** 469, 495 (1938); H. A. Jahn and W. H. J. Childs, Proc. Roy. Soc. [A], **169,** 451 (1939).

WASHINGTON, October 1, 1948.

U. S. Department of Commerce
National Bureau of Standards

Research Paper RP1945
Volume 41, December 1948

Part of the Journal of Research of the National Bureau of Standards

Transmittance of Near Infrared Energy by Binary Glasses[1,2]

By Jack M. Florence, Francis W. Glaze, Clarence H. Hahner, and Ralph Stair

A study has been made of the transmittance of near infrared energy by a number of binary glasses. Of the systems studied, the lithia-silica and lead oxide-silica were found to have the highest transmittance of energy in the range of wavelengths from 3.0 to 5.0 microns. The transmittance of lithia-silica is compared with that of the other alkali-silica glasses. Values of transmittance are given for lead silicate glasses of higher lead content than have been previously reported in the literature.

I. Introduction

Published data concerning the relation between the transmittance of infrared energy and the composition of glasses have been limited to a relatively few investigations. A compilation of these investigations is given by Eitel, Pirani, and Scheel [1][3] in *Glastechnische Tabellen*, which was published in 1932. Since that date, Gerlovin [2] has published a study of borate, silicate, and phosphate glasses; a study of glasses incorporating rare earth and other oxides has been published by Stair and Faick [3]. The majority of these studies are concerned with the absorption bands of complex glasses. In this paper only data on experimental binary glasses are considered.

II. Preparation of the Glasses

The glasses that were made for this work were melted in platinum crucibles of 150- to 300-g capacity. The batch materials used were of the highest commercial purity as used in the manufacture of optical glass, and no special processes were used to purify the materials before use. The only heavy metal that was present as an impurity in sufficient quantities to have any possible effect on the transmittance was iron. The following quantities as Fe_2O_3 were present in the batch materials used:

Powdered silica (SiO_2)	0.018 percent.
Li_2CO_3	Trace.
Na_2CO_3	Less than 0.001 percent.
K_2CO_3	Do.
Litharge (PbO)	0.001 percent.

The glasses were melted and fined in a platinum resistance furnace in about 6 hr and then poured into a mold to form a sample about ¼ in. thick. The samples were of a quality equivalent to that of optical glass. Samples were prepared for measurement by grinding and polishing into plates having plane parallel faces 1 in. square.

III. Composition of the Glasses

Measurements were made on glasses of lithium silicate, sodium silicate, potassium silicate, and lead silicate. The lithium silicate glass had a composition close to that of lithium metasilicate ($Li_2O.2SiO_2$). Compositions appreciably different from this ratio could not be cooled without devitrification [4]. The sodium silicate glasses contained 21.28, 24.79, and 31.02 mole percent of Na_2O. The potassium silicate glass contained 20.35 mole percent of K_2O. These glasses, listed in table 1, are within such ranges of compositions that comparisons may be made by mole-percentage and weight-percentage compositions within 3 percent. A stable K_2O-SiO_2 glass of 32.41 mole percent of K_2O could not be made for direct comparison with the Li_2O glass. The lead silicate

[1] Made possible by a transfer of funds from the Department of the Navy, Bureau of Ships, to the National Bureau of Standards.
[2] This paper will also appear in the December issue of the Journal of the American Ceramic Society.
[3] Figures in brackets indicate the literature references at the end of this paper.

811266—49——6

glasses made contained 70.86, 79.91, and 88.08 weight percent of PbO. Potassium and lead silicate [5] glasses beyond these ranges, either could not be melted and cooled without difficulty or were not sufficiently resistant to moisture so that a polished sample could be made for transmission measurements. The compositions of these glasses, by chemical analysis, are given in table 1.

TABLE 1. *Glass compositions*

Glass No.	SiO_2		Li_2O		Na_2O		K_2O		PbO		Fe_2O_3	
	Weight percent	*Mole percent*	*Weight percent*	*Mole percent*	*Weight percent*	*Mole percent*	*Weight percent*	*Mole percent*	*Weight percent*	*Mole percent*	*Weight percent*	*Mole percent*
1	80.72	67.58	19.26	32.41							0.017	0.005
2	78.01	78.71			21.97	21.28					.015	.006
3	74.60	75.21			25.38	24.79					.015	.006
4	68.29	68.97			31.70	31.02					.014	.006
5	71.37	79.64					28.61	20.35			.016	.007
6	29.13	60.44							70.86	39.55	.009	.01
7	20.08	48.28							79.91	51.70	.008	.01
8	11.91	33.44							88.08	66.54	.007	.02

IV. Near Infrared Transmittances

The infrared spectra of glasses have wide regions of absorption and transparency. The transmittance for glasses of the same batch composition will vary with the thickness of the sample and the presence in the glass of small amounts of impurities, among which are iron and nickel oxides and water vapor [6].

The spectral transmissions were determined radiometrically by means of a fluorite prism mirror spectrometer, Nernst glower, and a vacuum thermopile. A detailed description of the method is given in previous publications [7, 8, 9, 10, 11, and 12]. These data are given in figures 1 to 5 without correction for reflectance.

The simplest glass from the standpoint of chemical composition, though not ease of preparation, is fused silica. The transmission curve for transparent fused silica (fig. 1) indicates a high transmittance to about 3.5μ. The absorption band at 2.8μ is characteristic of silicate glasses, but it is a minimum in fused silica. Two additional absorption bands are present at the wavelengths of 3.7 and 4.45μ. The thickness of the sample was 2.85 mm.

1. Transmittances of the Alkali-Silica Glasses

The transmittances of a representative lithium silicate glass 1 are shown in figure 2 for a sample 5.74 mm thick. This thickness of sample gives a good contrast for the range of wavelengths from 3.0 to 5.0 μ. In figure 3 the transmission

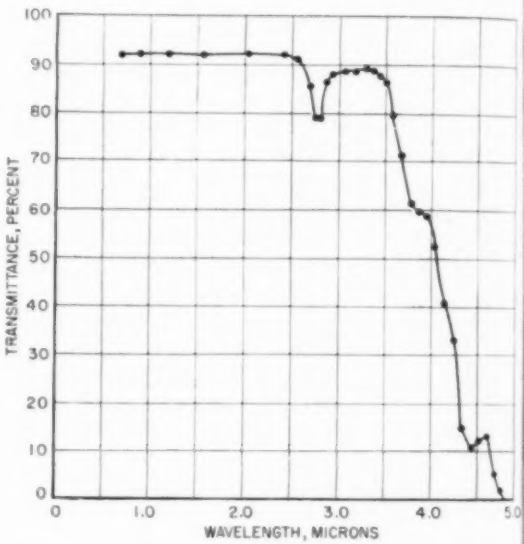

FIGURE 1. *Transmittance of infrared energy by fused silica.*
Thickness of sample = 2.85 mm.

curves of the sodium silicate glasses 2, 3, and 4 are shown. The highest transmittance is shown by glass 3, which is near the composition of the eutectic reported by Kracek [13] for the Na_2O-SiO_2 system. A comparison of the transmittance of the lithium silicate glass 1 with that of the sodium silicate glasses 2, 3, and 4, shows that the lithium silicate glass has a higher transmittance of infrared energy than any of the sodium silicate glasses. The potassium silicate glass 5 is similar

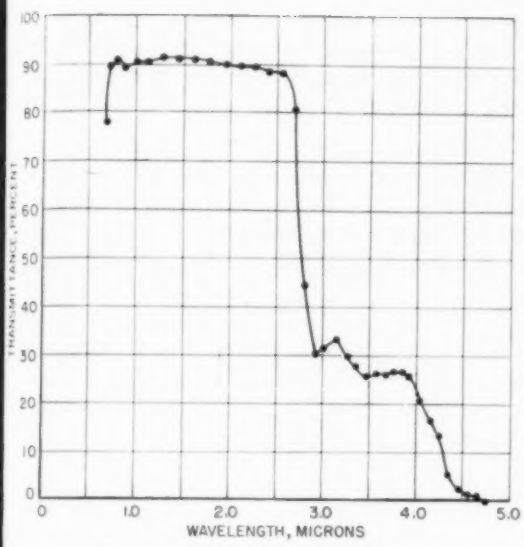

FIGURE 2. *Transmittance of infrared energy by a lithium silicate experimental glass.*

Thickness of glass 1=5.74 mm.

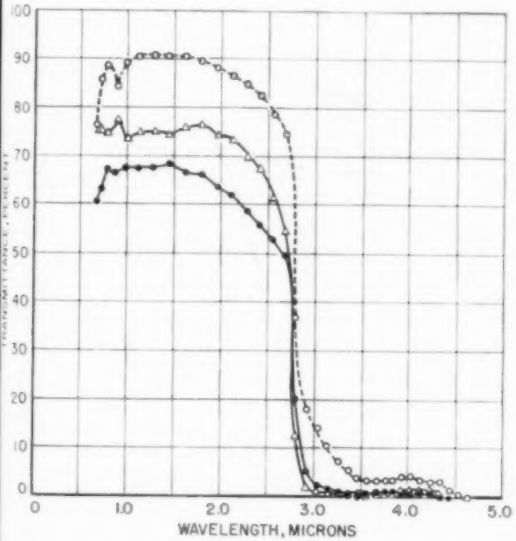

FIGURE 3. *Transmittance of infrared energy by sodium silicate experimental glasses.*

Thickness of glass 2=6.21 mm; glass 3=4.84 mm; and glass 4=4.67 mm. ●, Glass 2; ○, glass 3; △, glass 4.

the sodium silicate glasses in the transmittance of infrared energy, as shown in figure 4. Potassium silicate glass 5 is equivalent to the sodium silicate glass 2 on a mole percentage basis.

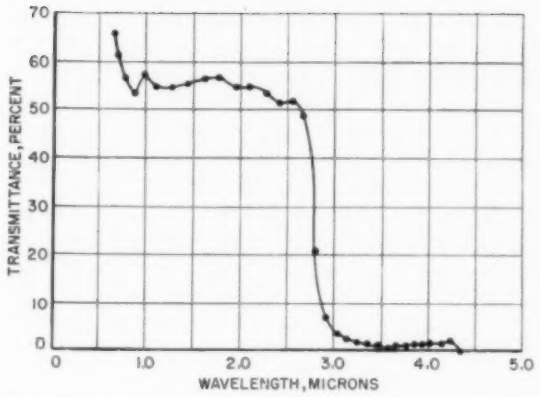

FIGURE 4. *Transmittance of infrared energy by potassium silicate glass.*

Thickness of glass 5=4.45 mm.

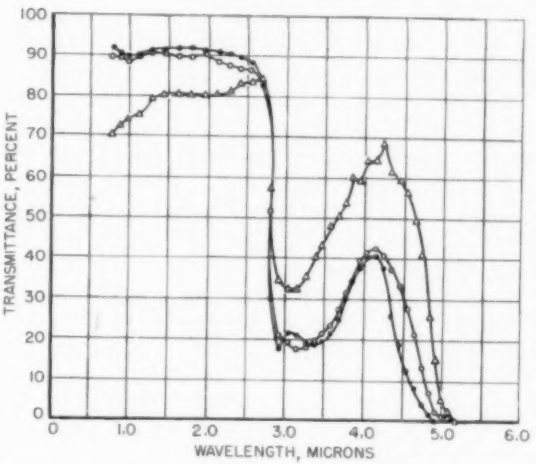

FIGURE 5. *Transmittance of infrared energy by lead silicate glasses.*

Thickness of glass 6=3.00 mm; glass 7=3.21 mm; and glass 8=2.81 mm. ●, Glass 6; ○, glass 7; △, glass 8.

2. Transmittances of Lead-Silica Glasses

Gerlovin [2] stated that the greatest transmittance in the infrared spectrum is shown by the glasses in the silicate systems and, among the silicate systems, by the lead silicates. It was also shown that for wavelengths from 4 to 5 μ, lead silicate glasses have a higher transmittance than fused silica glass. His report gave the transmittance curve of a lead silicate glass having the composition $4PbO.6SiO_2$ (71% of lead oxide, 29% of silica, by weight).

The experimental glasses prepared for our work contained 70.86 to 88.08 percent by weight of lead oxide. The transmittance curve for glass 6 shown, in figure 5, is similar to that published by Gerlovin. Glasses 7 and 8 contain more lead oxide than any glass reported by Gerlovin. It is evident that increasing the lead oxide content above 70.86 percent decreases the percentage of transmittance up to the 2.8-μ absorption band, but increases the transmittance for wavelengths from 3.25 to about 5.0 μ.

V. Summary

The transmittance of infrared energy by lithium, sodium, potassium, and lead silicate glasses has been measured for wavelengths of 0.7 to 5 μ. It was found that glasses containing lithia-silica gave a greater transmittance of infrared energy than the glasses of either soda-silica or potash-silica systems.

Increasing the percentage of lead oxide in a lead silicate glass does not increase the transmittance of infrared energy for all wavelengths.

A glass of the composition 71 percent of PbO, 29 percent of SiO_2, will give the maximum transmittance of infrared energy in the range of wavelengths from 0.8 to about 2.7 μ.

Increasing the quantity of lead oxide above 71 percent increases the transmittance of infrared energy in the range of wavelengths from 3.25 to about 5.0 μ, but lowers the transmittance in the range from 0.8 to 2.7 μ.

The authors thank Mrs. Helen Pool and J. J. Diamond for their cooperation in making the measurements of transmittances and the chemical analyses, respectively.

VI. References

[1] W. Eitel, M. Pirani, and K. Scheel, Glastechnische tabellen (29 Ultrarotdurchläss, Springer, Berlin 1932).
[2] J. I. Gerlovin, Acad. Sci. URSS **38,** 5 to 6, 170 (1943).
[3] R. Stair and C. A. Faick, J. Research NBS **38,** 9 (1947) RP1761.
[4] F. C. Kracek, J. Phys. Chem. **34,** 264 (1930).
[5] R. F. Geller, A. S. Creamer, and E. N. Bunting, J. Research NBS **13,** 237 (1934) RP705.
[6] A. J. Harrison, J. Am. Ceram. Soc. **30,** 362 (1947).
[7] R. Stair and W. W. Coblentz, BS J. Research **11,** 703 (1933) RP617.
[8] W. W. Coblentz, BS Bul. **10,** 1 (1913) S204.
[9] W. W. Coblentz, BS Bul. **13,** 423 (1916) S282.
[10] W. W. Coblentz, BS Sci. Pap. **17,** 187 (1921) S413.
[11] W. W. Coblentz, BS Sci. Pap. **17,** 187 (1921) S413.
[12] R. Stair and W. W. Coblentz, J. Research NBS **15,** 295 (1935) RP830.
[13] F. C. Kracek, J. Phys. Chem. **34,** 1583 (1930).

Washington, August 16, 1948.

INDEX TO VOLUME 41

A

Page

Accelerometers, calibration, RP1930 359
Acid-base equilibrium constant and dipole moment of tribenzylammonium picrate in benzene:
RP1896 1
RP1897 7
Acid-base reactions in organic solvents, RP1900 27
Airplane model, landing impact tests, RP1936 509
Aliphatic halide-carbonyl, condensations by means of sodium, RP1909 111
Alkylammonium picrates, dipole moment and association of benzene and dioxane, RP1896 1
Alloys, aluminum, marine-atmosphere stress-corrosion tests, RP1905 69
Alloys and commercial steels, effect of boron on hardenability, RP1938 545
Aluminates of barium, hydrated, preparation, optical properties, X-ray diffraction, RP1908 103
Aluminum alloys, corrosion resistance and tensile properties, RP1905 69
American Petroleum Institute-National Bureau of Standards hydrocarbons, freezing points, RP1929 323
Amides of glucuronic, galacturonic, and mannuronic acids, RP1943 609
Amino derivatives of mannuronic acid, RP1898 11
Arc-lamp exposure colorfastness and stability of materials under, RP1916 169
Autoclave test for soundness of hydrated lime, RP1917 179
Automotive engines, effect of substitute fuels, RP1913 135

B

Ballistic measurements, and instrument for the rapid production of a decimal series of potentials and its application to, RP1902 45
Barium aluminate hydrates, preparation, optical properties, X-ray diffraction, RP1908 103
Barium 2-ketolactobionate-barium bromide, preparation, RP1910 119
Barium-magnesium titanate dielectrics, properties, RP1899 17
Bases, organic, reaction with phenolsulfonephthalein derivatives in benzene, RP1900 27
Bending stresses in aircraft wings, RP1936 509
Benedict, William S., Richard C. Nelson, Earle K. Plyler, Absorption spectra of methane in the near infrared, RP1944 615
Benzene, acid-base reactions in, RP1900 27
Blaine, Raymond L., Harold J. Valis, Studies of the Mattson shot classifier, RP1931 371
Bloom, Evelyn G., Fred L. Mohler, J. H. Lengel, C. Edward Wise, Mass spectra of octanes, RP1912 129
Boron-treated alloys and steels, hardenability, RP1938 545
Bradford, William R., Harold O. Wyckoff, Robert J. Kennedy, Broad and narrow beam attenuation of 500 to 1,400 kilovolt X-rays in lead and concrete, RP1920 223
Bradt, Paul, Samuel L. Madorsky, Sidney Straus, Concentration of isotopes of mercury in countercurrent molecular stills, RP1918 205
Brickwedde, F. G., Harold W. Woolley, Russell B. Scott, Compilation of thermal properties of hydrogen in its various isotopic and ortho-para modifications, RP1932 379
Bruce, Clarence S., Jesse T. Duck, A. R. Pierce, Effects of substitute fuels on automotive engines, RP1913 135
Bueding, Elmer N., George R. Shelton, Ansel S. Creamer, Properties of barium-magnesium titanate dielectrics, RP1899 17
Bull, Marie T., Anton J. Streiff, Janice C. Zimmerman, Laurel F. Soule, Vincent A. Sedlak, Charles B. Willingham, Frederick D. Rossini, Purification, purity, and freezing points of 30 hydrocarbons of the API-Standard and API-NBS series, RP1929 323

C

Calcaterra, Edgar A., Abraham Fookson, Thomas W. Mears, Frank L. Howard, Aliphatic halide-carbonyl condensations by means of sodium, RP1909 111
Capacitance, direct, standards for low values of, RP1935 497
Carlson, Elmer T., Lansing S. Wells, Barium aluminate hydrates, RP1908 103
Carwile, Nesbit L., Thomas G. Digges, Carolyn R. Irish, Effect of boron on the hardenability of high-purity alloys and commercial steels, RP1938 545
Chemical durability, specular glass, and transmittance of optical glasses, RP1933 477
Clarke, Walter F., Lansing S. Wells, Ernest M. Levin, Expansive characteristics of hydrated limes and the development of an autoclave test for soundness, RP1917 179
Collagen and leather, expansivity, RP1924 279
Colorfastness and stability of materials under arc-lamp exposure, RP1916 169
Color perceptions of color-blind observers, RP1922 247
Concrete and lead barriers for X-ray protection, RP1920 223
Copolymers, mechanism of formation by addition of polymerization, RP1937 521
Copper isotopes, concentration of by countercurrent electromigration, RP1901 41
Copper tartrate reagent, method of preparation, RP1919 211
Corrosion-stress tests of aluminum alloy, RP1905 69
Creamer, Ansel S., George R. Shelton, Elmer N. Bunting, Properties of barium-magnesium titanate dielectrics, RP1899 17
Cryoscopic constants of hydrocarbons, RP1929 323
Crystal modification of manganese dioxide, RP1941 589
Cuprous oxide as a method of reducing sugar, RP1919 211
Current, destruction of superconductivity by, RP1940 581
Curtis, Harvey L., Howard S. Roberts, An instrument for the rapid production of a decimal series of potentials and its application to ballistic measurements, RP1902 45

D

Dahl, Andrew I., Paul D. Freeze, Laboratory evaluation of a method proposed by Gnam for measuring the temperature of rotating parts, RP1942 601
Davis, Marion Maclean, Priscilla J. Schuhmann, Mary Ellen Lovelace, Acid-base reactions in organic solvents. Behavior of some halogenated derivatives of phenolsulfonephthalein with different classes of organic bases in benzene, RP1900 27
Day, Frank H., Thimble-chamber calibration on soft X-rays, RP1926 295
Density of lactose solutions, RP1904 63
Deuteranopic observers, color perceptions, RP1922 247
Deuterium and hydrogen, pressure-volume-temperature relations, RP1932 379
Diamagnetic anisotropy of crystalline and oriented materials, RP1914 151
Die for cutting rubber test specimens, RP1907 95
Dielectric constant and power losses of barium-magnesium titanate dielectrics, RP1899 17
Dielectric constant of benzene and dioxane solutions, RP1896 1
Digges, Thomas G., Carolyn R. Irish, Nesbit L. Carwile, Effect of boron on the hardenability of high-purity alloys and commercial steels, RP1938 545
Dipole moments of alkylammonium and tribenzylammonium picrates:
RP1896 1
RP1897 7
Dry cells, manganese dioxide for, RP1941 589
Duck, Jesse T., Clarence S. Bruce, A. R. Pierce, Effects of substitute fuels on automotive engines, RP1913 135
Dynamic measurements of accelerations on aircraft, RP1930 359

E

Electrical resistance of superconducting wires, effect of temperature and current, RP1940 581
Electrode function of soda-silica glasses, RP1923 273

Page

Electrode, glass, inhibiting films on, RP1915 ... 163
Electromigration, concentration of ^{63}Cu by, RP1901 ... 41
Electron microscopy of wool fibers, RP1921 ... 231
Expansive characteristics of hydrated limes, RP1917 ... 179

F

Ferry, John D., Viscoelastic properties of polymer solutions, RP1903 ... 53
Florence, Jack M., Francis W. Glaze, Clarence H. Hahner, Ralph Stair, Transmittance of near infrared energy by binary glasses, RP1945 ... 623
Fookson, Abraham, Edgar A. Cadwallader, Thomas W. Mears, Frank L. Howard, Aliphatic halide-carbonyl condensations by means of sodium, RP1909 ... 111
Freeze, Paul D., Andrew I. Dahl, Laboratory evaluation of a method proposed by Gnam for measuring the temperatures of rotating parts, RP1942 ... 601
Frush, Harriet L., Horace S. Isbell, Amides of glucuronic, galacturonic, and mannuronic acids, RP1943 ... 609
—, —, Amino derivatives of mannuronic acid, RP1898 ... 11
Fuels, substitute, effect on automotive engines, RP1913 ... 135

G

Gage, thickness, for rubber test specimens, RP1907 ... 95
Galacturonic acid, amino derivatives, RP1943 ... 609
Girders, welded-steel box, bending test, RP1934 ... 483
Glass, chemical durability, RP1923 ... 273
Glass, electrode, inhibiting films on, RP1915 ... 163
Glasses, binary, transmittance of near infrared energy by, RP1945 ... 623
Glaze, Francis W., Jack M. Florence, Clarence H. Hahner, Ralph Stair, Transmittance of near infrared energy by binary glasses, RP1945 ... 623
Glucuronic acid, amino derivative, RP1943 ... 609
Gnam method for measuring temperatures of rotating parts, RP1942 ... 601
Golorato, Esther, Howard F. McMurdie, Study of the modifications of manganese dioxide, RP1941 ... 589
Grauer, Oscar H., Gerald F. Rynders, Donald Hubbard, Electrode function (pH response) of the soda-silica glasses, RP1923 ... 273

H

Hahner, Clarence H., Jack M. Florence, Francis W. Glaze, Ralph Stair, Transmittance of near infrared energy by binary glasses, RP1945 ... 623
Hammond, Lester D., Determination of lactose alone and in the presence of sucrose by the method of Munson and Walker, RP1919 ... 211
Hardenability of some alloys and steels, effect of boron on, RP1938 ... 545
Hessing, Harold, Hugh L. Logan, Stress-corrosion tests on high-strength aluminum alloy sheet, RP1905 ... 69
Hobbs, Edward V., Samuel Levy, Albert E. McPherson, Calibration of accelerometers, RP1930 ... 359
Holt, William L., Ellis O. Knor, Frank L. Roth, Strain tester for rubber, RP1907 ... 95
Howard, Frank L., Edgar A. Cadwallader, Abraham Fookson, Thomas W. Mears, Aliphatic halide-carbonyl condensations by means of sodium, RP1909 ... 111
Hubbard, Donald, Gerald F. Rynders, Oscar H. Grauer, Electrode function (pH response) of the soda-silica glasses, RP1923 ... 273
—, —, Chemical durability, specular gloss, and transmittance of optical glasses, RP1933 ... 477
—, —, Thickness of inhibiting films on glass electrode surfaces, RP1915 ... 163
Hydrated barium aluminates, preparation, optical properties, X-ray diffraction, RP1908 ... 103
Hydrocarbons, mass spectra, RP1912 ... 129
Hydrocarbons, purification, purity, and freezing points of API-Standard and API-NBS series, RP1929 ... 323
Hydrogen, thermal properties, RP1932 ... 379
Hygroscopicity of soda-silica glasses, RP1923 ... 273

I

Impact landing tests of model airplane, RP1936 ... 509
Infrared absorption spectra of methane, RP1944 ... 615
Infrared energy, near, transmittance of binary glasses, RP1945 ... 623
Infrared prism spectrometry, RP1911 ... 125
Interferograph photographing of interference fringes, RP1925 ... 287
Irish, Carolyn R., Thomas G. Digges, Nesbit L. Carwile, Effect of boron on the hardenability of high-purity alloys and commercial steels, RP1938 ... 545

Page

Isbell, Horace S., Harriet L. Frush, Amides of glucuronic, galacturonic, and mannuronic acids, RP1943 ... 609
—, —, Amino derivatives of mannuronic acid, RP1898 ... 11
—, *William W. Walton*, Barium 2-ketolactobionate and the corresponding barium bromide double salt, RP1910 ... 119
Isotopes, concentration of, by electromigration, RP1901 ... 41
Isotopes of mercury, concentration in countercurrent molecular still, RP1918 ... 305
Isotopic modifications of hydrogen, thermal properties, RP1932 ... 379

J

Jaffe, Bernard S., Ambrose H. Stang, Bending tests of large welded steel box girders at different temperatures, RP1934 ... 483
Judd, Deane B., Color perceptions of deuteranopic and protanopic observers, RP1922 ... 247

K

Kennedy, Robert J., Harold O. Wyckoff, William R. Bradford, Broad- and narrow-beam attenuation of 500- to 1,400-kilovolt X-rays in lead and concrete, RP1920 ... 221
2-Ketolactobionic acid, crystalline barium salts, RP1910 ... 119
Knor, Ellis O., William L. Holt, Frank L. Roth, Strain tester for rubber, RP1907 ... 95

L

Lactose, gravimetric determination, RP1919 ... 211
Lactose solutions, density and refractive indices, RP1904 ... 63
Landing impact tests of model airplane, RP1936 ... 509
Launer, Herbert F., Light-sensitive papers as controls for testing textile colorfastness and stability of materials under arc lamp exposure, RP1916 ... 169
Lead and concrete barriers for X-ray protection, RP1920 ... 221
Leather and collagen, expansivity, RP1924 ... 273
Lengel, J. H., Evelyn G. Bloom, Fred L. Mohler, C. Edward Wise, Mass spectra of octanes, RP1912 ... 129
Lenses, sources of error, RP1927 ... 301
Levin, Ernest M., Lansing S. Wells, Walter F. Clarke, Expansive characteristics of hydrated limes and the development of an autoclave test for soundness, RP1917 ... 179
Levy, Samuel, Albert E. McPherson, Edward V. Hobbs, Calibration of accelerometers, RP1930 ... 359
Limes, expansive characteristics of hydrated, RP1917 ... 179
Logan, Hugh L., Harold Hessing, Stress-corrosion tests on high-strength aluminum alloy sheet, RP1905 ... 69
Lovelace, Mary Ellen, Marion Maclean Davis, Priscilla J. Schuhmann, Acid-base reactions in organic solvents. Behavior of some halogenated derivatives of phenolsulfonephthalein with different classes of organic bases in benzene, RP1900 ... 27

M

Madorsky, Samuel L., Paul Bradt, Sidney Straus, Concentration of isotopes of mercury in countercurrent molecular stills, RP1918 ... 305
—, *Sidney Straus*, Concentration of copper 63 by countercurrent electromigration method, RP1901 ... 41
Magnesia, effect on expansion of plaster and cement-lime bars, RP1917 ... 179
Magnetochemistry, applications to polymers and polymerization, RP1914 ... 135
Manganese dioxide, study of modification, RP1941 ... 589
Mannuronic acid, amino derivatives:
RP1898 ... 11
RP1943 ... 609
Marine-atmosphere-exposure stress-corrosion tests of aluminum alloy sheets, RP1905 ... 69
Maryott, Arthur A., Acid-base equilibrium constant and dipole moment of tribenzylammonium picrate in benzene from measurements of dielectric constant, RP1897 ... 1
—, Dipole moments and molecular association of some picrates of primary, secondary, and tertiary amines in benzene and dioxane, RP1896 ... 1
Mass spectra of octanes, RP1912 ... 129
Mass spectrometer investigation of polymers, RP1928 ... 291
Matfson shot classifier, use in determination of size and size distribution of peening shot, RP1931 ... 371
McDonald, Emma J., Anne L. Turcotte, Density and refractive indices of lactose solutions, RP1904 ... 63

Page

McMurdie, Howard F., Esther Golovato, Study of the modifications of manganese dioxide, RP1941 589
McPherson, Albert E., Samuel Levy, Edward V. Hobbs, Calibration of accelerometers, RP1930 359
Walter Ramberg, Experimental verification of theory of landing impact, RP1936 509
Mears, Thomas W., Edgar A. Cadwallader, Abraham Fookson, Frank L. Howard, Aliphatic halide-carbonyl condensations by means of sodium, RP1909 111
Mercury, concentration of isotopes, RP1918 205
Methane, absorption spectra, RP1944 615
Mohler, Fred L., Evelyn G. Bloom, J. H. Lengel, C. Edward Wise, Mass spectra of octanes, RP1912 129
Molecular association and dipole moments of alkylammonium picrates, RP1896 1
Molecular stills for concentrating isotopes of mercury, RP1918 205
Monochromator, illumination of image shifts in, RP1925 287
Monomers, reactivity of free radicals derived from, RP1937 521
Moon, Charles, C. Matilda Sparks, Standards for low values of direct capacitance, RP1935 497
Munsell notations for color-blind observers, RP1922 247
Munson and Walker, reducing sugar method, RP1919 211

N

Nelson, Richard C., Earle K. Plyler, William S. Benedict, Absorption spectra of methane in the near infrared, RP1944 615

O

Octanes, mass spectra, RP1912 129
Optical glasses, chemical durability, specular glass, and transmittance, RP1933 477
Ortho-para modifications of hydrogen, thermal properties, RP1932 379
Oscillograph, voltage calibration of, RP1902 45

P

Papers, light-sensitive, as controls for testing colorfastness, RP1916 169
Peening shot, size and size distribution, RP1931 371
Phenolsulfonephthalein derivatives, reactions with organic bases in benzene, RP1900 27
Photographic lenses, errors in, and calibration of *f*-number, RP1927 301
Picrates, alkylammonium and tribenzylammonium, dipole moment: RP1896 1
RP1897 7
Pierce, A. R., Clarence S. Bruce, and Jesse T. Duck, Effects of substitute fuels on automotive engines, RP1913 135
Plaster, effect of magnesia on failures, RP1917 179
Plyler, Earle K., Infrared prism spectrometry from 24 to 40 microns, RP1911 125
Richard C. Nelson, William S. Benedict, Absorption spectra of methane in the near infrared, RP1944 615
Polymer solutions, viscoelastic properties, RP1903 53
Polymerization, kinetics of, RP1937 521
Polymers and polymerization, applications of magnetochemistry to, RP1914 151
Polymers, thermal decomposition, RP1928 315
Polystyrene, solution in xylene, properties, RP1903 53
Potentials, an instrument for the rapid production of decimal series of, RP1902 45
Pressure-volume-temperature relations for hydrogen and deuterium, RP1932 379
Prism, constant deviation, for producing monochromatic light, RP1925 287
Protanopic observers, color perceptions of, RP1922 247
Pyrex, chemical durability, RP1933 477

R

Radio wave absorption, RP1939 575
Ramberg, Walter, Albert E. McPherson, Experimental verification of theory of landing impact, RP1936 509
Red-green color blindness, RP1922 247
Refractive indices and density of lactose solutions, RP1904 63
Resistance, electrical, of superconducting wires, RP1940 581
Roberts, Howard S., Harvey L. Curtis, An instrument for the rapid production of a decimal series of potentials and its application to ballistic measurements, RP1902 45

Page

Rossini, Frederick D., Anton J. Streiff, Janice C. Zimmerman, Laurel F. Soule, Marie T. Butt, Vincent A. Sedlak, Charles B. Willingham, Purification, purity, and freezing points of 30 hydrocarbons of the API-Standard and API–NBS series, RP1929 323
Rotating parts, measuring temperature of, RP1942 601
Roth, Frank L., Robert D. Stiehler, Strain test for evaluation of rubber compounds, RP1906 87
—, *William L. Holt, Ellis O. Knox,* Strain tester for rubber, RP1907 95
Rubber compounds, strain test for evaluation, RP1906 87
Rubber strain tester, RP1907 95
Rynders, Gerald F., Donald Hubbard, Chemical durability, specular gloss, and transmittance of optical glasses, RP1933 477
—, —, Thickness of inhibiting films on glass electrode surfaces, RP1915 163
—, *Oscar H. Grauer, Donald Hubbard,* Electrode function (pH response) of the soda-silica glasses, RP1923 273

S

Sand particles and peening shot, size and size distribution, RP1931 371
Saunders, James B., Image shifts caused by rotating a constant deviation prism in divergent light, RP1925 287
Schuhmann, Priscilla J., Marion Maclean Davis, Mary Ellen Lovelace, Acid-base reactions in organic solvents. Behavior of some halogenated derivatives of phenolsulfonephthalein with different classes of organic bases in benzene, RP1900 27
Scott, Russell B., Harold W. Woolley, F. G. Brickwedde, Compilation of thermal properties of hydrogen in its various isotopic and ortho-para modifications, RP1932 379
—, Destruction of superconductivity by current, RP1940 581
Sedlak, Vincent A., Anton J. Streiff, Janice C. Zimmerman, Laurel F. Soule, Marie T. Butt, Charles B. Willingham, Frederick D. Rossini, Purification, purity, and freezing points of 30 hydrocarbons of the API-Standard and API–NBS series, RP1929 323
Seeman, Gloria S., Max Swerdlow, A method for the electron microscopy of wool, RP1921 231
Selwood, Pierce W., Applications of magnetochemistry to polymers and polymerization, RP1914 151
Shelton, George R., Ansel S. Creamer, Elmer N. Bunting, Properties of barium-magnesium titanate dielectrics, RP1899 17
Simha, Robert, Leo A. Wall, Copolymerization, RP1937 521
Soda-silica glasses, electrode function, RP1923 273
Sodium, aliphatic halide-carbonyl condensations, RP1909 111
Solvents, organic, acid-base reactions, RP1900 27
Soule, Laurel F., Anton J. Streiff, Janice C. Zimmerman, Marie T. Butt, Vincent A. Sedlak, Charles B. Willingham, Frederick D. Rossini, Purification, purity, and freezing points of 30 hydrocarbons of the API-Standard and API–NBS series, RP1929 323
Sparks, C. Matilda, Charles Moon, Standards for low values of direct capacitance, RP1935 497
Spectra, infrared absorption, of methane, RP1944 615
Spectra, mass, of octanes, RP1912 129
Spectrometry, infrared prism, RP1911 125
Spectrophotometric studies of acid-base reactions in benzene, RP1900 27
Specular gloss, chemical durability, and transmittance of optical glasses, RP1933 477
Stair, Ralph, Jack M. Florence, Francis W. Glaze, Clarence H. Hahner, Transmittance of near infrared energy by binary glasses, RP1945 623
Standards for low values of direct capacitance, RP1935 497
Stang, Ambrose H., Bernard S. Jaffe, Bending tests of large welded-steel box girders at different temperatures, RP1934 483
Steel box girders, welded, bending tests, RP1934 483
Steels and alloys, boron-treated, hardenability, RP1938 545
Stiehler, Robert D., Frank L. Roth, Strain test for evaluation of rubber compounds, RP1906 87
Strain test for evaluation of rubber compounds, RP1906 87
Strain tester for rubber, RP1907 95
Straus, Sidney, Samuel L. Madorsky, Concentration of copper 63 by the countercurrent electromigration method, RP1901 41
—, —, *Paul Bradt,* Concentration of isotopes of mercury in countercurrent molecular stills, RP1918 205
Streiff, Anton J., Janice C. Zimmerman, Laurel F. Soule, Marie T. Butt, Vincent A. Sedlak, Charles B. Willingham, Frederick D. Rossini, Purification, purity, and freezing points of 30 hydrocarbons of the API-Standard and API–NBS series, RP1929 323
Stress-corrosion tests on aluminum alloys, RP1905 69
Sucrose, effect on determination of reducing sugars, RP1919 211

Page

Superconductivity of wires, destruction by current, RP1940 581
Swerdlow, Max, Gloria S. Seeman, A method for the electron microscopy of wool, RP1921 231

T

Taylor, Eloise W., Absorption of radio waves reflected at vertical incidence as a function of the sun's zenith angle, RP1939 575
Temperature, low, effect on electrical resistance of superconducting wires, RP1940 581
Temperature of rotating parts, RP1942 601
Textiles, colorfastness under arc-lamp exposure, RP1916 169
Thallium bromide-iodide prism, RP1911 125
Thermal decomposition of polymers, RP1928 315
Thermal properties of titanate dielectrics, RP1899 17
Thermodynamic properties of hydrogen, RP1932 379
Thimble-chamber calibration on soft X-rays, RP1926 295
Titanate dielectrics, barium-magnesium, properties, RP1899 17
Transmittance, chemical durability, and specular gloss of optical glasses, RP1933 477
Transmittance of near infrared energy by binary glasses, RP1945 623
Tribenzylammonium picrate in benzene, dipole moment and dissociation, RP1897 7
Turcotte, Anne L., Emma J. McDonald, Density and refractive indices of lactose solutions, RP1904 63

U

Uronic acids, amino derivatives:
RP1898 11
RP1943 609

V

Valis, Harold J., Raymond Blaine, Studies of the Mattson shot classifier, RP1931 371
Vapor pressures of the hydrogens, RP1932 379
Vertical incidence absorption, RP1939 575
Viscoelasticity of polymer solutions, RP1903 53
Voltage divider, a rapid acting, RP1902 45
Vulcanizing characteristics of rubber, RP1906 87

W

Page

Wall, Leo A., Mass spectrometric investigation of the thermal decomposition of polymers, RP1928 315
—, *Robert Simha*, Copolymerization, RP1937 521
Walton, William W., Horace S. Isbell, Barium 2-ketolactobionate and the corresponding barium bromide double salt, RP1910 119
Washer, Francis E., Sources of error in and calibration of the *f*-number of photographic lenses, RP1927 301
Weir, Charles E., Effect of temperature on the volume of leather and collagen, RP1924 279
Welded-steel box girders, bending tests, RP1934 483
Wells, Lansing S., Elmer T. Carlson, Barium aluminate hydrates, RP1908 103
—, *Walter F. Clarke, Ernest M. Levin*, Expansive characteristics of hydrated limes and the development of an autoclave test for soundness, RP1917 179
Willingham, Charles B., Anton J. Streiff, Janice C. Zimmerman, Laurel F. Soule, Marie T. Butt, Vincent A. Sedlak, Frederick D. Rossini, Purification, purity, and freezing points of 30 hydrocarbons of the API-Standard and API-NBS series, RP1929 323
Wise, C. Edward, Evelyn G. Bloom, Fred L. Mohler, J. H. Lengel, Mass spectra of octanes, RP1912 129
Wool fibers, electron microscopy, RP1921 231
Woolley, Harold W., Russell B. Scott, F. G. Brickwedde, Compilation of thermal properties of hydrogen in its various isotopic and ortho-para modifications, RP1932 379
Wyckoff, Harold O., Robert J. Kennedy, William R. Bradford, Broad and narrow-beam attenuation of 500 to 1,400 kilovolt X-rays in lead and concrete, RP1920 223

X

X-ray diffraction study of manganese dioxide, RP1941 589
X-ray protection, lead and concrete barriers, RP1920 223
X-rays, soft, thimble-chamber calibration, RP1926 295

Z

Zimmerman, Janice C., Anton J. Streiff, Laurel F. Soule, Marie T. Butt, Vincent A. Sedlak, Charles B. Willingham, Frederick D. Rossini, Purification, purity, and freezing points of 30 hydrocarbons of the API-Standard and API-NBS series, RP1929 323

Engineering
Library

FEB

Journal of Research

of the

National Bureau of Standards

DECEMBER 1948

VOLUME 41 NUMBER 6

PERIODICALS OF THE NATIONAL BUREAU OF STANDARDS

Journal of Research

The National Bureau of Standards is the principal agency of the Federal Government for fundamental research in physics, chemistry, and engineering. It has the custody of the national standards of physical measurement in terms of which all working standards in research laboratories and industry are calibrated, and carries on necessary research leading to improvement in such standards and methods of measurement. It also has a general responsibility for basic research in physics, chemistry, and engineering, and for development of improved methods for testing materials and equipment. It determines physical constants and properties of materials, tests and calibrates standard measuring apparatus and reference standards, and studies technical processes. The results of the Bureau's research and investigations are published in the JOURNAL OF RESEARCH.

Research Papers

Reprints of individual articles appearing in the JOURNAL OF RESEARCH. They are made available to serve the needs of research workers, technical groups, and others for the separate papers relating to the special subjects in which they are interested.

Technical News Bulletin

Contains short but complete summaries of research, development, and testing in progress at the Bureau, accounts of the Bureau's national and international activities, scientific and technical announcements of new plans and programs, and a list of publications by members of the staff. It is a prompt and reliable source of official information of value to those who desire to keep in touch with the general activities of the Bureau.

Basic Radio Propagation Predictions

The CRPL-D series, Basic Radio Propagation Predictions, is issued as a monthly publication for those concerned with radio communication in determining the best sky-wave frequencies over any path at any time of day for average conditions for the month of prediction, which is made 3 months in advance. Charts of extraordinary-wave critical frequency for the F2 layer, of maximum usable frequency for a transmission distance of 4,000 km, and of percentage of time occurrence for transmission by sporadic E in excess of 15 Mc, for a distance of 2,000 km, are included.

ANNUAL SUBSCRIPTION Send order, with remittance, to Superintendent of Documents, U. S. Government Printing Office, Washington 25, D. C.	United States, Canada, Cuba, Mexico, Newfoundland, Republic of Panama	Other countries
JOURNAL OF RESEARCH of the National Bureau of Standards:		
12 monthly issues (2 volumes), paper covers	$4.50	$5.50
Bound volume (½ year, 1 volume), blue buckram	3.00	3.50
RESEARCH PAPERS	(*)	(*)
TECHNICAL NEWS BULLETIN, 12 monthly issues	1.00	1.35
BASIC RADIO PROPAGATION PREDICTIONS, 12 monthly issues	1.00	1.25

*The prices of the separate Research Papers appearing in this JOURNAL are given in the Contents. If 100 or more copies of any separate are ordered, a discount of 25 percent is allowed. Those who desire copies of separate Research Papers should send their orders and remittances without delay to the Superintendent of Documents, U. S. Government Printing Office, Washington 25, D. C. This will aid him to determine the number of copies to be printed for sale. Research Papers are not printed from electrotypes and usually no more reprints can be had when the first and only printing is exhausted.

Published with approval of Bureau of the Budget